Summer 2016

Fluvial Incision, Upper Plate Faulting, and Short-Term Deformation in the Southern Olympic Mountains of Washington State

Jaime Delano
Western Washington University, delanoj@wwu.edu

FLUVIAL INCISION, UPPER PLATE FAULTING, AND SHORT-TERM DEFORMATION IN THE SOUTHERN OLYMPIC MOUNTAINS OF WASHINGTON STATE

By

Jaime Delano

Accepted in Partial Completion
Of the Requirements for the Degree
Master of Science

Kathleen L. Kitto, Dean of the Graduate School

ADVISORY COMMITTEE:

Chair, Dr. Colin Amos

Dr. John Loveless

Dr. Doug Clark

MASTER'S THESIS

In presenting this thesis in partial fulfillment of the requirements for a master's degree at Western Washington University, I grant to Western Washington University the non-exclusive royalty-free right to archive, reproduce, distribute, and display the thesis in any and all forms, including electronic format, via any digital library mechanisms maintained by WWU.

I represent and warrant this is my original work, and does not infringe or violate any rights of others. I warrant that I have obtained written permissions from the owner of any third party copyrighted material included in these files.

I acknowledge that I retain ownership rights to the copyright of this work, including but not limited to the right to use all or part of this work in future works, such as articles or books. Library users are granted permission for individual, research and non-commercial reproduction of this work for educational purposes only. Any further digital posting of this document requires specific permission from the author.

Any copying or publication of this thesis for commercial purposes, or for financial gain, is not allowed without my written permission.

Jaime Delano
July 22, 2016

FLUVIAL INCISION, UPPER PLATE FAULTING, AND SHORT-TERM DEFORMATION IN THE SOUTHERN OLYMPIC MOUNTAINS OF WASHINGTON STATE

A Thesis
Presented to
The Faculty of
Western Washington University

In Partial Fulfillment
Of the Requirements for the Degree
Master of Science

by
Jaime Delano
July 2016

Abstract

Understanding topographic development in subduction zone forearcs requires comparison of deformation at short and long-term time intervals. We focus here on geomorphic records of uplift and incision in the Cascadia forearc of Washington State for comparison with short-term deformation driven by subduction zone coupling. We use surficial geologic mapping, optically stimulated luminescence dating, and surveyed terrace strath elevations to document fluvial incision and fault slip rates in the Wynoochee River valley in the southern Olympic Mountains. Results from 14 optically stimulated luminescence samples yield fluvial terrace age groupings of ~7-12 ka, ~14-18 ka, ~30-45 ka, and ~50-60 ka, which likely correspond to climate-modulated fluctuations in sediment supply within this repeatedly glaciated catchment. Calculated fluvial incision rates from surveyed terrace straths range between ~0.4 and 3.1 mm/yr, though incision in the upper reaches of the Wynoochee River is likely influenced by repeated valley aggradation, re-excavation, and isostatic rebound from glaciation, thereby hampering straightforward tectonic interpretation of calculation incision rates. Differential incision in the lower reaches of the river, however, is more straightforward to interpret and displays broad warping of the terrace tread and strath incision, potentially preserving a component of interseismic uplift. Terrace surfaces are vertically displaced by the active Canyon River fault, across which we estimate reverse dip-slip rates of ~0.1-0.3 mm/yr. We compare fault slip and incision results with a boundary element model constrained by GPS geodesy, estimating slip on the Canyon River fault and regional deformation in response to interseismic stress from the Cascadia subduction zone. The modeled reverse slip rates range between ~0.1-0.5 mm/yr, with lower rates of ~0.1-0.15 mm/yr near the Wynoochee River. Additionally, predicted uplift along the valley shows

similar broad warping to the incision record in the lower reaches. The general agreement between observed long-term geologic record and modeled short-term deformation suggests that a portion of Cascadia interseismic strain may be permanent, manifested as fluvial incision and slip along upper-plate faults. Consistency between these signatures over time may indicate relative stability in the spatial pattern of subduction zone coupling over ~10^4 yr intervals.

Acknowledgements

This research was supported by funding from the EarthScope AGeS award*, the Geological Society of America (GSA), and Western Washington University. Base maps used in Figure 1 and Plate 1 were derived from Washington 10 m DEM (http://gis.ess.washington.edu/data/raster/tenmeter/byquad/). Lidar DEMs used in Figs. 2, 5, and Plate 1 and topographic analyses were accessed from Puget Sound Lidar Consortium (PSLC).

I thank my advisor Colin Amos and committee members Jack Loveless and Doug Clark for their patience, constructive feedback, and advice. Thanks to Tabor Reedy, Kaelin Newman, Scott Bennett and Brian Sherrod for their assistance and discussion in the field, as well as Tammy Rittenour, Carlie Ideker, Kirk Townsend, and Michelle Summa-Nelson for their OSL lab assistance at Utah State University. Green Diamond Resource Co. was generous in allowing access to forest land. Thanks also to Randy Sutherby for allowing access to his property and for the insight to the cinematic history of the Wynoochee River.

*This material is based upon work supported by the National Science Foundation under Grant Nos. EAR-1358514, 1358554, 1358401, 1358443, and 1101100 (EarthScope National Office). Any opinions, findings, and conclusions or recommendations expressed in this material are those of the author(s) and do not necessarily reflect the views of the National Science Foundation.

Table of Contents

Abstract iv

Acknowledgements vi

List of Tables viii

List of Figures viii

Supplementary Figures viii

1. Introduction 1

2. Background 3

3. Methods 9

4. Results 14

5. Discussion 21

6. Conclusions 30

Appendix A: Unit descriptions 32

Appendix B: Alternative boundary element model iterations 34

References 36

Tables 41

Figures 44

Supplementary figures 59

List of tables

Table 1. Terrace strath survey data 41

Table 2. OSL sample data and results 42

Table 3. Scarp profile result data 43

Table 4. Strath incision data 44

List of figures

Figure 1. Regional Map of the Olympic Peninsula 45

Figure 2. Geomorphic map of the Wynoochee River valley 46

Figure 3. Valley profiles of Wynoochee River terrace treads 47

Figure 4. Valley channel width and rock type 48

Figure 5. Strath survey and incision valley profiles 49

Figure 6. Canyon River fault scarp profiles 50

Figure 7. Vertical separation and separation rates of fault profiles 51

Figure 8. Cascadia subduction zone dip-slip deficit 52

Figure 9. Boundary element model results for the Canyon River fault 53

Figure 10. Estimated regional uplift predicted from the boundary element model 54

Figure 11. Simulated slip on the Cascadia subduction zone 55

Figure 12. Simulated fault slip from a Cascadia subduction earthquake 56

Figure 13. Timing of terrace aggradation and regional alpine glacial advances 57

Figure 14: Time sequence schematic of the Wynoochee River incision history 58

Supplementary figures

Figures S1-S20. Stratigraphic columns of optically stimulated luminescence sites 59

Plate 1. Large format geomorphic map of the Wynoochee River valley ..... back cover

1. Introduction

A comprehensive picture of active deformation, topographic development, and seismic hazard in subduction zone forearcs requires understanding the relationships between short and long-term strain. Although interseismic deformation above a subduction zone is often considered to be largely elastic (Bilham et al., 1997; Mazzotti et al., 2002; Mitchell et al., 1994; Wells et al., 1998), the presence of topography implies a component of interseismic strain is permanently recorded in the geologic record (Kelsey et al., 1994; Meade, 2010). Vertical deformation in the upper plate of subduction zones represents complex and poorly understood contributions from megathrust earthquake cycle deformation (Savage, 1983), slip along upper-plate faults (e.g., Wells et al., 1998), and other processes such as underplating and/or aseismic folding (Hyndman and Wang, 1993; Pazzaglia and Brandon, 2001). Characterizing patterns of permanent deformation therefore requires measurements of incremental strain over multiple time intervals, including displacement and uplift rates recorded by Quaternary landforms, for comparison with constraints from the short-term geodetic record of earthquake cycle processes.

Longer-term strain measurements in the Cascadia subduction zone forearc have relied primarily on thermochonologic measurements of rock uplift at ~10^6 yr time scales (Brandon et al., 1998), and intermediate-term strain (10^3-10^5 yr) inferred from river incision (Pazzaglia and Brandon, 2001; Personius, 1995). Previous studies of fluvial incision rates in the Cascadia forearc reveal both spatial variability (Personius, 1995) and short-term temporal variability (Wegmann and Pazzaglia, 2002), although agreement between incision in the Olympic Mountains and spatial patterns of exhumation rates (Brandon et al., 1998; Pazzaglia and Brandon, 2001) suggests that the Olympic Mountains are in steady-state. Importantly, this match implies incision may be used as a proxy for vertical tectonic deformation. Incision rate studies on

the Olympic Peninsula are limited to one drainage (the Clearwater River, Fig. 1), however, and a potential link between intermediate-term incision and short-term vertical deformation associated with the Cascadia subduction zone earthquake cycle remains largely untested.

Deformation in the Cascadia forearc also includes north-south shortening implied by obliquity in plate convergence, manifested along upper plate faults revealed by lidar (Barnett et al., 2015; Blakely et al., 2009; Nelson et al., 2003; Walsh and Logan, 2007; Witter et al., 2008). The relationship of these faults to the subduction zone earthquake cycle, however, remains poorly understood. Previous studies in Cascadia usually assume that interseismic strain is entirely elastic, so upper plate faults accommodate north-south shortening from the deficit between the oblique long-term plate motion and a more trench-normal earthquake rebound (Mazzotti et al., 2002; McCaffrey et al., 2013; Wang et al., 1995). Alternatively, curvature in the subducting slab (Bevis et al., 2001) and/or oroclinal bending (Allmendinger et al., 2005) could focus trench-parallel shortening on upper plate faults. Upper plate faults are also sensitive to stress changes induced by great subduction earthquakes (Aron et al., 2013; Loveless and Pritchard, 2008). Accordingly, some studies suggest megathrust earthquakes may trigger slip on upper plate faults (Sherrod and Gomberg, 2014), or that upper plate events may initiate great subduction earthquakes by decoupling the subduction zone (González et al., 2015). Despite the extensive lidar coverage in many of the major drainages, upper plate fault deformation in the interior of the Olympic Mountains remains relatively sparsely studied.

Here, we use geomorphic mapping based on aerial lidar, optically stimulated luminescence dating (OSL), and surveyed terrace strath elevations to calculate intermediate-term deformation such as fault slip and fluvial incision in the Wynoochee River valley of southern Olympic Mountains of Washington State (Fig. 1). The drainage is orientated approximately

parallel to the strike of the subduction interface, allowing examination of trench-parallel deformation trends to contrast with trench-normal vertical deformation patterns revealed from previous studies (Pazzaglia and Brandon, 2001; Wegmann and Pazzaglia, 2002). We compare these intermediate-term measurements with an analysis of short-term deformation related to interseismic stress from the locked Cascadia subduction zone using a boundary element method (BEM) model with input conditions constrained by global positioning systems (GPS) observations. The model allows for estimation of slip rates of upper plate faults required to relieve stress imposed by interseismic coupling on the subduction zone interface, as well as more regional patterns of uplift. This analysis enables comparison of deformation constrained by short-term, geodetic data over the recent decades with those acting over longer geologic time scales. Together, these results provide the first examination of a potential relationship between Cascadia subduction zone interseismic deformation and activity on upper-plate faults, which in turn are capable of shaping the geomorphology of forearc rivers.

2. Background

2.1. Location, geology, and tectonic setting

The Cascadia subduction zone accommodates northeast-southwest convergence between the Juan de Fuca and North American plates (Fig. 1 inset). The majority of plate motion occurs during large megathrust earthquakes, the most recent of which occurred in A.D. 1700 (Atwater and Hemphill-Haley, 1997). Oblique plate convergence results in a component of long-term north-south shortening of the North American plate, distributed across western Washington at a relative shortening rate of ~5 mm/yr (Mazzotti et al., 2002). The degree to which geodetic velocities reflect long-term deformation, and therefore topographic development, remains

debated. Some studies suggest that interseismic strain is dominantly elastic, and therefore is released during megathrust earthquakes (Mitchell et al., 1994). Most existing mechanisms for forearc topographic development cite sources unrelated to the subduction zone earthquake cycle, such as accretion and aseismic folding (Pazzaglia and Brandon, 2001), or arc-parallel shortening unrelated to subduction earthquake slip (Mazzotti et al., 2002; Wells et al., 1998).

The Olympic Mountains represent the structural high of the subaerial forearc of the subduction zone accretionary wedge (Clowes et al., 1987). The subducting Juan de Fuca plate has a gentler dip below the Olympic Mountains than elsewhere in Cascadia, driving faster development of sub-aerial topography and greater relief than elsewhere in the forearc (Davis and Hyndman, 1989). The generalized geology of the Olympic Mountains consists of an accreted sedimentary core, the Olympic Subduction Complex, overthrust by pre-subduction Eocene Crescent Formation, comprised primarily of basalt and marine sedimentary rock (Fig. 1) (Tabor and Cady, 1978). The Crescent Formation wraps around the southern, eastern, and northern flanks of the Olympic Mountain Massif at lower elevations (Tabor and Cady, 1978), and represents the non-rigid backstop of the accretionary wedge (Brandon et al., 1998).

Along the southern half of the Cascadia margin in Oregon, spatially continuous marine terraces reveal generally low (near zero) uplift rates punctuated by regions of higher uplift (~1 mm/yr) (Kelsey et al., 1994) that mirror variations in fluvial incision within the Oregon forearc (Personius, 1995). These indicators of long term-differential strain along the plate boundary generally correspond to upper plate structures oriented at a high angle to the subduction zone margin (e.g. Kelsey et al., 1994; Merritts and Bull, 1989; West and McCrumb, 1988), but could indicate long-term variations in permanent interseismic strain along the subduction zone. The Olympic Peninsula lacks continuous marine terraces, but similarly to the Oregon coast, displays

generally low background uplift with shorter wave-length variation revealed by coastal stratigraphy (Kelsey et al., 1994; Pazzaglia and Brandon, 2001; Thackray, 1998). For example, the Kalaloch syncline, a broad (>32 km wavelength) syncline in Quaternary deposits accommodating north-south compression, displays differential uplift rates reaching 0.7 mm/yr (Thackray, 1998). While long-term uplift rates along the Olympic Peninsula coast are relatively well-documented (e.g., Kelsey et al., 1994; Thackray, 1998), our understanding of Olympic Mountain interior uplift remains limited by the dense forest cover that obscures landforms and limits accessibility.

Studies of incision in the Olympic Mountains are limited to the Clearwater River, an approximately convergence-parallel drainage in the western Olympic Mountains (Fig. 1). The lower Clearwater River valley remained mostly unglaciated during much of the Pleistocene and all of the Holocene, preserving a long record of incised terraces spanning the last ~140 ka (Pazzaglia and Brandon, 2001). Dating and analysis of these terraces demonstrate faster incision and uplift near the center of the range (~0.9 mm/yr) compared to relatively slow uplift near the coast (~0.1 mm/yr) (Pazzaglia and Brandon, 2001). Clearwater River terrace records from the Holocene show a similar headwater increase in incision, but with rates 2-3 times higher, which could reflect variability on time scales shorter than a full glacial-interglacial cycle (Wegmann and Pazzaglia, 2002). These incision records are consistent with longer-term erosion rates from apatite fission-tracks, which show radially decreasing exhumation rates centered just west of the highest peaks in the range, along a roughly convergence-parallel transect (Brandon et al., 1998).

The inference of steady state topography within the Olympic Mountains, however, remains untested in other parts of the range and lacks examination of potential trench-parallel uplift variability. Fluvial incision rates along the Oregon Coast Range indicates four-fold

variability (0.02 mm/yr – 0.08 mm/yr) in long-term subduction uplift (Personius, 1995). Balco et al. (2013) suggest that fluvial erosion variability in the Oregon Coast Range reflects north-propagating crustal thickening associated with the Mendocino Triple Junction migration. Fluvial incision, however, can contain poorly constrained contributions from isostatic rebound driven by rapid erosion or ice removal (Litchfield and Berryman, 2006; Thorson, 1989), channel substrate variability (e.g., Schanz and Montgomery, 2016), or changes in base level (Bull, 1991), rather than stemming from tectonic uplift alone. Increased high-resolution lidar coverage over the last decade in the Olympic Mountains allows for expansion of geomorphic analysis to many of the other major drainages in this portion of the Cascadia forearc.

2.2. The Wynoochee River basin

The Wynoochee River flows south from the southern Olympic Mountain interior to the mouth of the Chehalis River near sea level (Figs. 1 and 2a), with a total drainage area of ~560 km^2. The drainage is located ~30 km inland from the Olympic coast and is underlain primarily by basalt (Crescent Formation) and marine sedimentary bedrock (Montesano Formation) (Tabor and Cady, 1978). In contrast to previous fluvial studies in the Clearwater River basin, which is oriented roughly parallel to the Cascadia convergence direction, the Wynoochee River flows approximately parallel to the Cascadia margin, or perpendicular to convergence.

Previous Quaternary surficial mapping reveals at least three episodes of glaciation in the Wynoochee River valley (Carson, 1970). The youngest suite of deposits, the Grisdale drift, was interpreted to coincide temporally with the last glacial maximum (LGM) or Fraser glaciation, based primarily on weathering characteristics, glacial extent, and comparisons with adjacent drainages (Carson, 1970). The most expansive terraces in the Wynoochee Valley were

interpreted by Carson (1970) as outwash terraces from the retreating Grisdale glacier, with a lower suite of terraces corresponding to the Fraser maximum, more recently dated to ~17 ka (Porter and Swanson, 1998). Older outwash surfaces (Mobray and Helm Creek deposits) were estimated to coincide with Salmon Springs and Stuck glaciations in the Puget Lowlands based primarily on weathering characteristics, as well as glacial extent, correlations with other drainages, and radiocarbon-dead wood samples (Carson, 1970).

Extensive and repeated alpine glaciation complicates interpretation of the fluvial incision record in major western Olympic Mountain drainages such as the Hoh, Queets, and Quinault rivers (Pazzaglia and Brandon, 2001). Large glacial advances can obscure or remove older terraces and deposits, thereby removing the geomorphic record of fluvial incision. Isostatic rebound from ice removal can temporarily accelerate incision, while till and thick outwash terraces obscure the location of the bedrock channel floor. In the Wynoochee River, less extensive glaciation than in west-flowing drainages (Fig. 1) yields multiple terraces with limited thick outwash fill. Modern headwater precipitation and elevations are similar between the Wynoochee River and other major rivers, but the Wynoochee River annual discharge is significantly less, a result of a steeper precipitation gradient on the southern flanks of the Olympic Mountains (U.S. Geological Survey, 2016). Therefore, if contemporary patterns of precipitation are representative of paleoprecipitation, ice extent differences may stem from basin-averaged variability in precipitation and ice accumulation area.

Fluvial deposits and landforms in the Wynoochee River valley lack chronologic constraints based on traditional dating methods, such as radiocarbon dating, because of the abundance of reworked carbon and prevalence of deposits older than the radiocarbon age limits (Carson, 1970; Rittenour, 2008). New applications of OSL dating, however, have successfully

constrained late Quaternary fluvial terrace deposition elsewhere in the Olympic Mountains (Wyshnytzky et al., 2014). These samples reveal terrace ages spanning the LGM and ranging between ~15-24 ka, and correspond with the Twin Creeks 1 advance or the Fraser glaciation in the Puget Lowlands (Wyshnytzky et al., 2014).

2.3 Canyon River fault

High-resolution lidar reveals an uncharacterized extension of the northeast-striking Canyon River fault (CRF) cutting terraces along the Wynoochee River (Figs 1 and 2) (Walsh and Logan, 2007). The CRF is one of several similarly striking faults surrounding the Olympic Mountain massif that accommodate reverse motion (Fig. 1) (Barnett et al., 2015; Blakely et al., 2009; Brocher et al., 2001; Bucknam et al., 1999; Sherrod et al., 2008, 2004). The Saddle Mountain fault zone, Frigid Creek fault, and CRF are suggested to form an en echelon deformation zone and together accommodate north-south shortening inboard of the Olympic Mountain massif (Blakely et al., 2009). While the dominant signal from these faults is reverse, the direction and magnitude of lateral slip is poorly constrained. Slickenlines from paleoseismic trenches indicate dextral-reverse and sinistral-reverse motion within the Saddle Mountain fault zone (Barnett et al., 2015; Witter et al., 2008) with inconclusive preservation of lateral slip on the larger-scale geomorphic record.

A previous paleoseismic trench of the CRF ~10 km east of the Wynoochee River basin (Fig. 1) revealed a fault dipping ~70° to the southeast and reverse slip, with slickenlines raking both 25° and 65° indicating a variable component of sinistral slip (Walsh and Logan, 2007). The CRF trench showed evidence for an earthquake at ~1880 yr. B.P., with an estimated size of M_w ~6.7-7.8 (Walsh and Logan, 2007). Elsewhere in the southeastern Olympic Mountains,

paleoseismic work in the Saddle Mountain fault zone (Fig. 1) reveals post-glacial reverse slip rates of 0.2 mm/yr, and recent (3000 B.P.- present) slip rates between 0.7-3.2 mm/yr, with evidence of earthquakes as large as M_w 6.5–7.0 (Barnett et al., 2015). These past earthquakes reveal the need for quantifying seismic hazard in the Southern Olympic Mountains, specifically on the CRF, that poses an unknown risk to nearby Wynoochee Dam and nearby communities.

3. Methods

3.1 Geomorphic mapping, lidar analysis, and strath surveys

We use geomorphic mapping, lidar analysis, and differential GPS surveying of strath terrace elevations in the Wynoochee River valley to quantify fault slip and fluvial incision. Our geomorphic mapping builds on glacial landform mapping by Carson (1970) that predates lidar and the construction of the Wynoochee Dam. Using bare-earth lidar data accessed through Puget Sound Lidar Consortium (Quinault River Basin, 2012; Southwest Washington, 2009), we mapped terraces, moraines, landslides, and fault surface traces from the Wynoochee Dam to the confluence with the Chehalis River (Fig. 2a). Terrace age groupings are based on relative height ordering, height above the modern channel, surface morphology, and OSL ages. Faults were delineated within the lidar using visible scarps that displace other continuous landforms, such as terraces. Glacial deposits and landforms (e.g., till and moraines) were mapped based on surface morphology, such as kettle and kame topography, flutes, or irregular hummocky surfaces adjacent to flat deposits.

We calculate relative slip across faults as well as terrace incision by creating topographic profiles extracted from the lidar data. Fault scarp profiles are measured orthogonally across the fault trace. Vertical separation, dip-slip displacements, and associated uncertainties are

calculated using the Monte Carlo method following Thompson et al., (2002), varying fault dip from 55°-85° and fault location between ½ and ⅓ the scarp height. The fault dip range reflects the estimated 70° dip from Walsh and Logan, (2007), with equal probability of dip varying ± 15°.

For longitudinal terrace profiles along the entire river, we use valley distance, measured following the central axis of the Wynoochee River valley as in Pazzaglia and Brandon, (2001) (valley profile line in shown in Plate 1). Valley distance, compared to river distance, removes short-length variation caused by river meanders and allows direct elevation comparison of terraces projected from both sides of the valley. To create valley-length terrace tread profiles, individual terrace profiles were mapped and assigned elevations derived from the lidar. Tread profile lines were converted to elevation points spaced 10 m apart and projected orthogonally to the valley profile line.

We calculate river incision into bedrock and terrace fill thickness using the terrace tread profiles and field strath elevation surveys. We survey strath elevations and fill thicknesses using Trimble Geo7x GPS unit with a laser rangefinder. Survey locations are limited by exposure into terrace risers, and therefore only occur in select locations along the river such as accessible cut banks and road cuts. In the lower reaches of the river, we supplement strath surveys with bedrock depth information from well log data (Washington State Department of Ecology, 2016). We create a strath elevation profile for the most continuous terrace in the Wynoochee River using primarily direct strath survey measurements. To approximate the strath location between surveys, we use constraining maximum and minimum elevations from older and younger terrace strath surveys, as well as other field observations (e.g., gravel pit depth). Strath elevation error bars represent instrument uncertainty or the elevations of constraining observations. Incision is

calculated by subtracting the elevation of the modern river channel from the estimated strath profile at the same valley distance, as done in studies of the Clearwater River terraces (Pazzaglia and Brandon, 2001; Wegmann and Pazzaglia, 2002). Other studies have suggested potential complications with calculating incision using the elevation of the modern river channel as a reference datum (Finnegan et al., 2014; Gallen et al., 2015), but we focus here primarily on overall spatial patterns of incision rather than absolute incision rates.

We also evaluate changes in channel geometry as a means to assess fluvial response to active deformation and differential uplift. In this project, river width is calculated using the ChanGEOM MATLAB script (Fisher et al., 2012), using 3 m cells along the length of the river. The channel width data are smoothed to reduce noise using a 500-point moving average that represents 1500 m of river distance and is the approximate river length of one meander.

3.2. OSL sample collection and analysis

We use small aliquot, regenerative OSL dating of quartz sand to date terrace cover deposits along the length of the Wynoochee River. Natural radiation within these sediments causes electrons to become trapped in the crystal lattice of quartz grains, accumulating when shielded from heat and light (Rhodes, 2011). Electrons are released and when grains are exposed to light or heat, resetting OSL ages (Huntley et al., 1985). Therefore, the OSL ages represent the time since the strath cover sediments were deposited, and later incised, as a result of continued uplift. OSL can date glaciofluvial sediments spanning at least the past ~100 ky (Rittenour, 2008; Wyshnytzky et al., 2014) with uncertainties as low as 5% (Murray and Olley, 2002).

In this study, we collected sediment samples from exposures of outwash and strath terrace deposits. Samples were collected in terraces cut by mapped fault scarps, to constrain

earthquake timing and slip rates, as well as from the most continuous terraces, to calculate incision rates. Sample sites were chosen in exposures that showed clear fluvial lateral accretion structures (cross-bedding), targeting sediment containing the highest proportion of fine sand, and clearing the outer 10 cm of sediment. 19 of the 20 samples were collected by pounding an eight-inch opaque steel tube with a 1.5-inch diameter horizontally into the target material. One sample was collected at night, using red headlamps to avoid bleaching, by removing the outer ~5 cm of sediment and excavating one gallon of material into an opaque can. Approximately one quart of sediment from a 30 cm radius of the sample was collected at each site for dose rate analysis, along with a small film canister of sediment for water content measurements.

All sample preparation and analyses were performed at Utah State University under amber light (590 nm wavelength). Each sample was wet sieved to target fine sand and treated with hydrochloric acid (10% HCl) and bleach (10% H_2O_2) to remove carbonate and organic material. Quartz grains were separated from denser material using sodium polytungstate (2.7 g/cm^3). Quartz grains were then treated with concentrated hydrofluoric acid (47% HF) to remove feldspar and etch the outer grain. Moisture content was measured by calculating the weight difference between damp field sediment and the dried sample. To determine the background radiation dose rate, dry sediment was first split to obtain a representative sample. Measurements of K, Rb, U, and Th were performed at ALS Chemex in Reno, NV, using ICP-MS and ICP-AES. We use a minimum age model to estimate the ages, which favors younger, more fully bleached (reset) samples.

3.3. Boundary element modeling of interseismic strain

The CRF may partially control incision and uplift in the Wynoochee River valley, but the driving forces behind CRF slip are poorly understood. We evaluate the influence of the Cascadia subduction zone on upper plate structures by comparing the geologic history of uplift and incision along the Wynoochee River to modeled short-term deformation. We use the boundary element method (BEM) (Crouch and Starfield, 1983; Thomas, 1993) to model the stress imposed by regional tectonic processes, namely interseismic coupling on the subduction zone, onto other complex structures, such as upper plate faults, and in turn estimate average slip rates on these structures required to relieve the imposed stress. Thus the estimated slip rate distribution can be considered as a slip distribution of an earthquake on the CRF normalized by recurrence interval, under the assumption that the earthquake completely relieves accumulated shear stress imposed by subduction zone coupling. The estimated fault slip rates and predicted uplift patterns from the BEM model are compared to the observed geologic record, including paleoseismic slip rates and bedrock incision.

We first use an elastic block model (Meade and Loveless, 2009) to estimate microplate rotation and spatially variable slip deficit rates on the Cascadia subduction zone interface, the geometry of which is based on slab depth contours derived from seismicity data (McCrory et al., 2006) and represented with a continuous mesh of triangular dislocation elements (TDEs). The distribution of interseismic coupling is broadly similar to previous studies (e.g., McCaffrey et al., 2013). We then use the distribution of interseismic slip deficit rates on the Cascadia subduction zone to analytically calculate (Meade, 2007) the stress rate imposed on the CRF. We also represent the CRF using TDEs, projecting the mapped trace to 10 km depth, the approximate depth of the seismogenic crust, and rotating the plane to a ~70° dip to the southeast, as observed

in paleoseismic trenching (Walsh and Logan, 2007). We assume a shear traction-free boundary condition on CRF TDEs and prohibit element-normal motion. We then use the BEM to estimate the distribution of slip on the CRF required to relieve the stress imposed by Cascadia subduction zone coupling, similar to the approach of Marshall et al., (2009). Finally, we predict a vertical displacement field in the Wynoochee River valley region that reflects contributions from both Cascadia subduction zone coupling and CRF slip. We use the BEM model to test the hypothesis that the stress generated by contemporary subduction zone coupling is consistent with the longer-term fault kinematics of the CRF determined from paleoseismic observations.

4. Results

4.1 Geomorphic mapping

Our geomorphic mapping expands upon previous surficial mapping of predominately glacial deposits by Carson (1970). Geomorphic mapping reveals 19 flights of fluvial terraces, sorted into eight primary groups (Figs. 2 and 3, detailed descriptions in Appendix A). Terraces decrease in age and height above the river from Qt1 to Qt8, with inset terraces sharing the same strath denoted by lowercase letters (e.g., Qt8b and Qt8c). The older terraces (Qt1-Qt5) are primarily fill terraces, though the Qt5 deposit thins downstream transitioning from fill to strath. The younger terraces (Qt6-Qt8) are strath terraces with <3 m fill thickness. In addition to terraces, we map two generations of glacial deposits: Mobray Till (Qmt) and Grisdale Till (Qgt), modified from Carson (1970). Our mapped terraces Qt1 and Qt1b correspond with Carson's (1970) Helm Creek Drift, and terraces Qt2 and Qt2b correspond to Carson's (1970) Mobray Drift. Carson's High Fraser terraces correspond to our Qt3, Low Fraser terraces are primarily

mapped here as Qt4-Qt6c, and Holocene Alluvium (previously interpreted as present in postglacial terraces and floodplains) is mapped here as Qt7-Qt8c (Fig. 2).

Terrace tread long profiles reveal a complex sequence of terrace morphology (Fig. 3). Generally, more terrace treads are preserved upstream of the CRF and continue downstream of the lower gorge, with a gap in terrace preservation inside the lower gorge. This preservation pattern largely coincides with changes in channel substrate (Fig. 4). Segments of the valley with the largest number of terraces preserved are underlain by lacustrine deposits or Montesano Formation (relatively friable marine sedimentary rock). Fewer terraces are preserved in basalt bedrock within the lower gorge. Additionally, fewer low elevation terraces (<20 m above the channel) are preserved between valley distances 29 km – 36 km. The oldest terraces (Qt1-Qt2b) exist only in the lower reaches of the river, relatively high above the modern channel (>20 m). The surface of Qt3 and Qt4 apparently converge with Qt5 at ~22 km valley distance. The youngest terraces (Qt6-Qt8c) converge downstream with the modern river at ~30 km valley distance.

Terrace preservation patterns and channel bedrock changes also coincide with changes in channel width (Fig. 4). Overall, channel width in the Wynoochee River displays high frequency variation, but smoothing reveals more representative changes. The Wynoochee River narrows dramatically where the channel crosses the CRF and enters the inner lower gorge (Figs. 3b and 7). The changes in channel width are approximately coincident with changes in channel bedrock type, with the narrowest channel width values occurring in basalt. The channel narrowing and apparent knickpoint at ~2 km valley distance (referred to here informally as the upper gorge) coincides with a small fish dam (Fig. 4). Since the channel has been altered anthropogenically, the potential geologic significance of the upper gorge knickpoint and channel narrowing is not

considered here. Additionally, the extent of channel bottom substrate modification near the fish dam is unknown. The current channel bottom rock type is basalt, but Carson (1970) mapped lacustrine deposits along the Wynoochee River bottom extending from the entrance of the lower gorge upstream beyond the current Wynoochee Dam prior to dam construction. Therefore, some of the previously mapped lacustrine deposits from the Wynoochee Dam to south of the fish dam may have been removed during either dam construction.

Terrace Qt5 is the most continuous and accessible terrace in the valley. In total, we surveyed 29 strath elevations, integrated fill thickness field observations, and used bedrock depth from two well logs to constrain the Qt5 terrace strath location (Fig. 5, survey data in Table 1). Between valley distance ~3-7 km, Qt5 is overlain by a thick gravel fill, based on numerous gravel pits and road cuts that reach at least ~12 m below the tread surface, while Qt6, Qt7 and Qt8 generally have <3 m of fill. Downstream, within the lower gorge (valley distance ~7-12 km), virtually all terraces lack fill deposits above the strath. We discovered only one terrace exposure with fluvial sediment capping the bedrock (location of samples WYN-11 and WYN-12). South of the lower gorge (valley distance ~12-25 km), the Qt5 fill thickens, as evidenced by gravel pits at least 8 m deep below the surface of the tread, while terraces Qt6-Qt8c continue to have limited (<3 m) fill. Qt5 terraces in the lower reaches of the river (valley distance ~25-52 km) display variable fill thickness, but fill generally remains <5 m thick and increases slightly downstream. Virtually all exposures of Qt3, Qt2, and Qt1 are entirely fill material and lack a visible bedrock strath above river level. We observed one strath in Qt2, with fill cover thickness ~12 m.

Incision or strath height, calculated by subtracting the channel elevation from the strath elevation, is spatially variable along the length of the Wynoochee River (Fig. 5b). The Qt5 strath height varies along the length of the valley from ~5 m to ~45 m above the channel, with abrupt

changes roughly coinciding with channel bedrock changes. The highest Qt5 straths occur in basalt, and the lowest straths occur in lacustrine deposits or Montesano Formation. Increases in strath height also correspond to decreases in strath cover thickness. The largest change in strath height occurs near the CRF where the Qt5 strath height increases abruptly from ~20 m to ~45 m above the channel, however, the displacement of the Qt5 terrace tread across the fault is much less (~4-7 m). Further downstream, within the Montesano Formation, Qt5 strath height gradually varies between ~5 m and ~27 m above the modern channel and roughly parallels the terrace tread.

A key observation from the strath surveys is the presence of a thin (~2-3 m) lacustrine strath overlying basalt bedrock in Qt4b within the lower gorge (location shown in Fig. 5a, location of WYN-11 and WYN-12 in Fig. 3). This lacustrine unit strongly resembles the expansive lacustrine unit north of the lower gorge that forms straths within at least Qt6, Qt7, and Qt8 (Fig. 3b). Carson (1970) interpreted the lacustrine deposits upstream of the lower gorge as originating from Grisdale dammed glacial lakes.

4.2 Optically stimulated luminescence ages

In total, we collected and analyzed 20 OSL samples from 11 different locations (Table 2, Figs. S1-S20). Six samples displayed very low luminescence, and are therefore not used in the following analyses. The largest concern with OSL dating in fluvial environments is the potential for partial bleaching (resetting), resulting in artificially old burial ages. Nearly all samples, excluding WYN-07 and WYN-08, were collected in pairs (e.g., WYN-09 and WYN-10 are pairs) from the same exposure (or in very close proximity) within the same terrace. This double-sample method was employed to increase the chance of identifying partially bleached samples,

account for potential low luminescence, and reduce age uncertainty caused by the lack of outside age controls (such as radiocarbon dating) available in other drainages (Wyshnytzky et al., 2014).

Many of the collected sample pairs yielded measureable luminescence for only one sample of the pair (Table 2). WYN-19 yields a burial age for Qt8 of 7.4 ± 1.8 ka, and WYN-04 yields an age of 11.9 ± 3.2 ka for Qt7. Of the successfully dated samples collected in unit Qt5, two are from the same outcrop. These paired samples (WYN-16 and WYN-15) yield ages of 18.7 ± 3.6 ka and 11.1 ± 3.0 ka, respectively. These ages generally agree with samples from other outcrops of Qt5, which were calculated at 14.3 ± 3.7 ka (WYN-07), 14.7 ± 5.3 ka (WYN-06), and 31.8 ± 5.3 ka (WYN-08). Samples from Qt4 yield estimated ages of 32.0 ± 10.0 ka (WYN-12) and 41.8 ± 12.4 ka (WYN-17). Unit Qt3 sample ages include 37.2 ± 11.8 (WYN-02), and paired sample ages of 35.0 ± 10.7 ka (WYN-09) and 48.5 ± 30.9 (WYN-10). Samples from the same outcrop of Qt2 yield ages of 47.7 ± 12.3 ka (WYN-13) and 59.3 ± 20.9 ka (WYN-14), which overlap within error, but large uncertainties in both samples poorly constrain the timing of Qt2 deposition.

Combining the OSL ages with the surveyed strath heights yields differential incision rate values along the length of the valley. Other studies in the Clearwater use incision rates to estimate tectonic uplift rates (Pazzaglia and Brandon, 2001). We focus here primarily on the spatial patterns of incision, but the range of Qt5 strath heights corresponds to incision rates of 0.4 ± 0.3–1.8 ± 0.3 mm/yr using the calculated average OSL age for this deposit (14.7 ± 2.3 ka) (Fig. 5c, Table 4).

4.3 Scarp profiles

Mapping also reveals numerous fault scarps of the CRF, a northeast-striking, upper-plate reverse structure as trenched in other locations (Fig. 2) (Walsh and Logan, 2007). The fault trace is relatively continuous and generally displays northwest facing scarps with <5 m of vertical displacement. The western mapped trace reveals a 2.5 km long, 150 m wide pull-apart basin structure across a subtle left step in the CRF, consistent with a component of sinistral motion, however, other geomorphic indicators of lateral slip, such as offset stream channels, are not present (Plate 1). The orientation of the fault trace as it crosses terrace risers is consistent with a steep, south-east dipping fault plane (e.g., 5.5 km valley distance, within Qt4, Plate 1). At river level, the fault trace coincides with the emergence of a deep, steep-sided inner gorge (Fig. 3b), referred to here informally as the lower gorge.

The CRF offsets several sub-planar terrace treads suitable for measuring vertical separation. We use topographic profiles (A-S) to calculate vertical separation on the northern segment of the fault scarp (Fig. 6). The scarp displaces terraces Qt4, Qt6, Qt6b, and Qt7 and vertical separation varies from ~0.9 +0.4/-0.5 m to 8.0 ± 1.3 m (Figs. 5 and 6, Table 3). Using OSL ages from this study, we calculate vertical separation rates between 0.03 +0.02/-0.01 mm/yr to 0.3 ± 0.1 mm/yr (Fig. 7 and Table 3). A topographic profile on the southern segment of the fault trace (X-X') in unit Qt5 is shown in Figure 5c. Uncertainty in matching the Qt5 terrace across the CRF suggests vertical separation values of 4.3 ± 1.6 m or 7.7 ± 3.5 m, depending on the continuity of the northern terrace tread with Qt5 and Qt5b south of the fault. These values yield vertical separation rates of 0.3 + 0.2/-0.1 mm/yr to 0.5 + 0.4/-0.2 mm/yr, respectively. The lower vertical separation rate (~0.3 mm/yr) is consistent with the northern fault scarp estimated rates. We vary fault dip uniformly between 55°-85°, centered on 70° dip values measured from

Walsh and Logan, (2007). Using these values, the northern scarp (profiles A-S) reverse dip-slip rates range from 0.04 +0.04/-0.01 mm/yr to 0.3 ± 0.1 mm/yr. The southern scarp (profile X-X') reverse dip-slip rates are calculated as 0.3 +0.2/-0.1 mm/yr and 0.5 +0.4/-0.2 mm/yr.

4.4 Boundary element method model

We use the BEM model to estimate the slip rate distribution on the CRF required to relieve stress imposed by Cascadia subduction zone coupling (Figs. 8 and 9). An assumption inherent in our BEM analysis is that all stress imposed on the CRF by Cascadia subduction zone coupling is relieved by CRF slip. The predicted uplift rates (Figs. 9 and 10) therefore reflect a time-averaging of annual contributions from Cascadia subduction zone coupling and distinct slip events of unknown recurrence interval on the CRF.

The model predicts south-side-up motion on the CRF, with estimated reverse slip rates of 0.04-0.47 mm/yr (Fig. 3). Closest to the Wynoochee River, estimated reverse slip is values are ~0.1-0.15 mm/yr. The lateral component of estimated slip rates on the CRF is up to 0.7 mm/yr of dextral motion. Both reverse and lateral slip generally reach peak values in the center of the longest segments and decrease near fault tips. Results from alternative model iterations with varying fault geometries, including a range of fault depths and connectivity, are described in Appendix B but are broadly similar with the results presented here.

Regionally, broad-scale uplift stemming from subduction zone coupling alone ranges from ~0.5-2.5 mm/yr, generally decreasing with distance from the plate boundary (Fig. 10a). Vertical separation rates from slip on the CRF range from 0.05-0.5 mm/yr (Fig. 10b). Importantly, the trace of the river flows through a local minimum in model-predicted CRF uplift, owing to the segmentation of the fault within the valley. We calculate combined uplift from both

subduction zone coupling and CRF slip along the valley profile line (Fig. 10c). Slip on the CRF affects uplift within ~10 km of the surface trace, shown as a slight peak in the uplift profile. Long-wavelength variations in valley uplift are largely a result of spatially variable coupling as the river meanders closer and further from the subduction zone margin.

We simulated several moderate (M_w 7.8) earthquakes on the Cascadia subduction zone to determine whether subduction earthquakes could produce stress fields favorable to the observed slip on the CRF. Simulated earthquakes reached 1 m peak slip with centroids varying along strike and depth of the subducting slab interface (Fig. 11). All simulated earthquakes produced regional stress fields favorable to normal slip, with varying magnitudes, on the CRF (Fig. 12). Larger magnitude earthquakes with similar slip patterns would not change the estimated sense of CRF slip.

5. Discussion

5.1 Geomorphic evolution of the Wynoochee River

Our OSL sample ages suggest terrace deposition correlates with increased sediment supply associated with glacial maxima, as seen in other Olympic Mountain drainages (Pazzaglia and Brandon, 2001; Wyshnytzky et al., 2014). The majority of dated terraces in the Wynoochee valley correspond to mid-late MIS 3 and late MIS 2, and correlate with other previously identified western Olympic Mountain and Washington Cascade alpine glacier advances (Fig. 13). The Qt7-Qt8 deposit ages correspond to small late MIS 2 advances in the western Olympic Mountains (Thackray, 2001; Wyshnytzky et al., 2014) and the Cascades (Porter and Swanson, 2008). Qt5 deposit ages mostly correlate with LGM advances in the Hoh River (Thackray, 2001) and South Fork Hoh River valleys (Wyshnytzky et al., 2014), the Washington Cascades (Booth

et al., 2003; Porter and Swanson, 2008), and the maximum Cordilleran ice sheet advance (Porter and Swanson, 1998). One Qt5 sample, however (WYN-08), is similar in age to Qt4 and Qt3, which may be a result of partial bleaching or reflect multiple, diachronous terrace deposits on the same strath. The Qt4 and Qt3 terrace ages generally correlate with mid-MIS 3 advances in the Hoh River valley (Thackray, 2001). Qt2 ages have large uncertainties, but may correlate with late MIS 4 advances in the Hoh and Queets valleys (Thackray, 2001). This sequence of terraces also generally agrees with glacial advance and terrace deposition timing inferred by Carson (1970), excepting the Mobray Drift (Qt2) that is much younger than the Salmon Springs advance in Puget Sound. Other studies suggest glaciations the Olympic and Cascade Mountains are moisture-driven and asynchronous with North American climate events, with the largest advances during ~31-34 ka and 60-125 ka (MIS 3 and 5) and less extensive advances during the LGM ~19-23 ka (MIS 2) (Thackray, 2008). Results from this study are consistent with this idea, revealing larger aggradation events at 30-40 ka and 50-60 ka, and considerably less extensive deposition during ~12-20 ka (Fig. 13).

We demonstrate the importance of valley aggradation, rock type, and isostatic rebound, in addition to tectonic uplift, in controlling terrace formation and incision. We interpret the lower gorge as predating at least the largest Grisdale advance (mid-late MIS 3). The presence of glacial-lacustrine deposits in the modern channel floor upstream of the lower gorge, as well as on high basalt terrace straths within the lower gorge, suggests cycles of incision, damming, and re-excavation of the river valley to a pre-existing channel profile (Fig. 14). Alternatively, lacustrine deposits in the lower gorge may have been vertically displaced from upstream lacustrine deposits by the CRF. However, the mismatch between terrace tread vertical separation and lacustrine strath vertical separation across the fault is inconsistent with fault slip (Fig. 6c). Additionally,

using OSL deposit ages and the lacustrine strath separation, CRF vertical separation rates approach ~1.7 mm/yr, far exceeding any geologic or modeled differential uplift in this study by 3-7 times. Re-excavation of the lower gorge is also consistent with an anomalous sequence of Qt5 meander terraces south of the CRF. Normally, terrace elevation decreases from the inner to outer meander, a result of outward migration of the point bar and cut bank. In the lower gorge, this sequence is reversed in several locations (e.g., Profile 2 in Fig 3b, Fig. 6a) indicating that the channel location is controlled by the fill deposits, which are easy to incise, rather than lateral meander migration processes. Both the lacustrine deposits and the anomalous river migration pattern imply that deposits on top of bedrock straths within the lower gorge represent the most recent period of canyon ice-damming and fill, channel abandonment, and incision through glacial lake sediments. Importantly, this implies strath deposit ages in at least the upper reaches of the river are much younger than strath planation timing.

The disagreement between ages results from sample WYN-08 (31.8 ± 5.3 ka) and results from all other Qt5 sample ages (average of 14.7 ± 2.3 ka) suggests either partial bleaching of WYN-08 or a diachronous gravel deposit in some Qt5 terraces. Variable terrace type (strath or fill) within the same unit (Qt5) along the valley also implies that strath planation may not occur at all places along the channel at the same time. The downstream reaches of Qt5 (>25 km valley distance, Fig. 5) have a characteristic strath appearance, with relatively thin gravel fill capping a bedrock erosional unconformity, while the upstream exposures are more typical of an outwash fill terrace. In the Clearwater River, Pazzaglia and Brandon (2001) suggest the channel quickly returns to a graded river profile following downstream aggradation, and vertical incision quickly propagates upstream as the entire terrace is abandoned. In the Wynoochee River, however, the reversed distribution of Qt5 strath and fill terraces, and the older WYN-08 age, suggests some

downstream reaches of Qt5 strath are capped by deposits from Qt5, Qt4 and Qt3. Strath reoccupation is also supported by the convergence of fill terrace treads Qt3 and Qt4 with the surface of Qt5 at ~25 km. Thus, the lower river profile strath location may have been relatively stable preceding the current interglacial period, but the upper Wynoochee River valley has likely seen several episodes of fill and excavation.

The pattern of upstream divergence (valley distance <30 km) for the Qt6-Qt8 strath terraces strongly resembles strath terraces in the Clearwater River, interpreted as a result of faster tectonic uplift near the Olympic Mountain interior (Pazzaglia and Brandon, 2001). We interpret that Qt6-Qt8 formation is a result of isostatic rebound, evidenced by the very short interval of deposit ages spanning the end of the Fraser glaciation. Uplift, caused by the Grisdale glacial retreat, forced incision into weak lacustrine deposits and formed an upstream-diverging series of terraces (Qt6-Qt8) in a relatively short period of time. The modern river profile upstream of the CRF, therefore, likely lies close to the pre-Grisdale channel profile, but the location of the pre-glacial river profile downstream of the lower gorge remains unclear or may not be preserved.

We attribute the downstream divergence of Qt5, Qt5b, and Qt5c terraces as evidence for potential base level change at the confluence with the Chehalis River. Carson (1970) proposed that the Chehalis may have been choked with sediment during formation of outwash terraces (Qt1, Qt2, Qt3, Qt4, and Qt5 in this study), elevating the local base level. As the sediment load decreased, the river mouth incised to match the new Chehalis River elevation. We agree with this interpretation, and propose that after deposition of Qt5, the river mouth elevation decreased due to a reduced sediment load from the Wynoochee River and adjacent drainages. The lowered base level created backward propagating incision, forming Qt5-Qt5c and the modern river profile.

5.2 Slip on the Canyon River fault

Several geomorphic features imply longevity of CRF slip and control on the Wynoochee River profile. The dramatic channel narrowing and bedrock knickpoint (Fig. 4) across the CRF are likely due to south-side-up reverse slip. Channel narrowing and increased steepness can increase the stream power and erosiveness of a river by focusing more energy on a smaller area (e.g., Finnegan et al., 2005) to accommodate differential uplift (Amos and Burbank, 2007). Alternatively, a change in rock type from relatively friable lacustrine to much harder basalt could cause both channel narrowing and steepening without differential uplift. Spatial coincidence of the CRF with channel narrowing rather than with rock type change implies channel width responds to reverse slip on the CRF. This process may have positive feedbacks: as the fault slips, it exhumes harder rocks from depth, forcing the channel to narrow and steepen more. Additionally, the Wynoochee River valley occupies a local minimum in uplift related to CRF slip predicted from the BEM model (Fig. 10b), suggesting a long-lived fault controlled river location and CRF slip history in this location.

On the northern scarp profiles, the largest vertical separation occurs within unit Qt6b (scarps L and M, Figs. 5 and 6) and is 2-3 times the vertical displacement of units Qt4 and Qt6 (scarps N, O, P, Q, and A, B, C, D, respectively), which are vertically higher, and therefore mapped as older, than Qt6b. We see at least three possibilities to explain this apparent discrepancy. First, terrace Qt4 contains much thicker fill deposits than terraces Qt6, Qt6b and Qt7, decreasing the preservation potential of surface displacement. Alternatively, vertical displacement of Qt4 (scarps N-Q) may be partially obscured by more recent alluvial deposition. Topographic contours on Qt4 reveal an active alluvial fan on the up-thrown side of the fault scarp as well as a small channel roughly following the scarp from east to west (Fig. 6a). These

features could deposit sediment on both sides of the fault, decreasing or obscuring the scarp height. Finally, the scarp could be of fluvial origin, and the up-thrown side of Qt6b represents a slightly older terrace. This explanation requires the river to have eroded a cut bank along the fault to form the edge of the terrace riser, as is observed elsewhere on modern cut banks (Fig. 6a). This hypothesis implies that profiles L and M record a combination of terrace riser height and fault displacement, and cannot be used in slip analyses.

We consider it unlikely for an earthquake to displace Qt6b on the eastern side of the valley without displacing Qt6 ~700 m to the west, and favor the interpretation that profiles L and M cross a combined fluvially modified and fault-displaced scarp. However, we also consider it likely that post-earthquake deposition has occurred on Qt4, and therefore displacement measurements of profiles N to Q are considered minima.

Walsh and Logan (2007) estimate one earthquake occurring at ~1.8 ka elsewhere along the CRF, with net vertical separation of 3.35 m. Therefore, small vertical separation values (<3 m) from profiles A-K may also be from a single earthquake, perhaps the same ~1.8 ka event (Fig. 7). Because the scarp profiles N-Q record minimum vertical separation, terrace Qt4 may not record all co-seismic displacement since terrace formation ~40-50 ka. Small vertical separation values imply that the CRF may have a very long recurrence interval. Assuming the Walsh and Logan (2007) trench preserves one event, model-estimated vertical separation rates of 0.5 mm/yr imply a ~7 kyr recurrence interval. Alternatively, slip on the CRF may occur in more frequent, but smaller displacement events. More paleoseismic information is needed to accurately resolve earthquake recurrence on the CRF.

The BEM-estimated differential uplift rates across the CRF within the Wynoochee valley (0.05-0.2 mm/yr) (Fig. 9) agree with estimated vertical separation rates from offset terraces in

profiles A-Q (0.03-0.3 mm/yr) (Fig. 7), lower estimates from the southern CRF scarp (~0.3 mm/yr), as well as post-LGM vertical uplift rates from the Saddle Mountain fault zone (~0.2 mm/yr) (Barnett et al., 2015). The predicted component of dextral slip on the CRF from the BEM model, however, does not match the observation of sinistral-reverse slickenlines in a trench ~10 km to the east (Walsh and Logan, 2007). Importantly, much of the lateral motion on the CRF estimated by the model likely results from the dip-slip component of plate convergence in the coupling distribution (Fig. 8), thought to be reversed as elastic strain during megathrust earthquakes. Additionally, Barnett et al. (2015) concluded that sinistral slip along strands of the Saddle Mountain fault zone was small, due to a lack of geomorphic indicators such as offset stream channels. As such, we focus here on predicted rates of reverse motion on the CRF driven by subduction zone coupling. This overall pattern compares well with clear geomorphic evidence of long-term, south-side-up reverse motion on the CRF (Fig. 6). That said, we also note the potential for spatially and perhaps temporally variable slip in this region, given observations of both dextral and sinistral-reverse motion on the Saddle Mountain faults (Witter et al., 2008; Barnett et al., 2015) and normal slip on the Frigid Creek fault to the east (Blakely et al., 2009) (Fig. 1).

5.3 Implications for Cascadia forearc topographic development

Similarities in rates and patterns of Late Pleistocene faulting and incision and the predicted deformation from modeled megathrust coupling suggest that contemporary patterns of interseismic strain may contribute to permanent forearc deformation. Marked similarities exist between model-predicted kinematics and vertical separation rates and the observed deformation in offset terrace treads. Additionally, the time-averaged regional uplift pattern from the BEM

resembles longer-term incision preserved in strath terraces. Lacustrine deposits and terrace aggradation mask the pattern of incision in the Wynoochee River by obscuring the paleo-channel bedrock floor location. However, the preserved Qt5 strath profile between 20-40 km reveals patterns of long-term strain similar to the modeled regional uplift profile (Fig. 10c), possibly reflecting the faster coupling-related uplift than elsewhere in the valley.

The degree to which fluvial downcutting recorded by the Qt5 strath (Fig. 5) reflects long and shorter-term uplift remains complicated by a number of factors. In particular, given the prevalence of aggradational fills and clear evidence for repeated glaciation, particularly in the upper basin (Carson, 1970), some component of incision may result from glacial isostatic adjustment. Changes in glacial loading from local alpine glaciers and/or the Puget Lobe of the Cordilleran ice sheet (<35 km to the east; Fig. 1) (Thorson, 1989) could induce apparent gradients in incision depending on the timing of strath cutting and subsequent terrace abandonment (Litchfield and Berryman, 2006). Effects of the Cordilleran ice sheet in the southern Olympic Mountains, however, are largely unstudied. We expect isostatic adjustment effects from the Cordilleran ice sheet to decrease from north to south, based on decreased ice sheet thickness (Thorson, 1989), short-lived maximum extent of the Cordilleran ice, and rapid ice retreat (Booth et al., 2003). Ice removal effects in Olympic Mountain interior are also unknown, but alpine-ice isostatic rebound and incision should also decrease to the south in the Wynoochee valley. Additionally, the prevalence of bedrock incision along the length of the trench-parallel Wynoochee River (Fig. 5c), in contrast to the upstream increase in incision along the trench-normal Clearwater River (Fig. 1), might reflect Wynoochee River base level lowering. As such, we do not ascribe meaning to the absolute rate of incision with respect to vertical

tectonic motion, as done in the Clearwater drainage (Pazzaglia and Brandon, 2001); however, overall patterns of incision may still yield clues to long-term differential uplift.

In the lower reaches of the river, where Qt5 terraces have a more characteristic strath appearance and thin gravel deposits, the incision record may be more straightforward to interpret. Neither isostasy nor base level changes are likely to produce the broad, ~15-20 m warping of the Qt5 terrace strath in the lower Wynoochee River (Fig. 5c). The elevated portion of the Qt5 strath generally coincides with a complicated series of previously mapped bedrock fault and fold segments (Logan, 2003), but there are no visible fault scarps in the lidar. This localized uplift could reflect deformation from a margin-normal structure, such as the Kalaloch syncline (Thackray, 1998) and the hypothesized fold in the lower Clearwater River (Pazzaglia and Brandon, 2001). Although this feature in the Qt5 strath could reflect motion on a blind upper-plate fault, we note the similarity between this zone of accelerated incision and locally high interseismic uplift along the Wynoochee River profile predicted by the BEM model (Fig. 10c). Combined with the overall location of the Wynoochee valley within a regional low in interseismic uplift (Fig. 10b), controlled in part by the CRF, this spatial coincidence leaves open the possibility that long-term terrace downcutting mimics short-term permanent strain. This result resembles previous findings based on geomorphic observations in the Oregon forearc of the CSZ (Kelsey et al., 1994; Personius, 1995).

The similarities in slip and potentially incision between the model and the fluvial terrace record may in turn imply spatial stability of Cascadia subduction zone coupling from short to at least intermediate-term time scales. If subduction zone coupling were instead temporally variable, inconsistent interseismic strain would result in variable CRF slip and regional

deformation, and therefore a greater disagreement between the modeled and geologic deformation.

Finally, results from this study suggest that interseismic stress alone can cause upper plate fault slip in the Cascadia forearc. The match in slip on the CRF between the geomorphic record and the BEM implies that no additional source of stress, such as forearc migration, is required to produce the observed slip on the CRF. However, other sources of stress may contribute to the observed deformation if the permanent component of Cascadia interseismic strain is smaller than estimated here (e.g., incomplete and/or heterogeneous stress drop on the CRF). Therefore, forearc deformation, including longer-term arc-parallel shortening manifested as reverse faulting and broad scale folding, may reflect permanent subduction zone strain and relatively stable coupling. Hence, heterogeneity in uplift along the Cascadia forearc could be expressions of long-lived spatial variations in plate coupling.

6. Conclusions

Based on geomorphic mapping, strath terrace surveys, and optically stimulated luminescence dating in the Wynoochee River valley, we find similarities between the intermediate-term fault slip and incision record and short-term deformation from a modeled regional uplift and slip on the Canyon River fault produced from interseismic stress on the Cascadia subduction zone. Our OSL results yield terrace ages groupings of ~7-12 ka, ~14-18 ka, ~30-45 ka, and ~50-60 ka, consistent with alpine glaciations elsewhere in the Olympic and Cascade Mountains. Measured fault slip rates from the geomorphic record agree with modeled results, both yielding vertical separation rates of ~0.1-0.3 mm/yr in the valley, with estimated model vertical uplift rates up to 0.4 mm/yr elsewhere on the fault. Additionally, the Wynoochee

River valley shows signs of repeated glacial damming and re-excavation, obscuring the incision record and long-term uplift history. Therefore, we provide an example where terrace deposits do not provide a maximum age for bedrock incision, and instead reflect a younger resurfacing of a long-lived geomorphic feature. Incision distributions may mimic tectonic uplift in some portions of the valley, but incision rates are not correlative to tectonic rates. Calculating incision rates to estimate uplift in other glacially-influenced rivers may result in artificially fast rates.

The agreement between short-term modeled slip and the intermediate-term geologic record indicates that uplift, topographic development, and deformation in the Cascadia forearc may be in part controlled by subduction zone coupling. We see evidence that interseismic stress alone can drive upper plate fault slip, and potentially broad, aseismic folding. Additionally, similarities between patterns of short-term interseismic strain and the geologic record imply a long-term stability in coupling greater than the duration of the subduction zone earthquake cycle. Thus, interseismic strain in the forearc above subduction zones may not be entirely elastic and a component of deformation remains after subduction zone earthquakes. This relationship also implies that long-term upper plate faulting and variations in uplift along the length of the Cascadia forearc may be integrally linked to a pattern of temporally stable subduction zone coupling. Therefore, Cascadia forearc topography partially arises from margin normal shortening manifested on upper plate faults and folds, driven by interseismic stress. Additional slip information on other upper plate faults, as well as comparisons of modeled deformation elsewhere in the forearc, are necessary to further test these relationships.

Appendix A: Unit descriptions

Qt6(b, c), Qt7(b, c) and Qt8(b, c)

All generations of Qt6, Qt7, and Qt8 are interpreted to be relatively young due to the preservation of channel migration patterns on the tread, visible in the lidar DEM. The terrace strath is usually within a few meters of the surface of the tread. Exposures upstream of the CRF show lacustrine deposits forming the strath. Fill material consists of primarily rounded cobbles and medium gravel with cross-bedding, and very small amounts of sand between foresets. Clasts are minimally cemented.

Qt5, Qt5b, and Qt5c

All generations of Qt5 have virtually no preserved channel migration patterns preserved on the tread visible in the lidar DEM. The bedrock varies from lacustrine, basalt, and Montesano Formation. These terraces have highly variable fill thickness. In some locations, the terrace is primarily bedrock with <1 m fill on top, in others, it has 10's of meters of fill, deep enough to maintain a gravel pit for the logging operations. Locations with thicker fill may also have deeply incised post-deposition stream channels. This terrace is expansive and the most continuous terrace. Most exposures show fill comprised of primarily rounded cobbles and pebbles with cross-bedding, with evidence of buried soils visible in thicker fill locations. The fill deposits are weakly to moderately cemented together.

Qt4 and Qt4b

Qt4 has very similar surface morphology to Qt5 but generally has much thicker fill, which in some locations is at least 35 m thick. The terrace tread surface is relatively smooth, with no preserved channel migration patterns visible in the lidar DEM. Some locations, such as near the CRF, have been heavily incised by post-deposition stream channels. The fill material

generally consists of cross-bedded cobbles and gravels of varying sizes, with some sand between the foresets. Qt4a only exists upstream of the CRF on the east side of the valley and as preserved meander cutoffs at high elevations in the lower gorge. The meander cutoff terraces have almost no fill below the tread. The fill material generally consists of cross-bedded cobbles and gravels of varying sizes, with some sand between the foresets, and is weakly-moderately cemented.

Qt3

The Qt3 tread surface is smooth and lacks any original channel morphology visible in the lidar, but is incised by modern stream channels. The extent is partially inferred from Carson's (1970) mapping, since some of the borders are not contained within the lidar DEM. Fill thickness varies, with one field exposure in a river cut bank showing at least 45 m of fill deposits. Clasts within the fill are moderately to well cemented together, making OSL sample collection difficult. Most exposures consisted primarily of cross-bedded rounded cobbles and gravels, with small amounts of interbedded sands

Grisdale till (Qgt)

The Grisdale Till surface morphology is defined in the lidar DEM by hummocky and kettle and kame topography with sub-parallel, often curved, rounded linear ridges (mapped as moraines). In the field, Grisdale Till exposures consisted of diamicton, layered and massive clays, sand, cobbles, and coarse gravels. Some regions contained deformed internal layering structures, but often any internal organization showed signs of disrupted by post or syn-depositional tilting and folding. The Grisdale till lacks undeformed layered, cross-bedded gravels and sand.

Qt2

The Qt2 terraces are identified largely from Carson, (1970), as much of the extent lies outside of the lidar data. The surface lacks definition and has very rounded terrace risers and is often incised by post-depositional streams, indicating a relatively old age compared to other terraces. Exposures showed thick gravel deposits with cross-bedding, and is well cemented, making it difficult to collect OSL samples.

Mobray till (Qmt)

The Mobray till extent is largely defined by Carson's mapping, because the lidar does not extend to most of the boundaries. The DEMs reveal some evidence of very rounded linear ridges (mapped as moraine crests). There was no field reconnaissance of Mobray till.

Qt1

The extent of Qt1 is partially identified by height above the modern channel and from Carson, (1970), as much of the extent lies outside the lidar data. Surface morphology is heavily rounded and lacks clear, broad, flat terrace risers as with other terraces. The risers often have post-depositional stream incision and very rounded terrace risers.

Appendix B: Alternative boundary element model iterations

We tested alternative fault configurations using the BEM to understand how uncertainty in fault geometry affects modeled slip on the CRF. We varied fault depth and fault connectivity to evaluate potential differences in dip-slip and uplift rates.

Changes in fault projection depth: We tested fault depth variation, projecting the surface trace to 5 km, 10 km, or 15 km depth. The predicted peak slip rate magnitude along the CRF is dependent on fault depth. The maximum dip-slip rates for 5, 10, and 15 km fault depths are 0.4

mm/yr, 0.65 mm/yr, and 0.8 mm/yr, respectively. The slip distribution along the fault plane remains similar, but slip magnitudes scale with depth.

Changes in fault connectivity: To test alternative fault connectivity at depth, we connected the two largest fault segments into one fault plane and left two smaller mapped segments disconnected. Connecting the two largest fault segments partitions slip off of small segments, increasing peak slip in those regions. For faults projected to the same depth, the disconnected fault slips more on small segments than if the faults are connected. Additionally, the uplift pattern becomes more uniform. With a disconnected fault trace projected to 10 km depth, uplift is very low (~0.1-0.15 mm/yr) near the Wynoochee River valley, a stark contrast to the maximum values nearing ~0.5 mm/yr. The minimum uplift in the Wynoochee River valley with a continuous fault trace (~0.2-3 mm/yr) is not as pronounced as in the segmented model, but it remains a local minimum nonetheless.

Scaling fault depth with fault length: We also modeled slip on the CRF with variable fault depth along the trace. Shorter fault segments were projected to 5 km depth, while longer fault segments were projected to 10 km fault depth. Using this method, we modeled slip for a disconnected fault trace as well as connecting the two largest segments. Variable fault depth did not significantly affect fault slip rates or uplift patterns. Therefore, we conclude that although the fault geometry is uncertain, the first-order conclusions drawn in the main text are insignificantly affected by perturbations to the geometry.

References

Allmendinger, R.W., González, G., Yu, J., Hoke, G., Isacks, B., 2005. Trench-parallel shortening in the Northern Chilean Forearc: Tectonic and climatic implications. Geol. Soc. Am. Bull. 117, 89–104. doi:10.1130/B25505.1

Amos, C.B., Burbank, D.W., 2007. Channel width response to differential uplift. J. Geophys. Res. Earth Surf. 112, F02010. doi:10.1029/2006JF000672

Aron, F., Allmendinger, R.W., Cembrano, J., González, G., Yáñez, G., 2013. Permanent fore-arc extension and seismic segmentation: Insights from the 2010 Maule earthquake, Chile. J. Geophys. Res. Solid Earth 118, 724–739. doi:10.1029/2012JB009339

Atwater, B.F., Hemphill-Haley, E., 1997. Recurrence intervals for great earthquakes of the past 3,500 years at northeastern Willapa Bay, Washington (USGS Numbered Series No. 1576), Professional Paper. U.S. G.P.O. ; Information Services [distributor],.

Balco, G., Finnegan, N., Gendaszek, A., Stone, J.O.H., Thompson, N., 2013. Erosional response to northward-propagating crustal thickening in the coastal ranges of the U.S. Pacific Northwest. Am. J. Sci. 313, 790–806. doi:10.2475/11.2013.01

Barnett, E.A., Sherrod, B.L., Hughes, J.F., Kelsey, H.M., Czajkowski, J.L., Walsh, T.J., Contreras, T.A., Schermer, E.R., Carson, R.J., 2015. Paleoseismic Evidence for Late Holocene Tectonic Deformation along the Saddle Mountain Fault Zone, Southeastern Olympic Peninsula, Washington. Bull. Seismol. Soc. Am. 105, 38–71. doi:10.1785/0120140086

Bevis, M., Kendrick, E., Smalley, R., Brooks, B., Allmendinger, R., Isacks, B., 2001. On the strength of interplate coupling and the rate of back arc convergence in the central Andes: An analysis of the interseismic velocity field. Geochem. Geophys. Geosystems 2, 1067. doi:10.1029/2001GC000198

Bilham, R., Larson, K., Freymueller, J., 1997. GPS measurements of present-day convergence across the Nepal Himalaya. Nature 386, 61–64. doi:10.1038/386061a0

Blakely, R.J., Sherrod, B.L., Hughes, J.F., Anderson, M.L., Wells, R.E., Weaver, C.S., 2009. Saddle Mountain fault deformation zone, Olympic Peninsula, Washington: Western boundary of the Seattle uplift. Geosphere 5, 105–125. doi:10.1130/GES00196.1

Booth, D.B., Troost, K.G., Clague, J.J., Waitt, R.B., 2003. The Cordilleran Ice Sheet, in: A.R. Gillespie, S.C.P., and B.F. Atwater (Ed.), Developments in Quaternary Sciences, The Quaternary Period in the United States. Elsevier, pp. 17–43.

Brandon, M.T., Roden-Tice, M.K., Garver, J.I., 1998. Late Cenozoic exhumation of the Cascadia accretionary wedge in the Olympic Mountains, northwest Washington State. Geol. Soc. Am. Bull. 110, 985–1009. doi:10.1130/0016-7606(1998)110<0985:LCEOTC>2.3.CO;2

Brocher, T.M., Parsons, T., Blakely, R.J., Christensen, N.I., Fisher, M.A., Wells, R.E., 2001. Upper crustal structure in Puget Lowland, Washington: Results from the 1998 Seismic Hazards Investigation in Puget Sound. J. Geophys. Res. Solid Earth 106, 13541–13564. doi:10.1029/2001JB000154

Bucknam, R.C., Sherrod, B., Elfendahl, G., 1999. A fault scarp of probable Holocene age in the Seattle fault zone, Bainbridge Island, Washington [abstract]. Seismol. Reseach Lett. 70, 223.

Bull, W.B., 1991. Geomorphic responses to climatic change. Oxford University Press.

Carson, R., 1970. Quaternary Geology of the South-Central Olympic Peninsula, Washington (Dissertation). University of Washington.

Clowes, R.M., Brandon, M.T., Green, A.G., Yorath, C.J., Brown, A.S., Kanasewich, E.R., Spencer, C., 1987. LITHOPROBE—southern Vancouver Island: Cenozoic subduction complex imaged by deep seismic reflections. Can. J. Earth Sci. 24, 31–51. doi:10.1139/e87-004

Crouch, S.L., Starfield, A.M., 1983. Boundary Element Methods in Solid Mechanics: With Applications in Rock Mechanics and Geological Engineering, 1 edition. ed. George Allen & Unwin, London ; Boston.

Davis, E.E., Hyndman, R.D., 1989. Accretion and recent deformation of sediments along the northern Cascadia subduction zone. Geol. Soc. Am. Bull. 101, 1465–1480. doi:10.1130/0016-7606(1989)101<1465:AARDOS>2.3.CO;2

Finnegan, N.J., Roe, G., Montgomery, D.R., Hallet, B., 2005. Controls on the channel width of rivers: Implications for modeling fluvial incision of bedrock. Geology 33, 229–232. doi:10.1130/G21171.1

Finnegan, N.J., Schumer, R., Finnegan, S., 2014. A signature of transience in bedrock river incision rates over timescales of 104-107 years. Nature 505, 391–394. doi:10.1038/nature12913

Fisher, G.B., Amos, C.B., Bookhagen, B., Burbank, D.W., Godard, V., 2012. Channel widths, landslides, faults, and beyond: The new world order of high-spatial resolution Google Earth imagery in the study of earth surface processes. Geol. Soc. Am. Spec. Pap. 492, 1–22. doi:10.1130/2012.2492(01)

Gallen, S.F., Pazzaglia, F.J., Wegmann, K.W., Pederson, J.L., Gardner, T.W., 2015. The dynamic reference frame of rivers and apparent transience in incision rates. Geology 43, 623–626. doi:10.1130/G36692.1

González, G., Salazar, P., Loveless, J.P., Allmendinger, R.W., Aron, F., Shrivastava, M., 2015. Upper plate reverse fault reactivation and the unclamping of the megathrust during the 2014 northern Chile earthquake sequence. Geology 43, 671–674. doi:10.1130/G36703.1

Huntley, D.J., Godfrey-Smith, D.I., Thewalt, M.L.W., 1985. Optical dating of sediments. Nature 313, 105–107. doi:10.1038/313105a0

Hyndman, R.D., Wang, K., 1993. Thermal constraints on the zone of major thrust earthquake failure: The Cascadia Subduction Zone. J. Geophys. Res. Solid Earth 98, 2039–2060. doi:10.1029/92JB02279

Kelsey, H.M., Engebretson, D.C., Mitchell, C.E., Ticknor, R.L., 1994. Topographic form of the Coast Ranges of the Cascadia Margin in relation to coastal uplift rates and plate subduction. J. Geophys. Res. Solid Earth 99, 12245–12255. doi:10.1029/93JB03236

Litchfield, N., Berryman, K., 2006. Relations between postglacial fluvial incision rates and uplift rates in the North Island, New Zealand. J. Geophys. Res. Earth Surf. 111, F02007. doi:10.1029/2005JF000374

Logan, R.L., 2003. Geologic map of the Shelton 1:100,000 quadrangle. Open File Report 2003-15.

Loveless, J.P., Pritchard, M.E., 2008. Motion on upper-plate faults during subduction zone earthquakes: Case of the Atacama Fault System, northern Chile. Geochem. Geophys. Geosystems 9, Q12017. doi:10.1029/2008GC002155

Marshall, S.T., Cooke, M.L., Owen, S.E., 2009. Interseismic deformation associated with three-dimensional faults in the greater Los Angeles region, California. J. Geophys. Res. Solid Earth 114, B12403. doi:10.1029/2009JB006439

Mazzotti, S., Dragert, H., Hyndman, R.D., Miller, M.M., Henton, J.A., 2002. GPS deformation in a region of high crustal seismicity: N. Cascadia forearc. Earth Planet. Sci. Lett. 198, 41–48. doi:10.1016/S0012-821X(02)00520-4

McCaffrey, R., King, R.W., Payne, S.J., Lancaster, M., 2013. Active tectonics of northwestern U.S. inferred from GPS-derived surface velocities. J. Geophys. Res. Solid Earth 118, 709–723. doi:10.1029/2012JB009473

McCrory, P.A., Blair, J.L., Oppenheimer, D.H., Walter, S.R., 2006. Depth to the Juan de Fuca slab beneath the Cascadia subduction margin: A 3-D model for sorting earthquakes.

Meade, B.J., 2010. The signature of an unbalanced earthquake cycle in Himalayan topography? Geology 38, 987–990. doi:10.1130/G31439.1

Meade, B.J., 2007. Present-day kinematics at the India-Asia collision zone. Geology 35, 81–84. doi:10.1130/G22924A.1

Meade, B.J., Loveless, J.P., 2009. Block Modeling with Connected Fault-Network Geometries and a Linear Elastic Coupling Estimator in Spherical Coordinates. Bull. Seismol. Soc. Am. 99, 3124–3139. doi:10.1785/0120090088

Merritts, D., Bull, W.B., 1989. Interpreting Quaternary uplift rates at the Mendocino triple junction, northern California, from uplifted marine terraces. Geology 17, 1020–1024. doi:10.1130/0091-7613(1989)017<1020:IQURAT>2.3.CO;2

Mitchell, C.E., Vincent, P., Weldon, R.J., Richards, M.A., 1994. Present-day vertical deformation of the Cascadia Margin, Pacific Northwest, United States. J. Geophys. Res. 991, 12257–12277. doi:10.1029/94JB00279

Murray, A.S., Olley, J.M., 2002. Precision and accuracy in the optically stimulated luminescence dating of sedimentary quartz: A status review. Geochronometria 21.

Nelson, A.R., Johnson, S.Y., Kelsey, H.M., Wells, R.E., Sherrod, B.L., Pezzopane, S.K., Bradley, L.-A., Koehler, R.D., Bucknam, R.C., 2003. Late Holocene earthquakes on the Toe Jam Hill fault, Seattle fault zone, Bainbridge Island, Washington. Geol. Soc. Am. Bull. 115, 1388–1403. doi:10.1130/B25262.1

Pazzaglia, F.J., Brandon, M.T., 2001. A Fluvial Record of Long-term Steady-state Uplift and Erosion Across the Cascadia Forearc High, Western Washington State. Am. J. Sci. 301, 385–431. doi:10.2475/ajs.301.4-5.385

Personius, S.F., 1995. Late Quaternary stream incision and uplift in the forearc of the Cascadia subduction zone, western Oregon. J. Geophys. Res. Solid Earth 100, 20193–20210. doi:10.1029/95JB01684

Porter, S.C., Swanson, T.W., 2008. 36Cl dating of the classic Pleistocene glacial record in the northeastern Cascade Range, Washington. Am. J. Sci. 308, 130–166. doi:10.2475/02.2008.02

Porter, S.C., Swanson, T.W., 1998. Radiocarbon Age Constraints on Rates of Advance and Retreat of the Puget Lobe of the Cordilleran Ice Sheet during the Last Glaciation. Quat. Res. 50, 205–213. doi:10.1006/qres.1998.2004

Quinault River Basin [lidar file], 2012. Seattle, WA: USGS and Puget Sound Lidar Consortium. Available: Puget Sound Lidar Consortium, Seattle, WA http://pugetsoundlidar.ess.washington.edu/index.htm (September 2014).

Rhodes, E.J., 2011. Optically Stimulated Luminescence Dating of Sediments over the Past 200,000 Years. Annu. Rev. Earth Planet. Sci. 39, 461–488. doi:10.1146/annurev-earth-040610-133425

Rittenour, T.M., 2008. Luminescence dating of fluvial deposits: applications to geomorphic, palaeoseismic and archaeological research. Boreas 37, 613–635. doi:10.1111/j.1502-3885.2008.00056.x

Savage, J.C., 1983. A dislocation model of strain accumulation and release at a subduction zone. J. Geophys. Res. Solid Earth 88, 4984–4996. doi:10.1029/JB088iB06p04984

Schanz, S.A., Montgomery, D.R., 2016. Lithologic controls on valley width and strath terrace formation. Geomorphology 258, 58–68. doi:10.1016/j.geomorph.2016.01.015

Sherrod, B., Gomberg, J., 2014. Crustal earthquake triggering by pre-historic great earthquakes on subduction zone thrusts. J. Geophys. Res. Solid Earth 119, 1273–1294. doi:10.1002/2013JB010635

Sherrod, B.L., Blakely, R.J., Weaver, C.S., Kelsey, H.M., Barnett, E., Liberty, L., Meagher, K.L., Pape, K., 2008. Finding concealed active faults: Extending the southern Whidbey Island fault across the Puget Lowland, Washington. J. Geophys. Res. Solid Earth 113, B05313. doi:10.1029/2007JB005060

Sherrod, B.L., Brocher, T.M., Weaver, C.S., Bucknam, R.C., Blakely, R.J., Kelsey, H.M., Nelson, A.R., Haugerud, R., 2004. Holocene fault scarps near Tacoma, Washington, USA. Geology 32, 9–12. doi:10.1130/G19914.1

Southwest Washington [lidar file], 2009. Portland, OR: Oregon Department of Geology and Mineral Industries. Available: Puget Sound Lidar Consortium, Seattle, WA http://pugetsoundlidar.ess.washington.edu/index.htm (September 2014).

Tabor, R., Cady, W., 1978. Geologic map of the Olympic Peninsula, Washington. U.S. Geological Survey Map I-994.

Thackray, G.D., 2008. Varied climatic and topographic influences on Late Pleistocene mountain glaciation in the western United States. J. Quat. Sci. 23, 671–681. doi:10.1002/jqs.1210

Thackray, G.D., 2001. Extensive Early and Middle Wisconsin Glaciation on the Western Olympic Peninsula, Washington, and the Variability of Pacific Moisture Delivery to the Northwestern United States. Quat. Res. 55, 257–270. doi:10.1006/qres.2001.2220

Thackray, G.D., 1998. Convergent-margin deformation of Pleistocene strata on the Olympic Coast of Washington, USA. Geol. Soc. Lond. Spec. Publ. 146(1), 199–211.

Thomas, A., 1993. Poly3D: A three-dimensional, polygonal element, displacement boundary element computer program with applications to fractures, faults, and cavities in the Earth's crust. Stanford University.

Thompson, S.C., Weldon, R.J., Rubin, C.M., Abdrakhmatov, K., Molnar, P., Berger, G.W., 2002. Late Quaternary slip rates across the central Tien Shan, Kyrgyzstan, central Asia. J. Geophys. Res. Solid Earth 107, 2203. doi:10.1029/2001JB000596

Thorson, R.M., 1989. Glacio-isostatic response of the Puget Sound area, Washington. Geol. Soc. Am. Bull. 101, 1163.

U.S. Geological Survey, 2016. Water Resources of the United StatesU.S. Geological Survey [WWW Document]. URL http://www.usgs.gov/water/ (accessed 3.30.16).

Walsh, T.J., Logan, R.L., 2007. Results of trenching the Canyon River fault, southeast Olympic Mountains, Washington.

Wang, K., Mulder, T., Rogers, G.C., Hyndman, R.D., 1995. Case for very low coupling stress on the Cascadia Subduction Fault. J. Geophys. Res. Solid Earth 100, 12907–12918. doi:10.1029/95JB00516

Washington State Department of Ecology, 2015, Washington State Well Log Viewer: https://fortress.wa.gov/ecy/waterresources/map/WCLSWebMap/default.aspx (November 2015).
Wegmann, K.W., Pazzaglia, F.J., 2002. Holocene strath terraces, climate change, and active tectonics: The Clearwater River basin, Olympic Peninsula, Washington State. Geol. Soc. Am. Bull. 114, 731–744. doi:10.1130/0016-7606(2002)114<0731:HSTCCA>2.0.CO;2
Wells, R.E., Weaver, C.S., Blakely, R.J., 1998. Fore-arc migration in Cascadia and its neotectonic significance. Geology 26, 759–762. doi:10.1130/0091-7613(1998)026<0759:FAMICA>2.3.CO;2
West, D.O., McCrumb, D.R., 1988. Coastline uplift in Oregon and Washington and the nature of Cascadia subduction-zone tectonics. Geology 16, 169–172. doi:10.1130/0091-7613(1988)016<0169:CUIOAW>2.3.CO;2
Witter, R.C., Givler, R.W., Carson, R.J., 2008. Two Post-Glacial Earthquakes on the Saddle Mountain West Fault, Southeastern Olympic Peninsula, Washington. Bull. Seismol. Soc. Am. 98, 2894–2917. doi:10.1785/0120080127
Wyshnytzky, C.E., Rittenour, T.M., Nelson, M.S., Thackray, G., 2014. Luminescence dating of late Pleistocene proximal glacial sediments in the Olympic Mountains, Washington. Quat. Int. 362, 116–123. doi:10.1016/j.quaint.2014.08.024

TABLE 1. STRATH SURVEY RESULTS

Valley distance (m)	Unit	Location		Elevation* (m)	Cover thickness at exposure (m)	Bedrock type	Cover material
		Lat (°N)	Long (°W)				
2098	Qt7	47.3743	123.6289	182.2 ± 0.9	n/a†	Till	Gravel
2306	Qt8b	47.3728	123.6305	176.0 ± 0.8	0.0	Basalt	None
5755	Qt7	47.3423	123.6409	163.5 ± 0.2	2.8	Lacustrine	Gravel and loess
5762	Qt7	47.3422	123.6408	162.7 ± 0.2	3.0	Lacustrine	Gravel and loess
5777	Qt7	47.3420	123.6406	161.1 ± 0.3	4.0	Lacustrine	Gravel
5785	Qt7	47.3420	123.6406	160.8 ± 0.2	5.2	Lacustrine	Gravel
5952	Qt6	47.3414	123.6453	177.6 ± 0.5	2.0	Lacustrine	Gravel
7389	Qt4	47.3299	123.6441	197.9 ± 1.0	<1.0	Basalt	Soil
7525	Qt5b	47.3294	123.6428	186.6 ± 0.9	<1.0	Basalt	Gravel
8140	Qt4b	47.3231	123.6427	194.1 ± 0.3	2.3	Lacustrine over basalt	Sand and gravel
8155	Qt4b	47.3229	123.6427	192.7 ± 0.4	2.0	Lacustrine over basalt	Sand and gravel
9259	Qt4	47.3136	123.6446	191.4 ± 0.3	1.0	Basalt	Gravel and loess
11040	Qt5b	47.2997	123.6529	139.7 ± 1.7	n/a†	Basalt	Montesano Fm.
11062	Qt5b	47.2994	123.6528	147.2 ± 3.2	2.9	Montesano Fm.	Gravel and loess
21000	Qt6	47.2115	123.6335	94.0 ± 1.1	3.5	Montesano Fm.	Gravel
21105	Qt6c	47.2117	123.6292	84.9 ± 0.3	1.5	Montesano Fm.	Gravel and soil
26695	Qt5	47.1649	123.6335	84.9 ± 0.2	5.1	Montesano Fm.	Gravel and loess
29607	Qt2b	47.1393	123.6372	79.0 ± 1.0	2.0	Montesano Fm.	Gravel
30524	Qt5	47.1293	123.6415	71.1 ± 1.3	3.3	Montesano Fm.	Gravel and soil
34102	Qt5	47.1045	123.6718	59.5 ± 0.7	1.0	Montesano Fm.	Gravel
34980	Qt5b	47.1005	123.6850	51.1 ± 0.2	3.2	Montesano Fm.	Gravel and loess
35059	Qt5b	47.0999	123.6854	50.8 ± 0.3	2.5	Montesano Fm.	Gravel and loess
35161	Qt5b	47.0989	123.6856	51.0 ± 0.3	2.5	Montesano Fm.	Gravel and loess
39756	Qt5	47.0586	123.6929	38.9 ± 0.2	3.1	Montesano Fm.	Gravel and loess
39803	Qt5	47.0582	123.6927	38.8 ± 0.2	3.1	Montesano Fm.	Gravel and loess
40372	Qt5c	47.0531	123.6920	34.7 ± 0.6	1.5	Montesano Fm.	Gravel
41332	Qt5	47.0441	123.6970	32.8 ± 0.6	n/a†	Montesano Fm.	Gravel and soil
42734	Qt5	47.0308	123.6989	30.5 ± 0.8	3.0	Montesano Fm.	Gravel and soil
43858	Qt5b	47.0208	123.6968	27.3 ± 1.8	1.8	Montesano Fm.	Soil

*Errors reported to 1 standard deviation.

†Cover thickness could not be measured in the field due to lack of visibility of the tread surface

Table 1. Strath survey data

TABLE 2. OPTICALLY STIMULATED LUMINESCENCE SAMPLE RESULTS

USU number*	Sample number†	Unit	Location		Elevation (m)	Burial depth (m)	Valley distance (km)	Number aliquots§	Dose rate (Gy/ka)	Equivalent dose (Gy)	Age# (ka)
			Lat (°N)	Long (°W)							
2051	WYN-01	Qt3	47.2256	123.6298	125	2.5	19.64	2 (4)	0.64 ± 0.04	16.3 ± 2.3	26.0 ± 4.0
2052	WYN-02	Qt3	47.2274	123.6323	121	2.0	19.34	12 (31)	0.72 ± 0.05	26.8 ± 8.0	37.2 ± 11.8
2053	WYN-03	Qt7	47.3422	123.6408	163	2.5	5.77	2 (4)	0.87 ± 0.05	12.3 ± 1.4	14.0 ± 2.0
2054	WYN-04	Qt7	47.3423	123.6409	165	2.5	5.75	13 (27)	0.87 ± 0.08	11.5 ± 2.9	11.9 ± 3.2
2055	WYN-05	Qt5	47.3399	123.6503	186	4.0	6.23	0 (4)	0.73 ± 0.07	±	±
2056	WYN-06	Qt5	47.3417	123.6507	194	1.0	6.03	17 (31)	1.00 ± 0.07	15.3 ± 5.3	14.7 ± 5.3
2057	WYN-07	Qt5b	47.1006	123.6848	57	3.5	34.96	14 (24)	0.71 ± 0.04	10.2 ± 2.4	14.3 ± 3.7
2058	WYN-08	Qt5	47.0583	123.6928	42	1.5	39.79	17 (31)	1.11 ± 0.06	35.2 ± 5.3	31.8 ± 5.3
2059	WYN-09	Qt3	47.3194	123.6366	223	3.0	8.60	13 (40)	0.56 ± 0.04	42.6 ± 5.6	35.0 ± 10.7
2060	WYN-10	Qt3	47.3215	123.6335	220	3.5	8.38	13 (57)	0.56 ± 0.04	27.4 ± 30.9	48.5 ± 30.9
2061	WYN-11	Qt4b	47.3231	123.6427	194	1.8	8.13	1 (4)	0.67 ± 0.04	31.6 ±	47.0 ±
2062	WYN-12	Qt4b	47.2229	123.6427	195	1.3	8.15	13 (27)	0.75 ± 0.05	24.1 ± 7.2	32.0 ± 10.0
2063	WYN-13	Qt2	46.9815	123.6557	44	1.0	49.38	17 (25)	1.24 ± 0.07	58.5 ± 13.9	47.7 ± 12.3
2064	WYN-14	Qt2	46.9817	123.6558	47	1.5	49.36	14 (24)	0.91 ± 0.05	54.2 ± 18.3	59.3 ± 20.9
2065	WYN-15	Qt5	47.2121	123.6355	107	2.0	20.91	9 (56)	0.87 ± 0.05	16.4 ± 2.7	18.7 ± 3.6
2066	WYN-16	Qt5	47.2121	123.6355	109	1.5	20.91	17 (40)	0.82 ± 0.05	9.0 ± 2.3	11.1 ± 3.0
2067	WYN-17	Qt4	47.3740	123.6147	253	1.5	1.17	21 (37)	0.95 ± 0.10	39.8 ± 11.1	41.8 ± 12.4
2068	WYN-18	Qt4	47.3740	123.6147	251	1.5	1.17	6 (31)	0.85 ± 0.05	15.5 ± 5.0	18.0 ± 6.2
2069	WYN-19	Qt8	47.3419	123.6407	162	1.5	5.82	19 (27)	1.12 ± 0.06	10.2 ± 2.4	7.4 ± 1.8
2070	WYN-20	Qt8	47.3413	123.6405	161	1.7	5.85	3 (4)	1.07 ± 0.06	15.9 ± 1.0	15.0 ± 2.0

Note: Errors reported to 2 standard deviations.

*USU sample number refers to the identifying number used at the Utah State University luminecense lab

†Sample number refers to the identifying number used in this study

§Aliquots includes total attempted (in parentheses) and accepted (outside parentheses).

#Ages calculated using a minimum age model

Table 2. OSL sample data and results. Samples are paired sequentially by location (e.g., WYN-01 and WYN-02 are location pairs). Greyed samples are low luminescence samples, and are not used in analyses.

TABLE 3. CANYON RIVER FAULT SCARP PROFILE RESULTS

Profile	Location		Elevation	Unit	Distance scarp	Fault dip range	Vertical separation (Vs)	Dip slip (Ds)	Ds rate	Vs rate	OSL	Age
	Lat (°N)	Long (°W)	(m)		(m)	(°)	(m)	(m)	(mm/yr)	(mm/yr)	sample	(ka)
A	47.3394	123.6470	179.4	Qt6	28	55-85	1.61 + 0.78 - 0.79	1.73 + 0.89 - 0.85	n/a†	n/a†	n/a†	n/a†
B	47.3397	123.6468	179.3	Qt6	68	55-85	1.56 + 0.41 - 0.41	1.69 + 0.50 - 0.47	n/a†	n/a†	n/a†	n/a†
C	47.3399	123.6466	179.7	Qt6	104	55-85	1.65 + 0.54 - 0.54	1.79 + 0.63 - 0.60	n/a†	n/a†	n/a†	n/a†
D	47.3404	123.6461	180.2	Qt6	160	55-85	1.70 + 0.59 - 0.60	1.83 + 0.70 - 0.66	n/a†	n/a†	n/a†	n/a†
E	47.3413	123.6445	168.1	Qt7	327	55-85	0.91 + 0.52 - 0.50	1.00 + 0.58 - 0.56	0.08 + 0.07 - 0.04	0.08 + 0.05 - 0.05	WYN-04	11.9 ± 1.6
F	47.3416	123.6442	167.9	Qt7	362	55-85	1.48 + 0.56 - 0.56	1.60 + 0.65 - 0.61	0.13 + 0.05 - 0.08	0.12 + 0.07 - 0.05	WYN-04	11.9 ± 1.6
G	47.3429	123.6402	167.5	Qt7	701	55-85	2.95 + 1.13 - 1.11	3.20 + 1.31 - 1.23	0.26 + 0.17 - 0.10	0.24 + 0.05 - 0.09	WYN-04	11.9 ± 1.6
H	47.3430	123.6396	167.9	Qt7	748	55-85	3.27 + 0.36 - 0.34	3.46 + 0.69 - 0.40	0.28 + 0.14 - 0.06	0.27 + 0.09 - 0.06	WYN-04	11.9 ± 1.6
I	47.3431	123.6390	167.9	Qt7	796	55-85	2.01 + 0.72 - 0.71	2.18 + 0.83 - 0.80	0.18 + 0.10 - 0.07	0.16 + 0.06 - 0.10	WYN-04	11.9 ± 1.6
J	47.3432	123.6385	167.8	Qt7	833	55-85	2.20 + 1.10 - 1.09	2.40 + 1.25 - 1.21	0.19 + 0.15 - 0.09	0.18 + 0.13 - 0.09	WYN-04	11.9 ± 1.6
K	47.3448	123.6332	214.2	Qt4	1274	55-85	2.46 + 0.84 - 0.57	2.63 + 1.02 - 0.64	0.07 + 0.05 - 0.06	0.06 + 0.06 - 0.02	WYN-17	41.8 ± 6.2
L	47.3450	123.6324	215.1	Qt4	1338	55-85	2.87 + 0.51 - 0.47	2.98 + 0.80 - 0.48	0.07 + 0.04 - 0.02	0.07 + 0.05 - 0.02	WYN-17	41.8 ± 6.2
M	47.3452	123.6318	217.0	Qt4	1392	55-85	1.77 + 0.37 - 0.35	1.91 + 0.47 - 0.42	0.04 + 0.03 - 0.01	0.05 + 0.03 - 0.02	WYN-17	41.8 ± 6.2
N	47.3454	123.6311	219.0	Qt4	1446	55-85	1.56 + 0.33 - 0.33	1.60 + 0.52 - 0.41	0.04 + 0.03 - 0.01	0.03 + 0.02 - 0.01	WYN-17	41.8 ± 6.2
O	47.3464	123.6264	287.0	Qt4	2138	55-85	6.09 + 2.97 - 2.39	6.50 + 2.77 - 2.76	0.15 + 0.11 - 0.07	0.14 + 0.11 - 0.06	WYN-17	41.8 ± 6.2
P	47.3464	123.6260	290.0	Qt4	2166	55-85	4.27 + 0.72 - 0.72	4.29 + 0.76 - 0.74	0.10 + 0.04 - 0.03	0.10 + 0.04 - 0.03	WYN-17	41.8 ± 6.2
X (A)	47.3321	123.6534	191.0	Qt5	n/a*	55-85	7.65 + 3.57 - 3.46	8.36 + 4.08 - 3.90	0.53 + 0.25 - 0.49	0.51 + 0.42 - 0.24	WYN-06	14.7 ± 2.6
X (B)	47.3321	123.6534	191.0	Qt5/5b	n/a*	55-85	4.27 + 1.62 - 1.61	4.67 + 2.03 - 1.94	0.29 + 0.26 - 0.12	0.28 + 0.22 - 0.11	WYN-06	14.7 ± 2.6

Note: Uncertainties reported to 1 standard deviation

OSL = optically stimulated luminescene

*Profile X was not along the same scarp as profiles A-Q, and therefore does not have a distance value.

†Terrace units do not have age constraints, so no rate values were calculated.

Table 3. Scarp profiling results results.

TABLE DR4. QT5 STRATH INCISION AND INCISION RATES			
Valley distance (km)	Strath height (m)	Qt5 age (ka)	Incision rate (mm/yr)
0.0	36.3 + 1.0 - 1.0	14.7 ± 2.29	2.47 + 0.3 - 0.3
2.0	31.7 + 1.0 - 25.0	14.7 ± 2.29	2.16 + 0.3 - 3.8
6.0	22.8 + 3.0 - 3.0	14.7 ± 2.29	1.55 + 0.5 - 0.5
7.3	20.8 + 3.5 - 3.5	14.7 ± 2.29	1.41 + 0.5 - 0.5
7.5	45.1 + 2.7 - 2.7	14.7 ± 2.29	3.07 + 0.7 - 0.7
8.1	45.7 + 2.2 - 2.2	14.7 ± 2.29	3.11 + 0.6 - 0.6
10.4	38.0 + 4.0 - 4.0	14.7 ± 2.29	2.59 + 0.9 - 0.9
11.1	29.0 + 3.5 - 3.5	14.7 ± 2.29	1.97 + 0.6 - 0.6
21.0	12.7 + 5.0 - 1.1	14.7 ± 2.29	0.86 + 0.4 - 0.2
26.6	23.4 + 0.2 - 0.2	14.7 ± 2.29	1.59 + 0.2 - 0.2
30.5	26.8 + 1.3 - 1.3	14.7 ± 2.29	1.82 + 0.3 - 0.3
34.1	24.1 + 0.7 - 0.7	14.7 ± 2.29	1.64 + 0.2 - 0.2
39.8	15.8 + 0.2 - 0.2	14.7 ± 2.29	1.07 + 0.2 - 0.2
41.3	12.5 + 0.6 - 0.6	14.7 ± 2.29	0.85 + 0.2 - 0.2
42.7	12.7 + 0.8 - 0.8	14.7 ± 2.29	0.86 + 0.2 - 0.2
43.8	12.8 + 6.0 - 1.8	14.7 ± 2.29	0.87 + 0.5 - 0.3
45.0	11.5 + 0.2 - 0.2	14.7 ± 2.29	0.78 + 0.2 - 0.2
46.0	9.7 + 0.2 - 0.2	14.7 ± 2.29	0.66 + 0.2 - 0.2
49.8	5.7 + 4.0 - 4.0	14.7 ± 2.29	0.39 + 0.3 - 0.3
Note: Errors reported to 1 standard deviation			

Table 4. Incision rate results

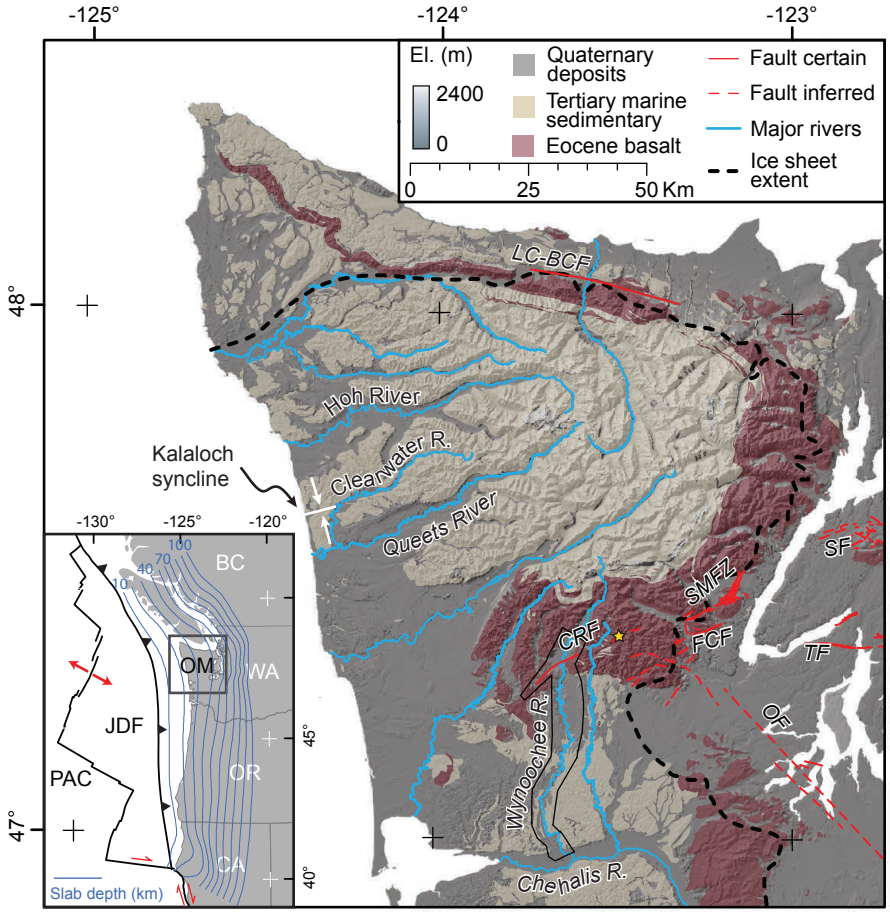

Figure 1. Map of the Olympic Peninsula showing ice sheet extent (Thorson, 1989), upper plate faults, and location of rivers. Generalized geologic units from Tabor and Cady (1978). Star denotes location of previous trench on the Canyon River fault (Walsh and Logan, 2007). Puget lowland faults are CRF, Canyon River fault; SMFZ, Saddle Mountain fault zone; FCF, Frigid Creek fault; SF, Seattle fault; TF, Tacoma fault; OF, Olympia fault (Barnett et al., 2015). Inset: Cascadia subduction zone with slab depth contours (McCrory et al., 2006). Red arrows = relative plate motions. JDF = Juan de Fuca plate, PAC = Pacific plate, OM = Olympic Mountains.

Figure 2 caption: Geomorphic mapping of the Wynoochee River Valley. A) Overview of the study area, with locations and ages of OSL samples. B) Detailed view of mapping and geomorphic changes as the Wynoochee River crosses the Canyon River fault. Note the channel narrowing and deep canyon south of the fault. Key shows correlations with mapping of Carson (1970).

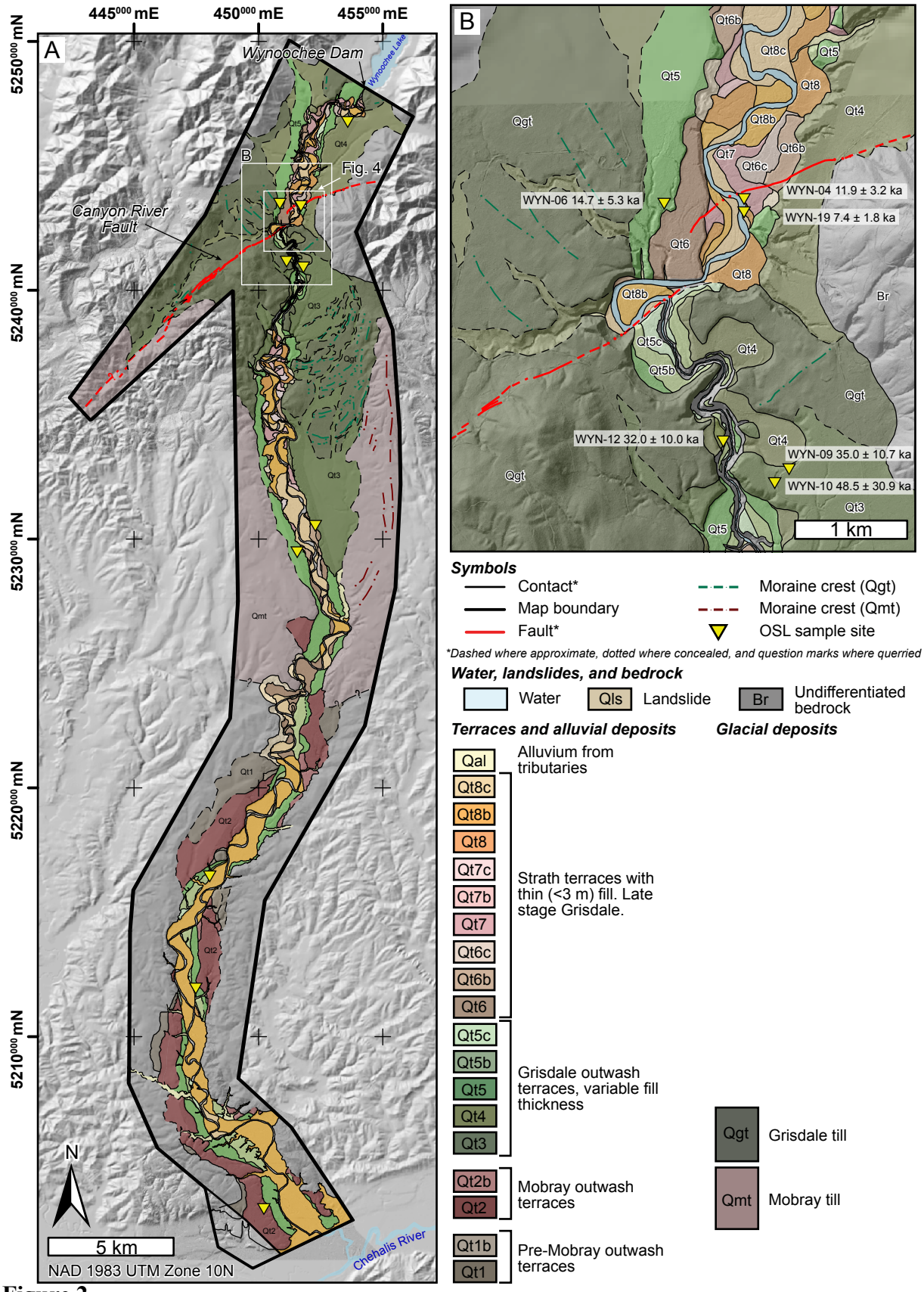
445000 mE
450000 mE
455000 mE
5250000 mN
5240000 mN
5230000 mN
5220000 mN
5210000 mN
A
Wynoochee Dam
Wynoochee Lake
B
Fig. 4
Canyon River Fault
Qt5
Qt4
Qt3
Qgt
Qmt
Qt1
Qt2
N
5 km
NAD 1983 UTM Zone 10N
Chehalis River
B
Qt6b
Qt8c
Qt5
Qt8
Qt4
Qgt
Qt8b
Qt7
Qt6b
Qt6c
WYN-06 14.7 ± 5.3 ka
WYN-04 11.9 ± 3.2 ka
WYN-19 7.4 ± 1.8 ka
Qt6
Qt8
Qt8b
Br
Qt5c
Qt4
Qt5b
Qgt
WYN-12 32.0 ± 10.0 ka
Qt4
WYN-09 35.0 ± 10.7 ka
Qgt
WYN-10 48.5 ± 30.9 ka
Qt3
Qt5
1 km
Symbols
Contact*
Map boundary
Fault*
Moraine crest (Qgt)
Moraine crest (Qmt)
OSL sample site
*Dashed where approximate, dotted where concealed, and question marks where querried
Water, landslides, and bedrock
Water
Qls
Landslide
Br
Undifferentiated bedrock
Terraces and alluvial deposits
Glacial deposits
Qal
Alluvium from tributaries
Qt8c
Qt8b
Qt8
Qt7c
Qt7b
Qt7
Qt6c
Qt6b
Qt6
Strath terraces with thin (<3 m) fill. Late stage Grisdale.
Qt5c
Qt5b
Qt5
Qt4
Qt3
Grisdale outwash terraces, variable fill thickness
Qgt
Grisdale till
Qt2b
Qt2
Mobray outwash terraces
Qmt
Mobray till
Qt1b
Qt1
Pre-Mobray outwash terraces

Figure 2.

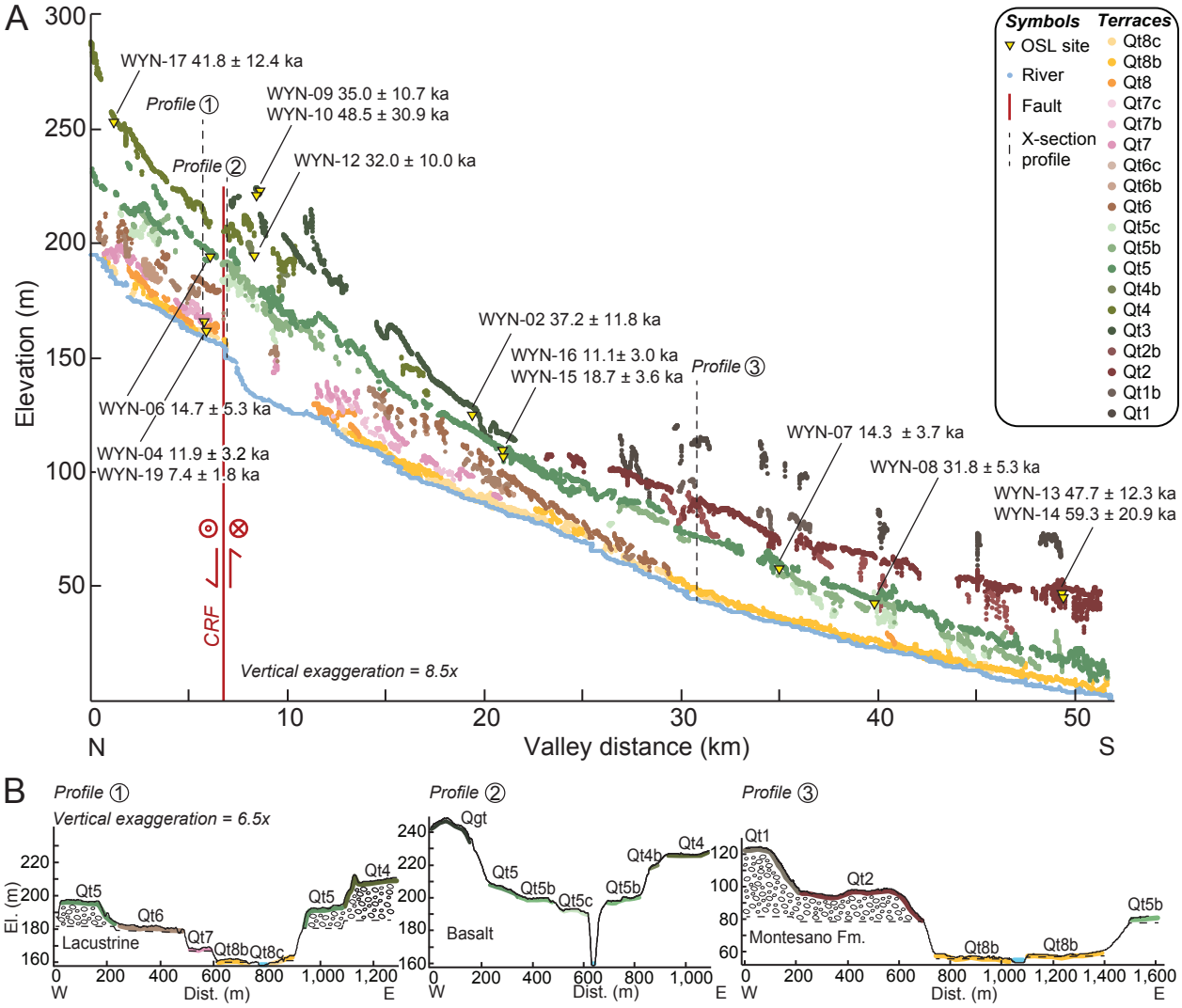

Figure 3. A) Valley profile of all Wynoochee River fluvial and outwash terrace treads, colored by unit, with OSL sample locations. CRF = Canyon River fault. B) Cross-valley profiles with locations shown in A, treads colored by unit. Dashed lines are strath heights from field surveys, profile 2 straths are very close to the tread.

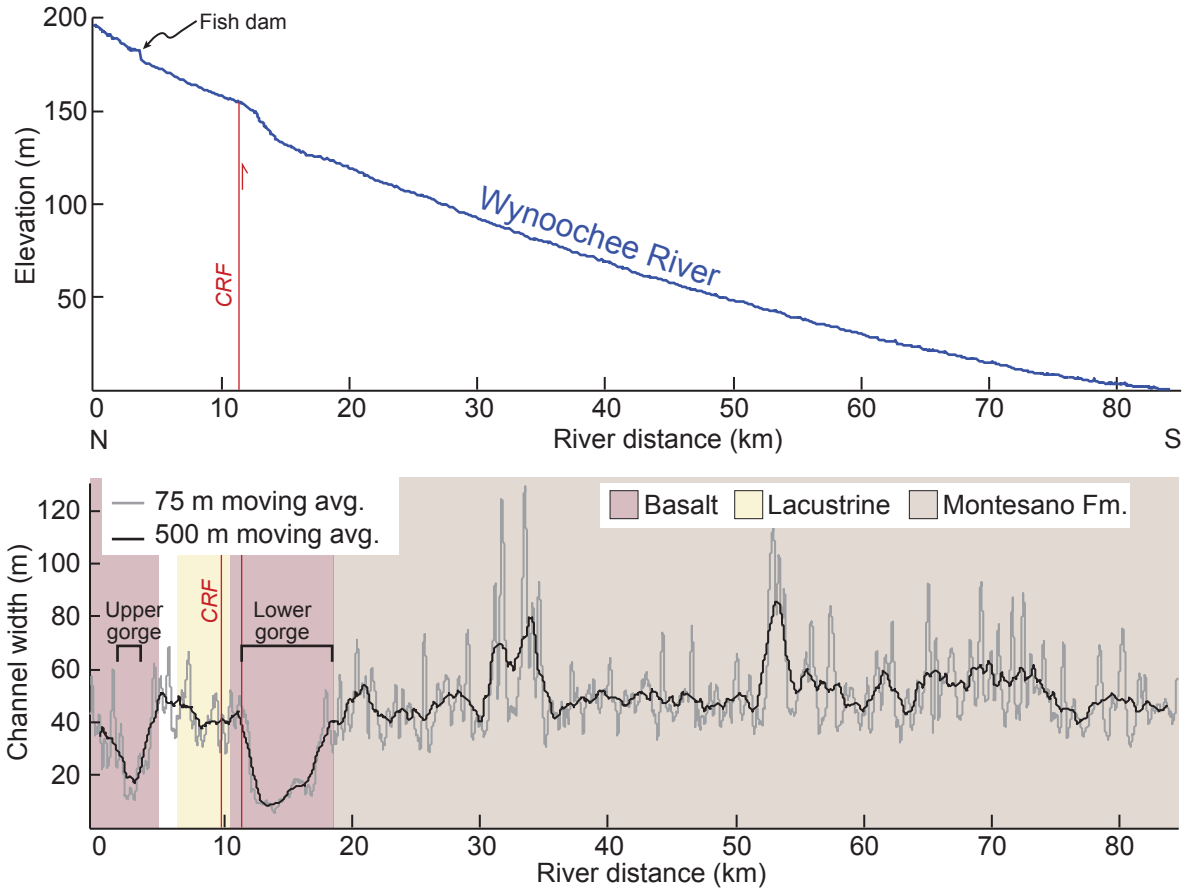

Figure 4. Top: Long profile of the Wynoochee River. Note the prominent knickpoint at ~7 km distance. Bottom: Channel width along the channel profile, showing channel substrate rock type. The two CRF (Canyon River fault) lines are the mapped traces that intersect the river.

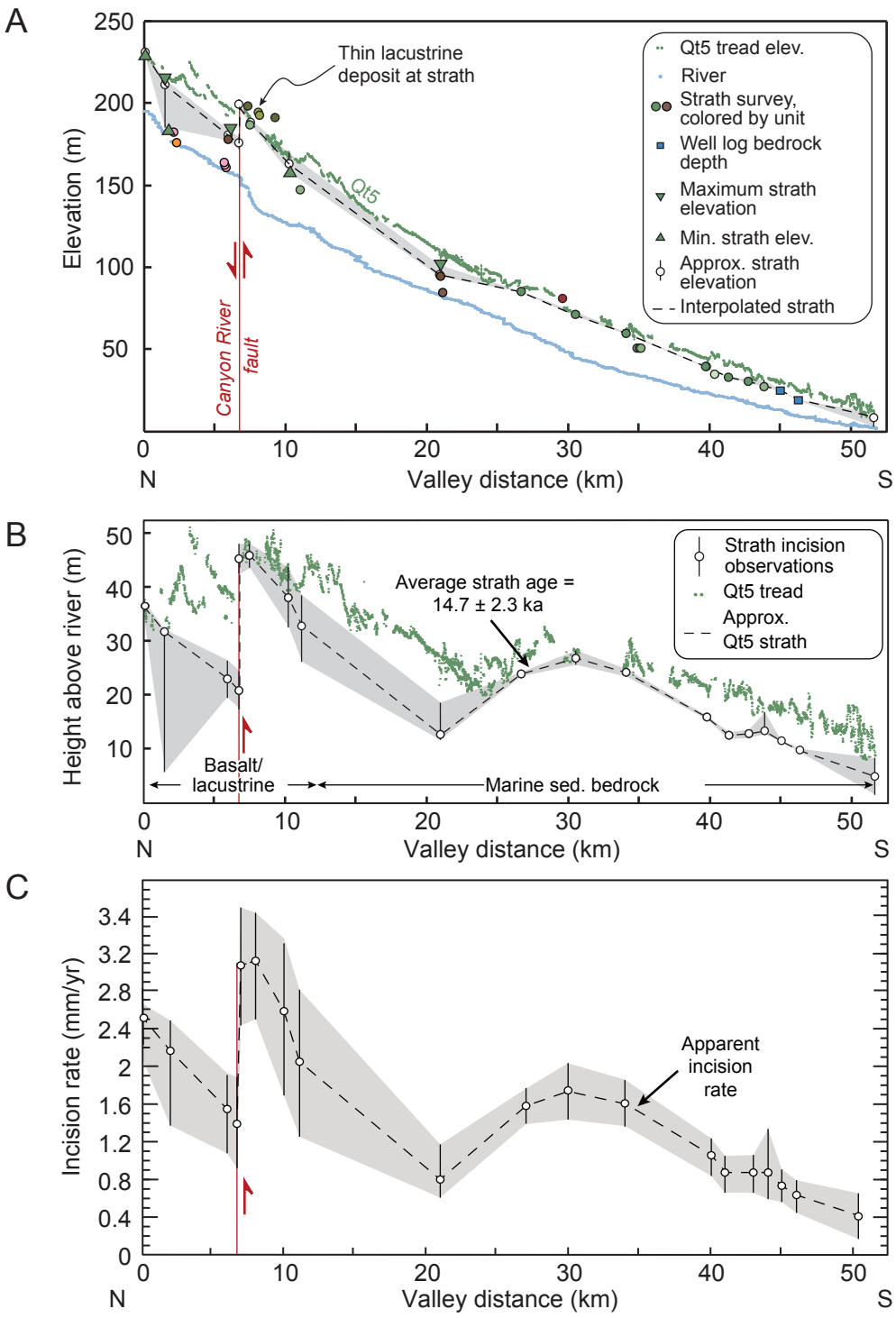

Figure 5. A) Qt5 tread and strath observation elevations vs. valley distance. Shading represents observation uncertainty. B) Strath height with uncertainty (shading) and tread height above the modern channel. C) Estimated incision rates with uncertainty (shading) from the Qt5 terrace.

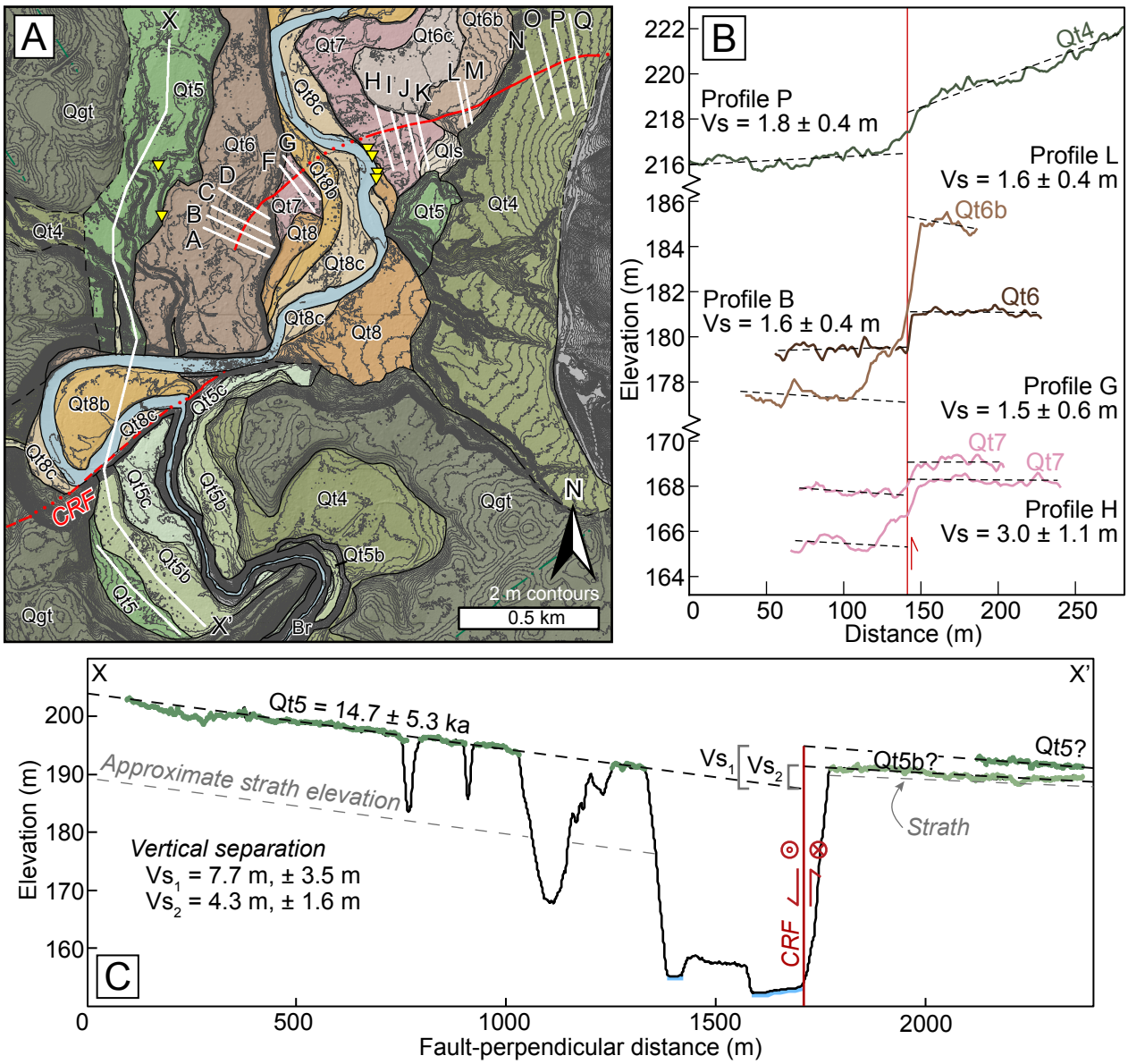

Figure 6. A) Location of scarp profiles shown in B and C with 2 m contours. CRF = Canyon River fault B) Select scarp profiles, colored by unit. Note the changes in elevation at 170 m and 186 m. Vs = vertical separation. C) Long profile of X - X'. Profile elevation points were projected to a line perpendicular to the fault strike. Black dashed lines are best-fit lines to tread surfaces, and gray dashed lines are the approximate strath height. Question marks on downstream terraces reflect uncertainty in matching terraces across the fault.

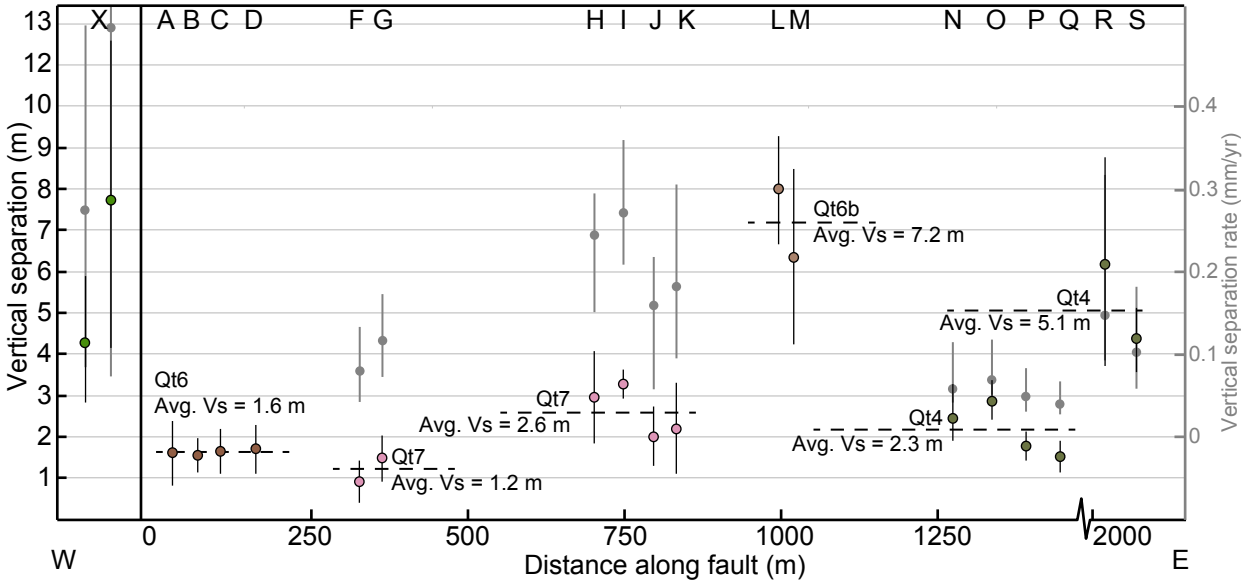

Figure 7. Vertical separation (Vs) is shown by colored points (colored by unit) along the Canyon River fault. Locations of each profile shown in Fig. 4A. Black dashed lines represent averages for each terrace; grey points show uplift rates using OSL ages. Vsr = Vertical separation rate.

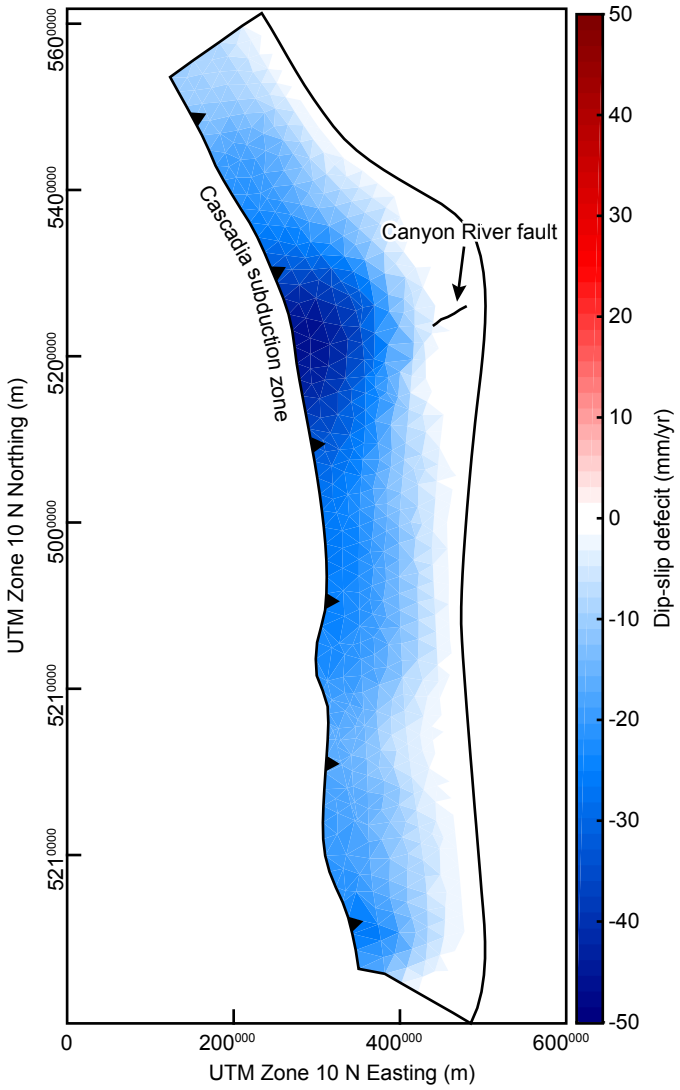

Figure 8. Dip-slip deficit distribution on the Cascadia subduction zone slab interface, constrained by GPS. Barbs on subduction zone point down dip.

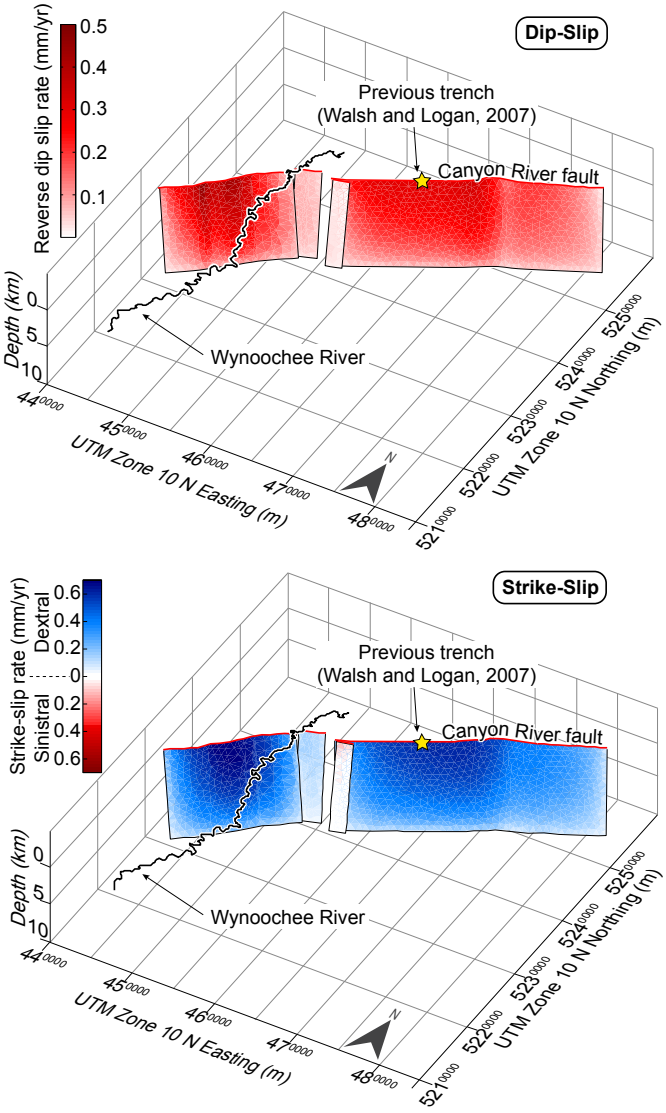

Figure 9. Dip slip and strike-slip rate results on the Canyon River fault from the boundary element model using 70° dip, projected to 10 km depth.

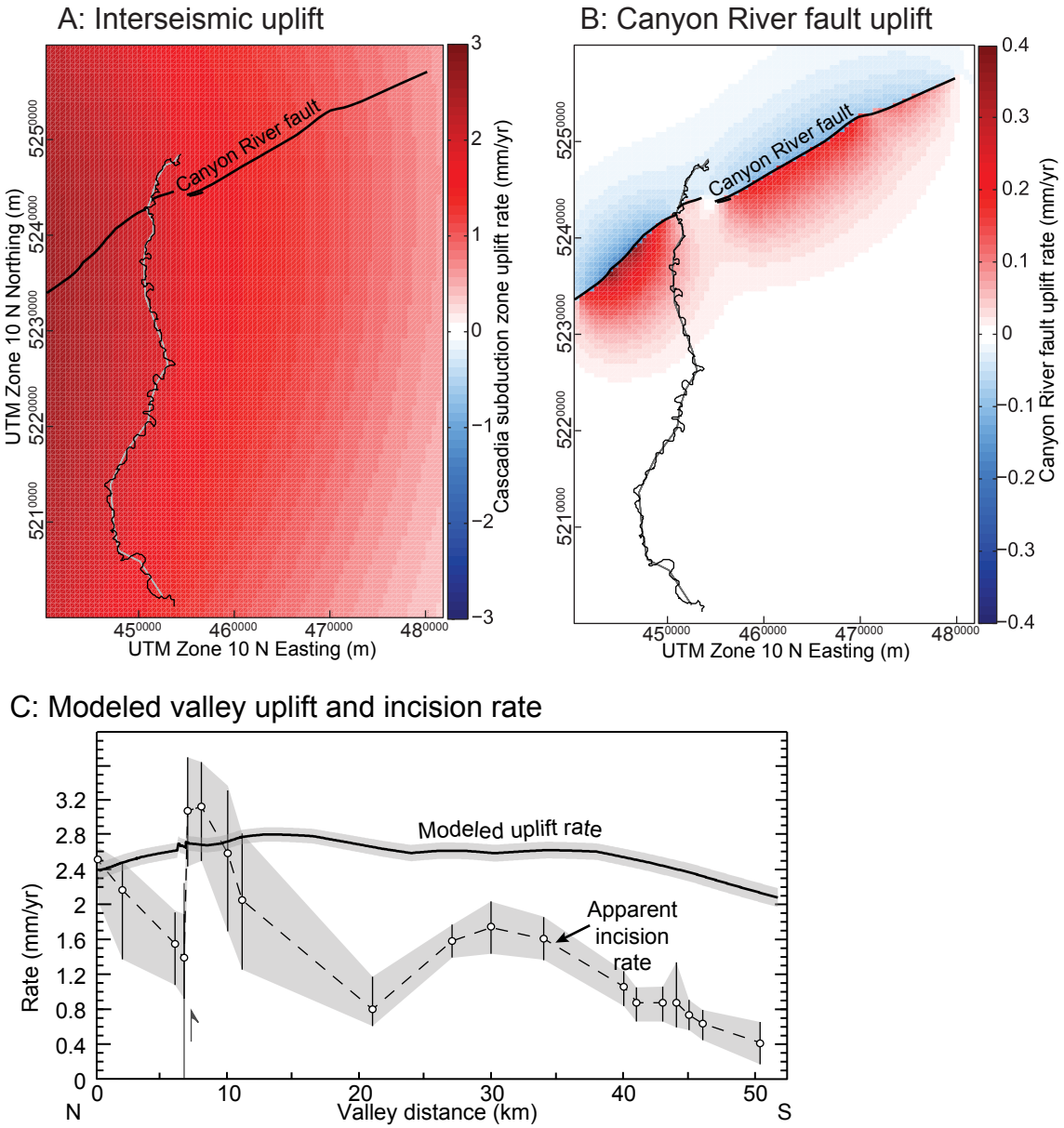

Figure 10. A) Regional uplift pattern of interseismic coupling on the Cascadia subduction zone, without slip on the Canyon River fault. B) Regional uplift rate pattern of BEM-predicted the slip on the Canyon river fault, using 70° dip and 10 km fault depth. C) Combined valley uplift pattern from the interseismic uplift of the Cascadia subduction zone and Canyon River fault projected to the valley line, compared to flivial incision rate from Fig. 5.

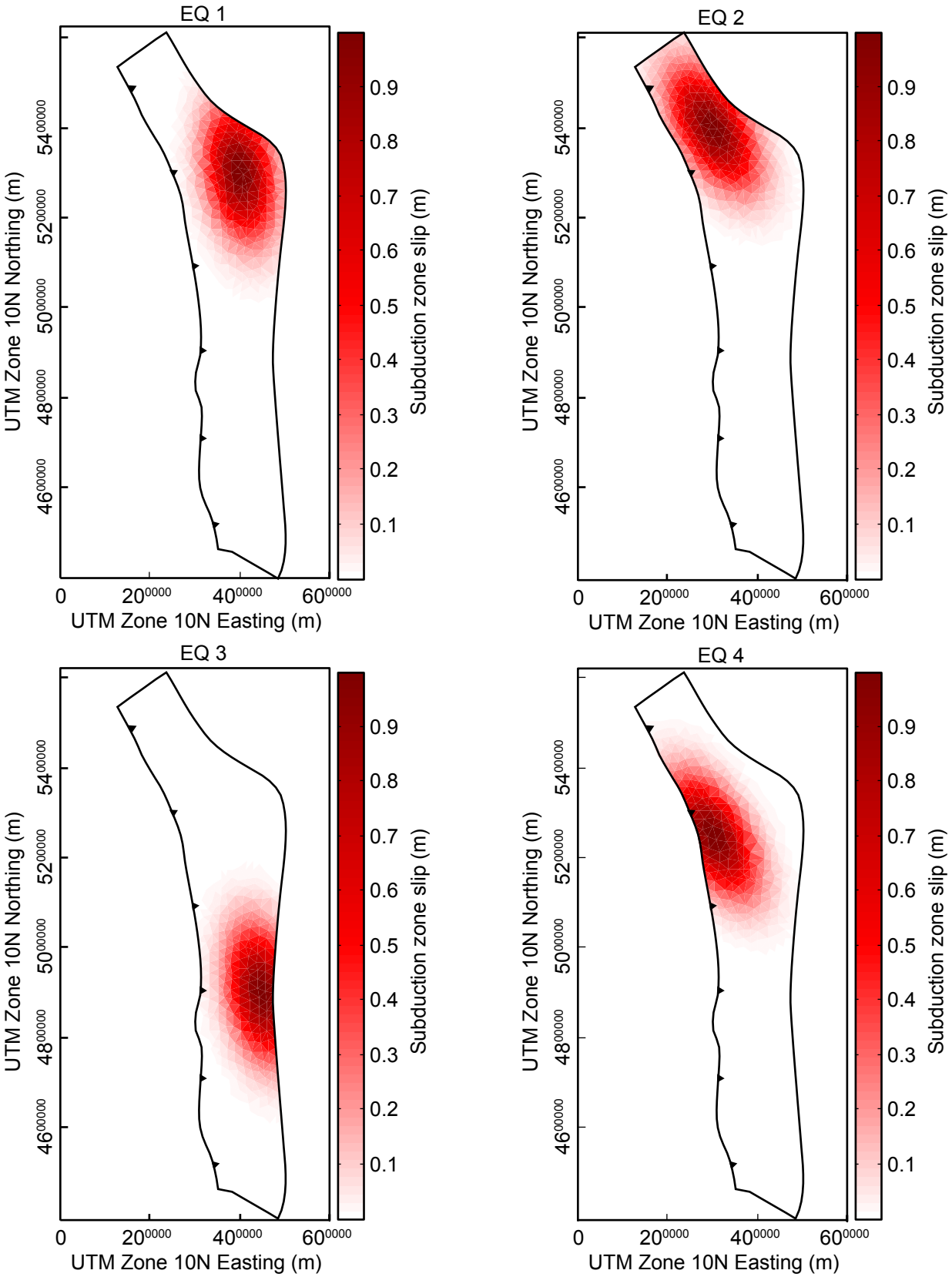

Figure 11. Synthetic earthquake dip-slip on the Cascadia subduction zone interface with 1 m peak slip. Resulting slip configurations on the Canyon River fault shown in Figure 12.

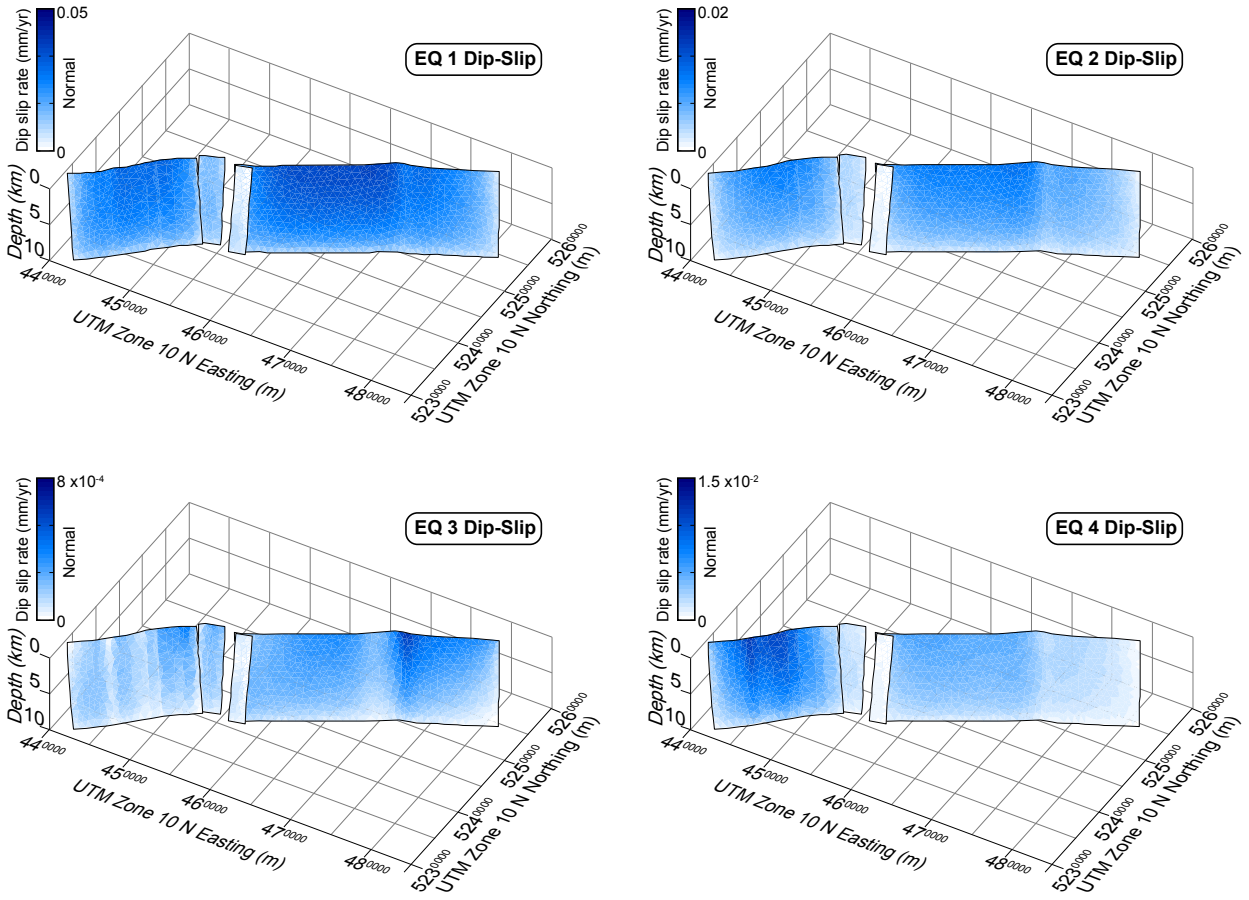

Figure 12. Slip on the Canyon River fault resulting from synthetic earthquake slip on the Cascadia subduction zone interface. Cascadia subduction slip configurations shown in Figure 11.

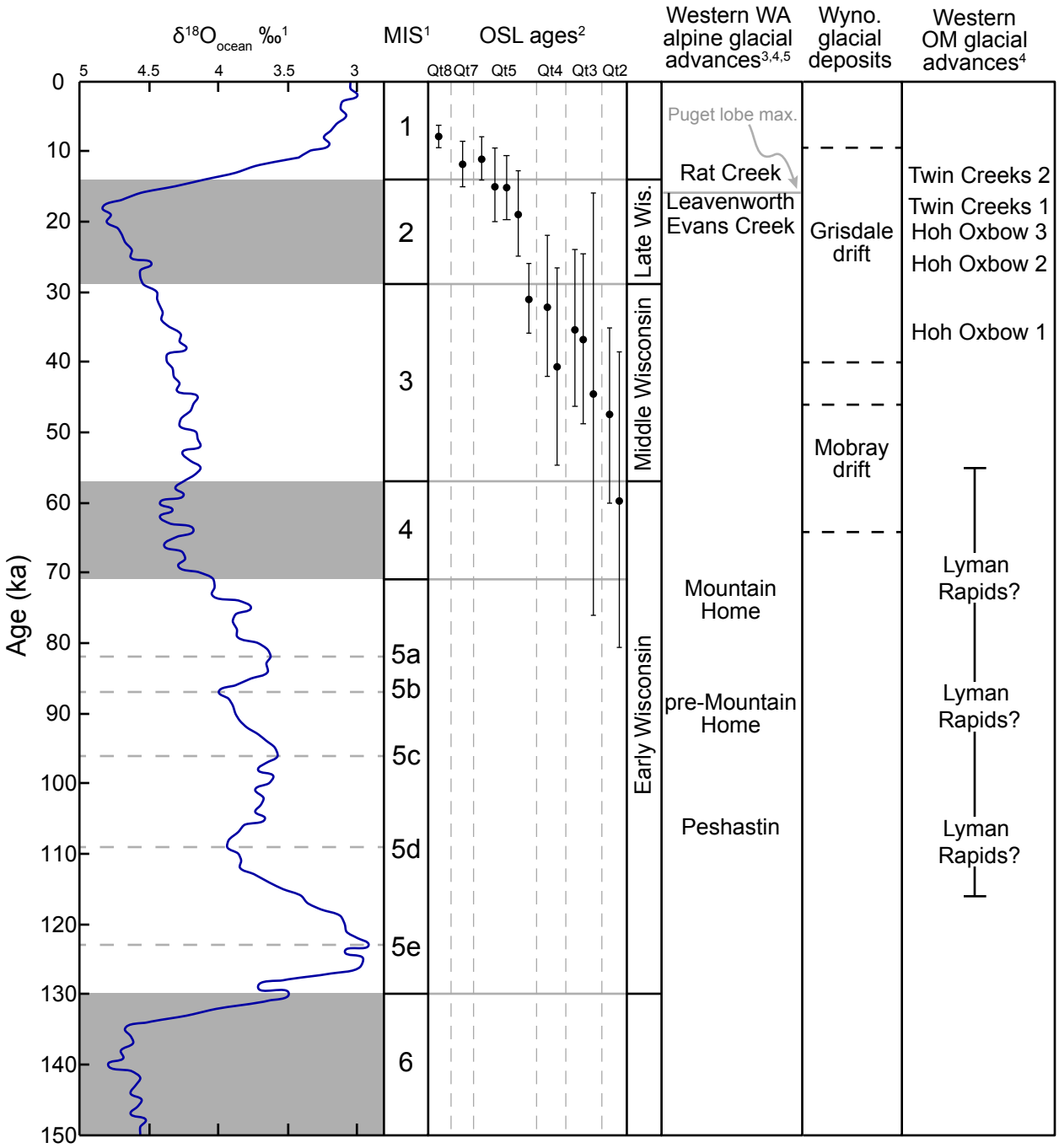

[1]Oxygen isotope and MIS stages from Lisiecki and Raymo (2005)
[2]OSL (optically stimulated luminescence) of Wynoochee River deposit ages from this study
[3]Puget Lobe and Evans Creek ages as compiled from Booth et al. (2003)
[4]Western Olympic Mountain glacial advances are from Thackray (2001)
[5]Western Washington alpine glaciations as compiled from Kaufman et al. (2004)

Figure 13. Terrace chronology from this study compared to other global climate events and glacial advances in other Olympic Mountain drainages. Red OSL sample age is likely over estimated. The three Lyman Rapids advances and error bars reflects deposit age uncertainty. MIS = marine isotope stage, OM = Olympic Mountains, OSL = optically stimulated luminescence, Wyno. = Wynoochee

Figure 14. 1) River incises into bedrock during an interglacial period. 2) Glacier advances to maximum, over-running the lower gorge and deposits outwash. 3) The glacier retreats and continues to deposit outwash. Ice and debris dam the river and fill the lower gorge with lake deposits. 4) Between glacial advances, the dam breaches and the river incises into outwash and lake deposits, leaving lacustrine deposits on existing basalt straths. GIA steepens Qt3 surface. 5) An upstream glacial advance causes aggradation on top of the lacustrine strath in the lower gorge and upstream. 6) During the modern interglacial period, the river re-excavates the lower gorge leaving lacustrine and outwash deposits at high elevations.

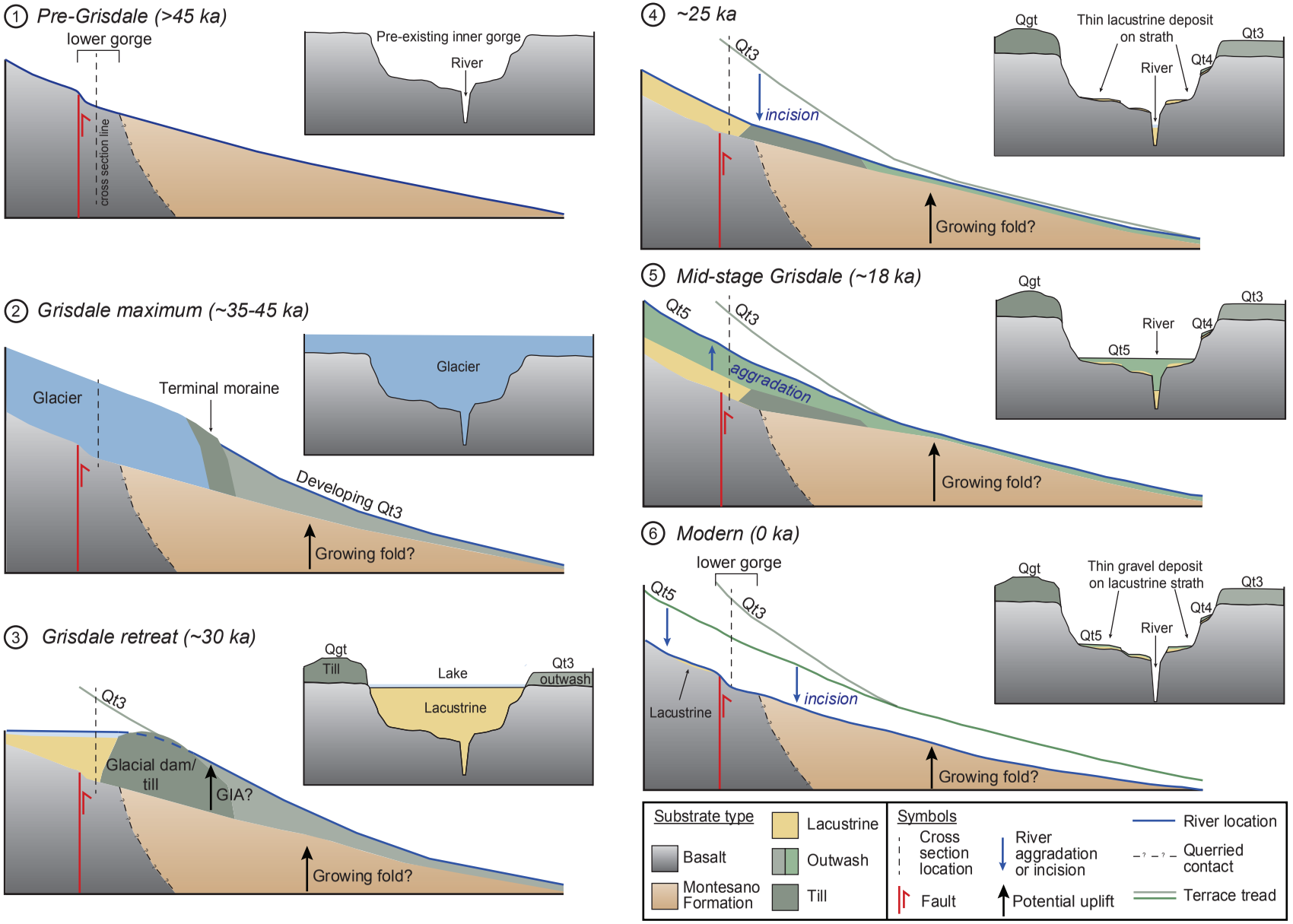

Figure 14. See caption on previous page

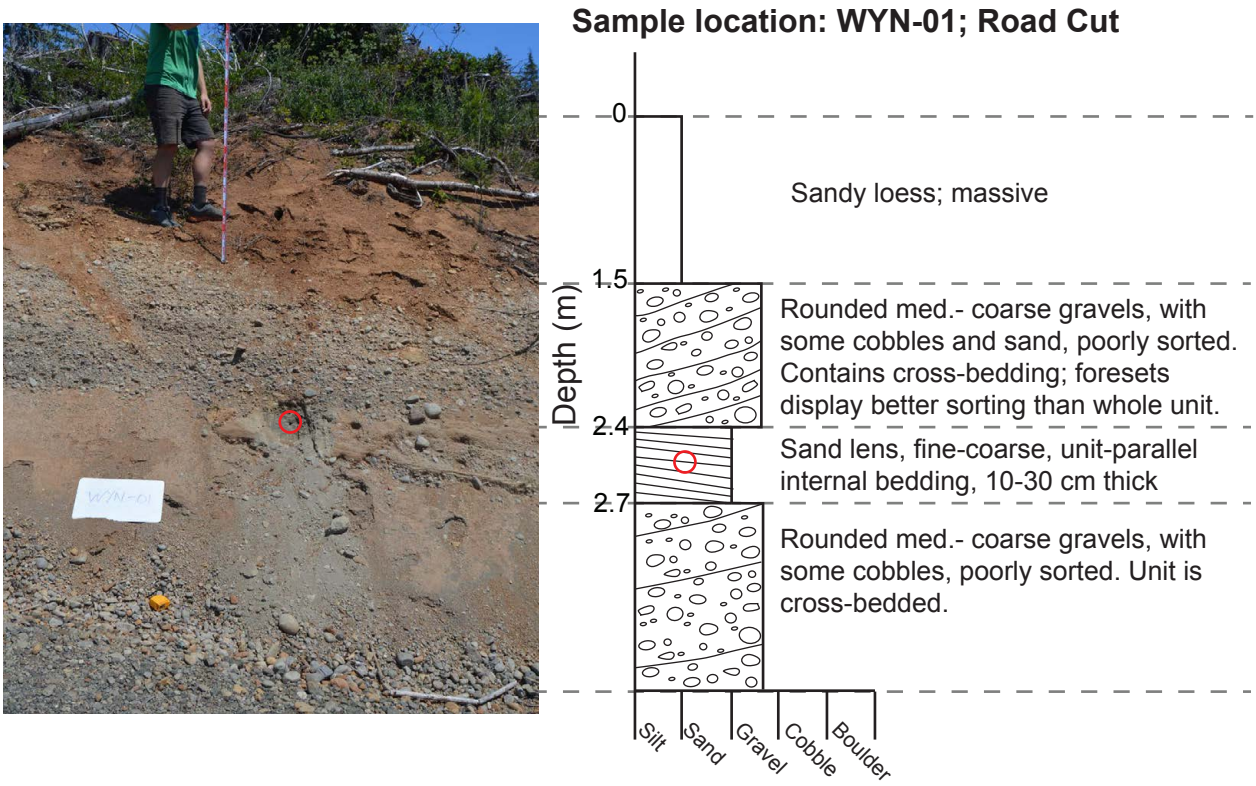

Figure S1.

Caption for figures S1-S22: Stratigraphic columns for optically stimulated luminescence sample sites.

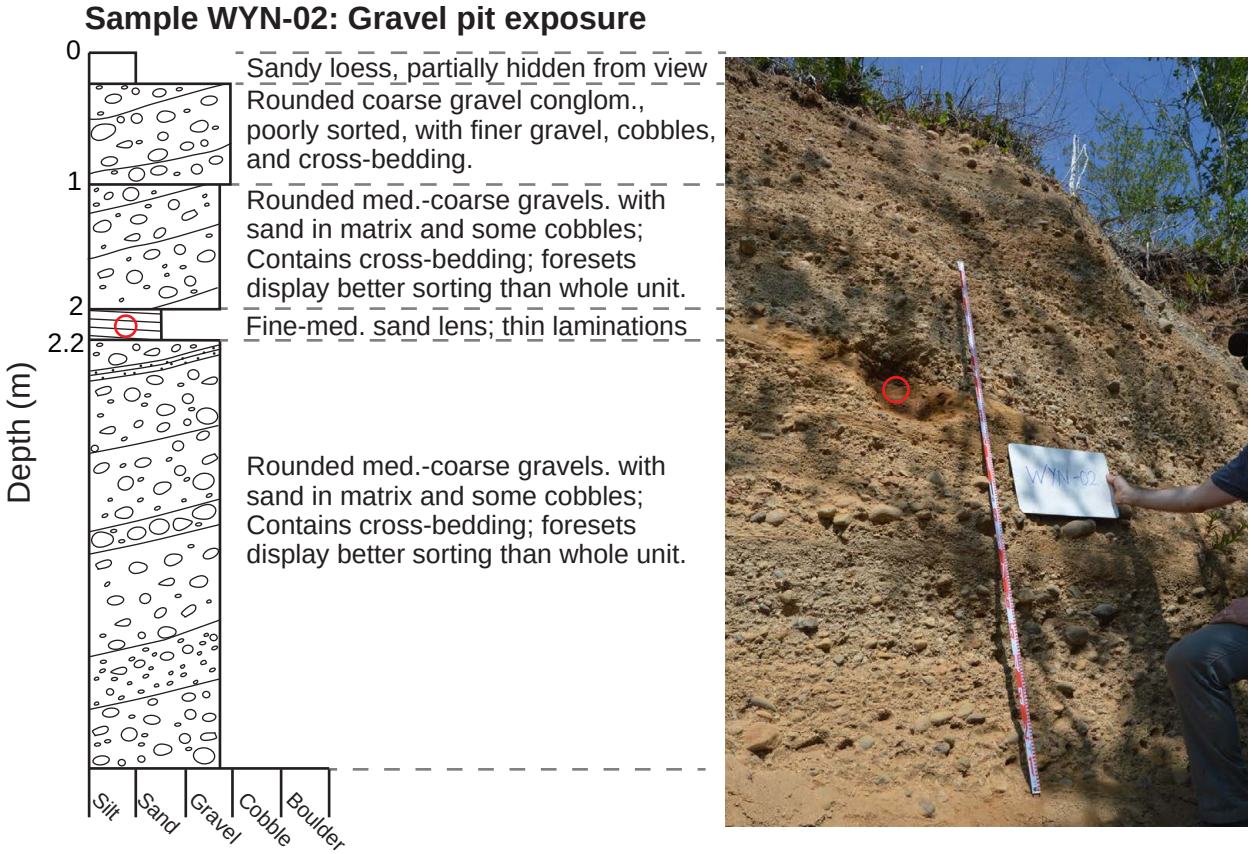
Sample WYN-02: Gravel pit exposure
Depth (m)
0
1
2
2.2
Sandy loess, partially hidden from view
Rounded coarse gravel conglom., poorly sorted, with finer gravel, cobbles, and cross-bedding.
Rounded med.-coarse gravels. with sand in matrix and some cobbles; Contains cross-bedding; foresets display better sorting than whole unit.
Fine-med. sand lens; thin laminations
Rounded med.-coarse gravels. with sand in matrix and some cobbles; Contains cross-bedding; foresets display better sorting than whole unit.
Silt
Sand
Gravel
Cobble
Boulder
WYN-02

Figure S2.

Sample WYN-03: River cut, night collection into 1 gallon paint can

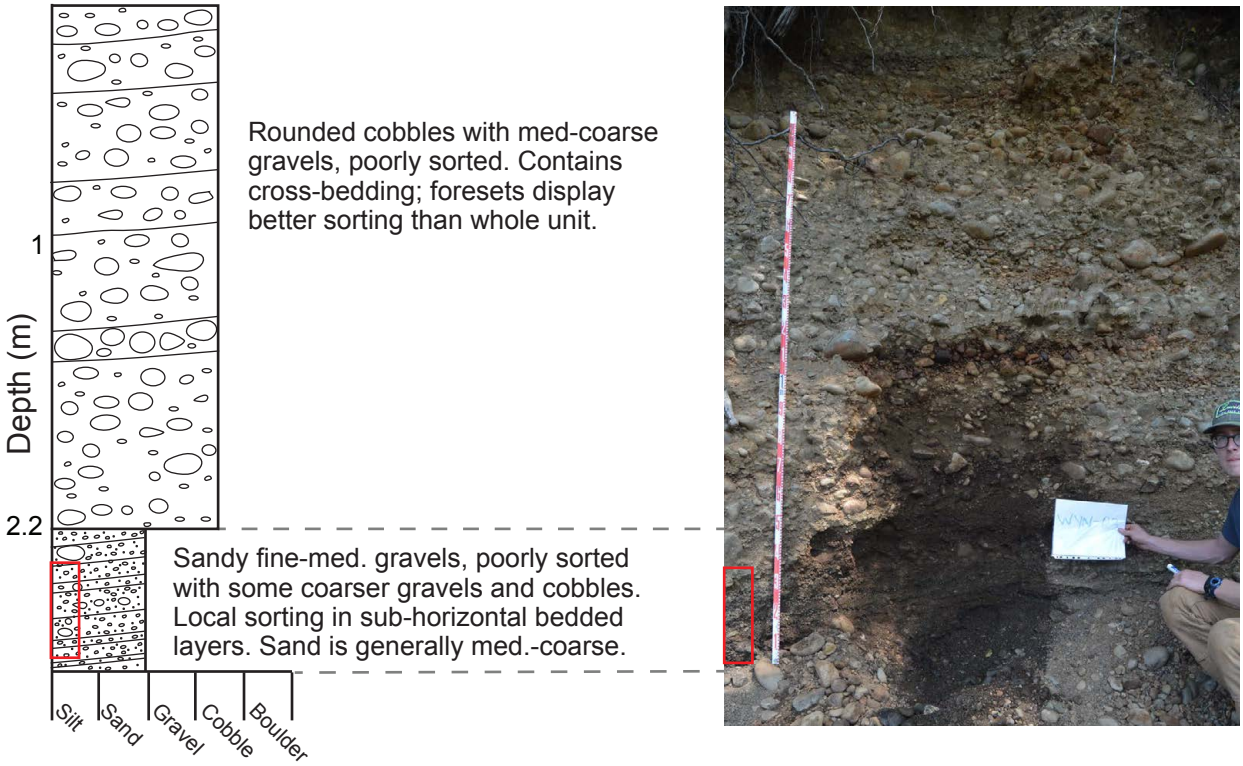

Figure S3.

Sample WYN-04 location: cut bank

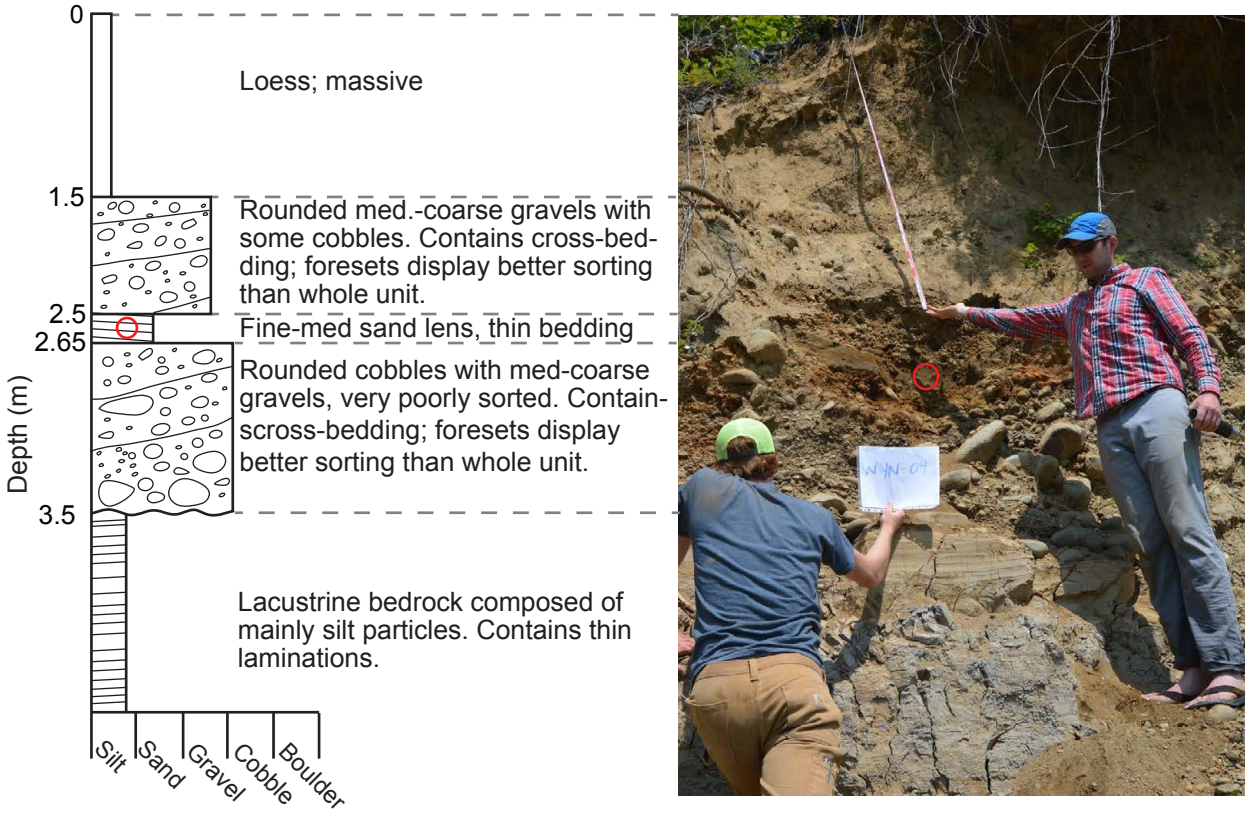

Figure S4.

Sample WYN-05 location: Road cut

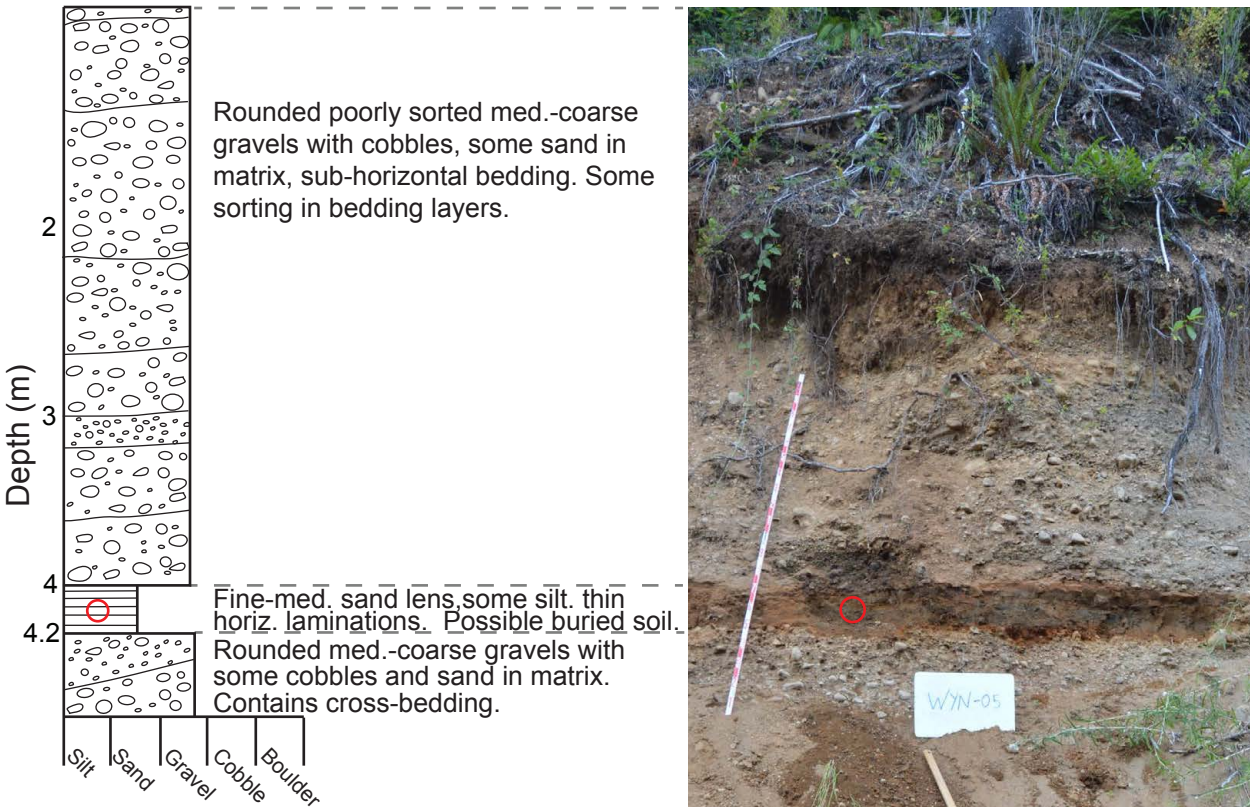

Figure S5.

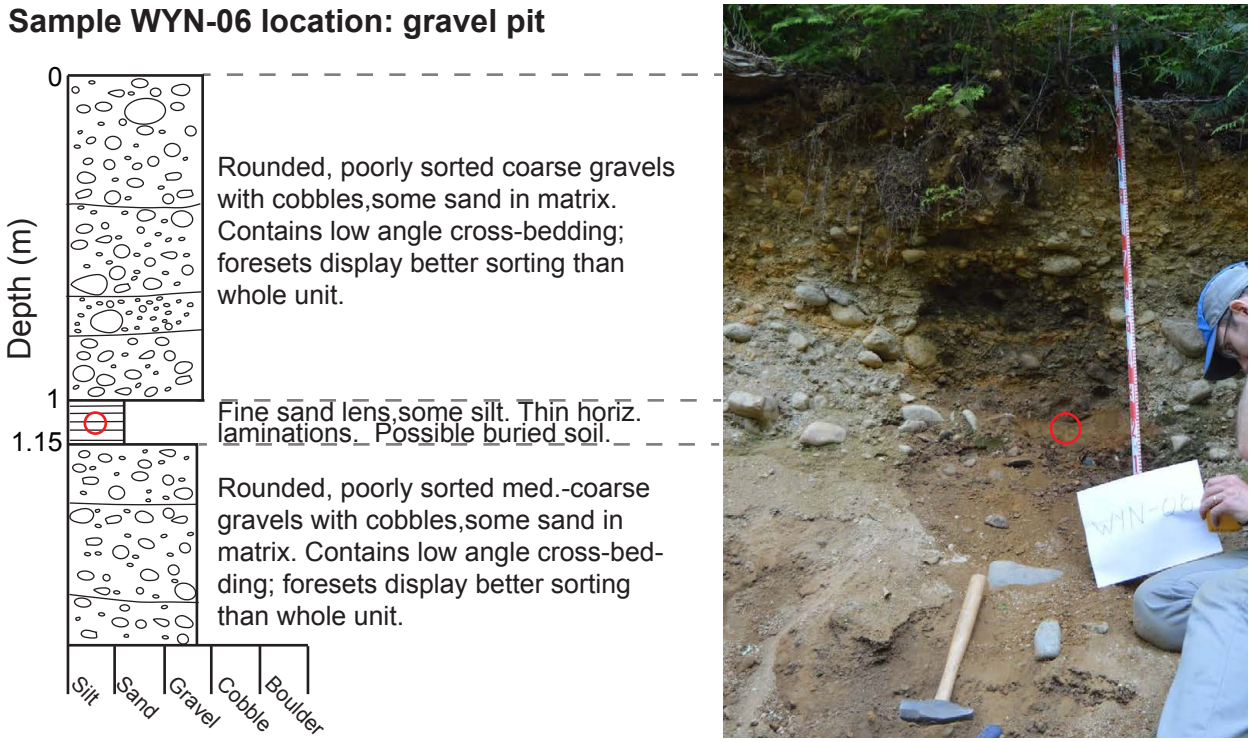
Sample WYN-06 location: gravel pit
Depth (m)
0
1
1.15
Rounded, poorly sorted coarse gravels with cobbles,some sand in matrix. Contains low angle cross-bedding; foresets display better sorting than whole unit.
Fine sand lens,some silt. Thin horiz. laminations. Possible buried soil.
Rounded, poorly sorted med.-coarse gravels with cobbles,some sand in matrix. Contains low angle cross-bedding; foresets display better sorting than whole unit.
Silt
Sand
Gravel
Cobble
Boulder
WYN-06

Figure S6.

Sample WYN-07 location: Exposed cliff adjacent to road (old river cutbank)

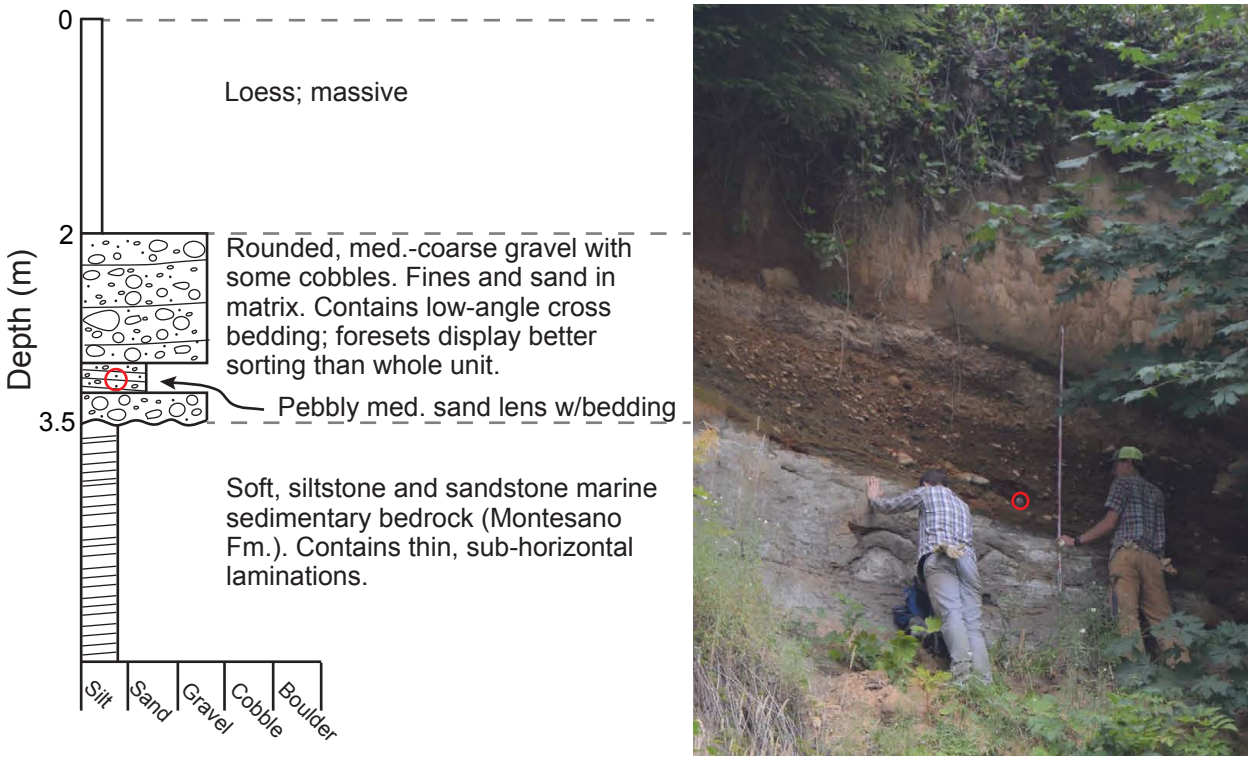

Figure S7.

Sample WYN-08 location: cut bank adjacent to road

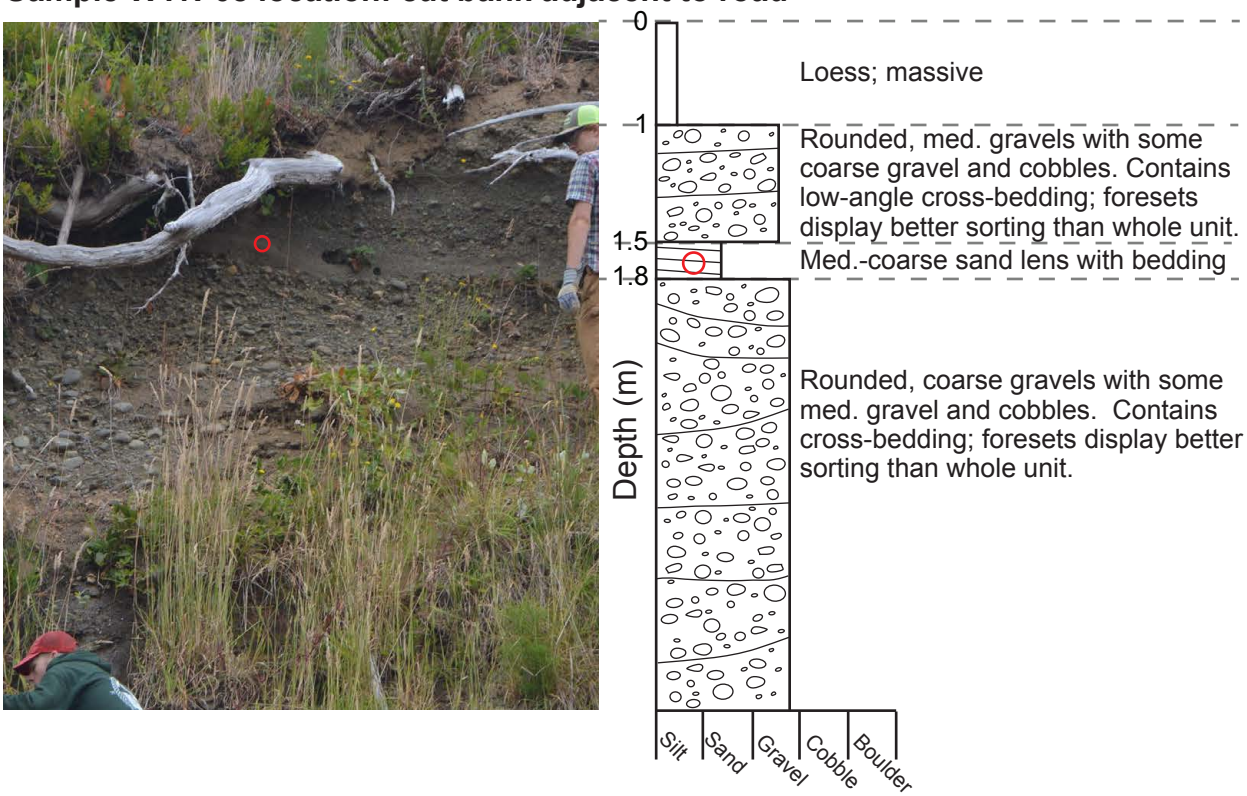

Figure S8.

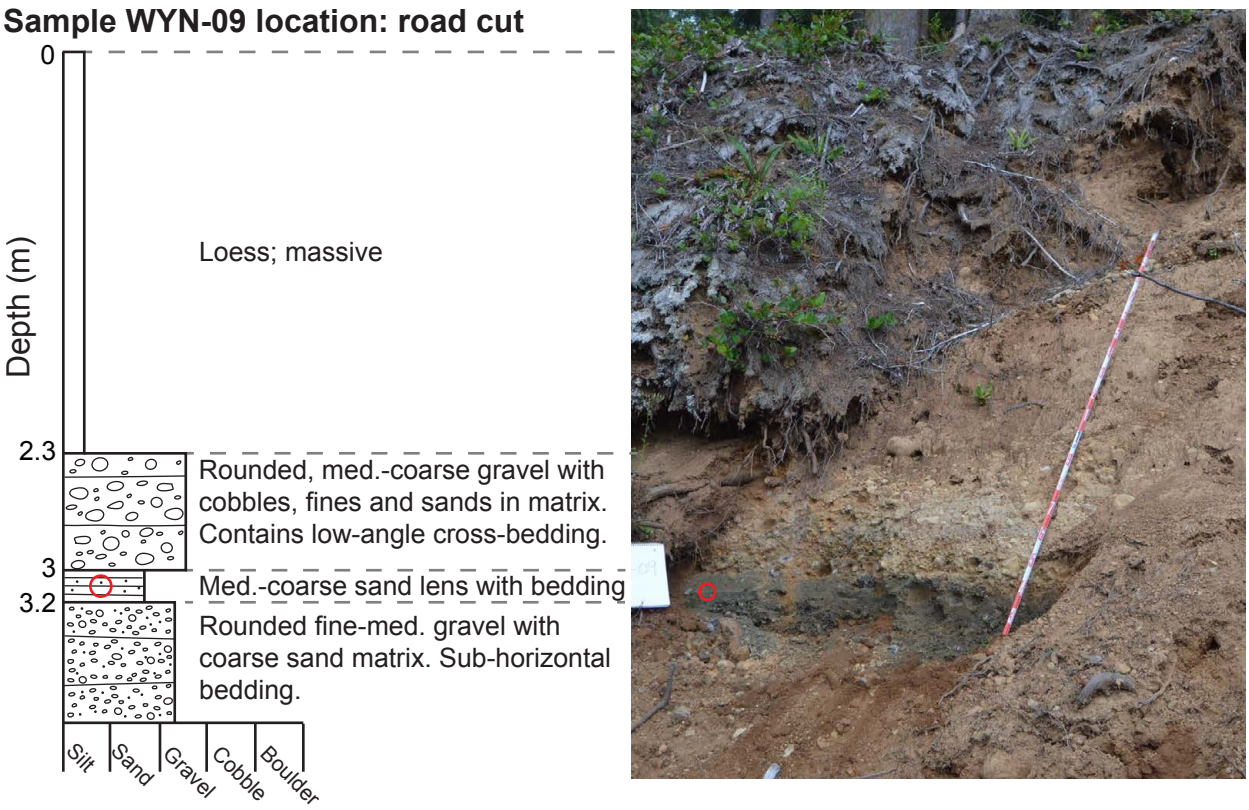
Sample WYN-09 location: road cut
Depth (m)
0
2.3
3
3.2
Loess; massive
Rounded, med.-coarse gravel with cobbles, fines and sands in matrix. Contains low-angle cross-bedding.
Med.-coarse sand lens with bedding
Rounded fine-med. gravel with coarse sand matrix. Sub-horizontal bedding.
Silt
Sand
Gravel
Cobble
Boulder

Figure S9.

Sample WYN-10 location: road cut

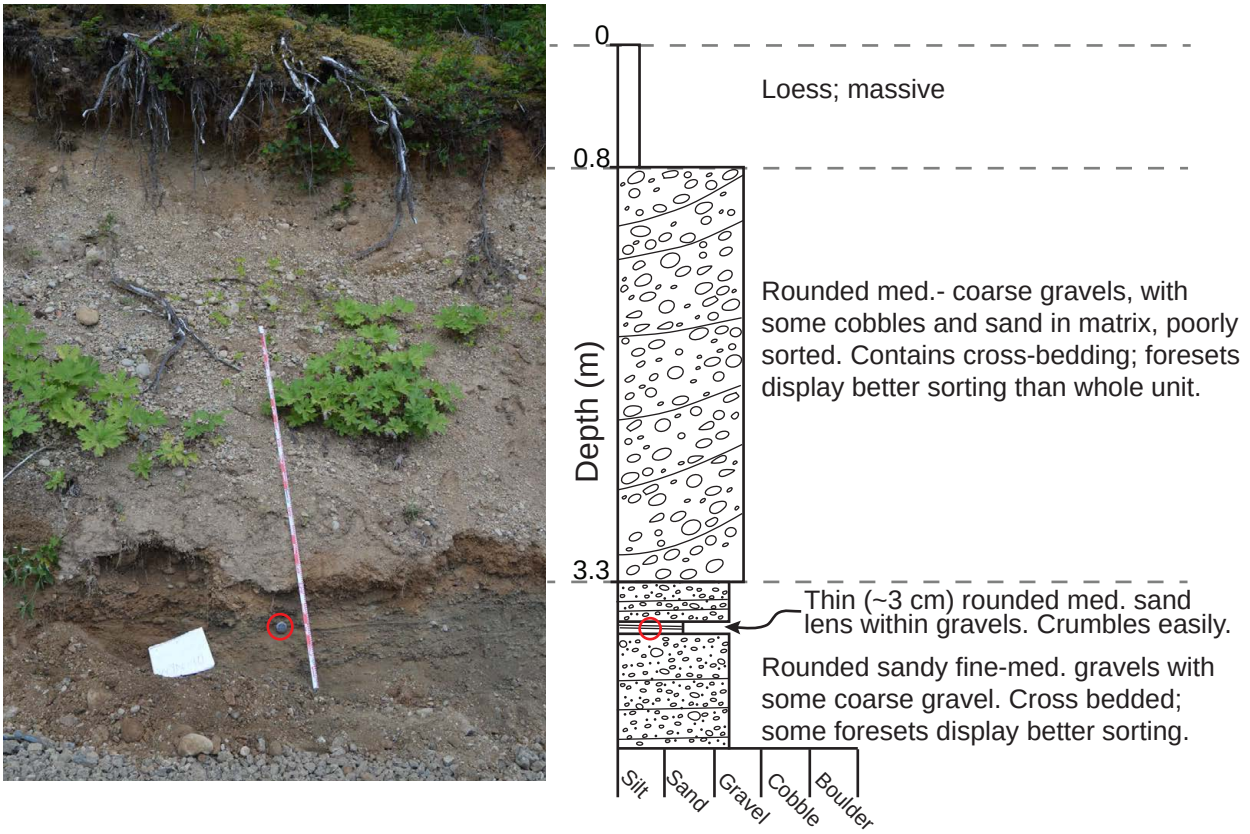

Figure S10.

Sample WYN-11 location: edge of cliff (canyon) adjacent to river

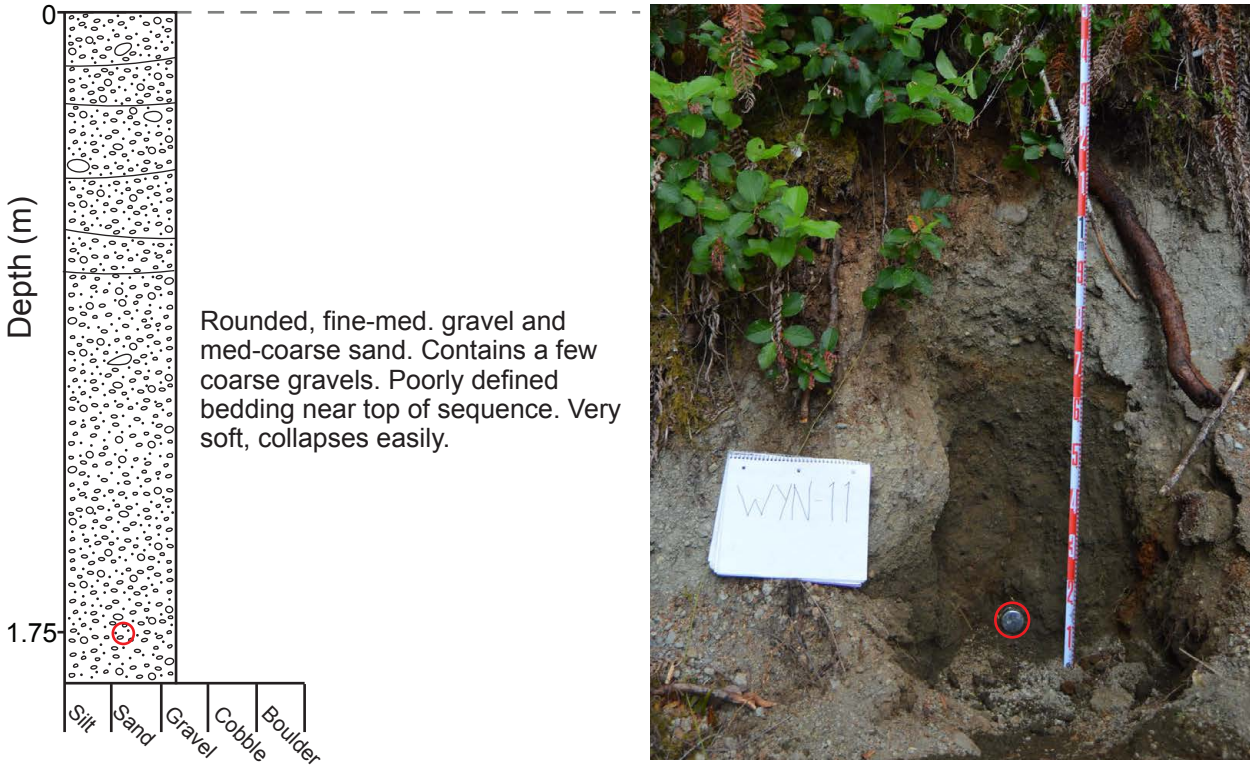

Figure S11.

Sample WYN-12 location: edge of cliff adjacent to river

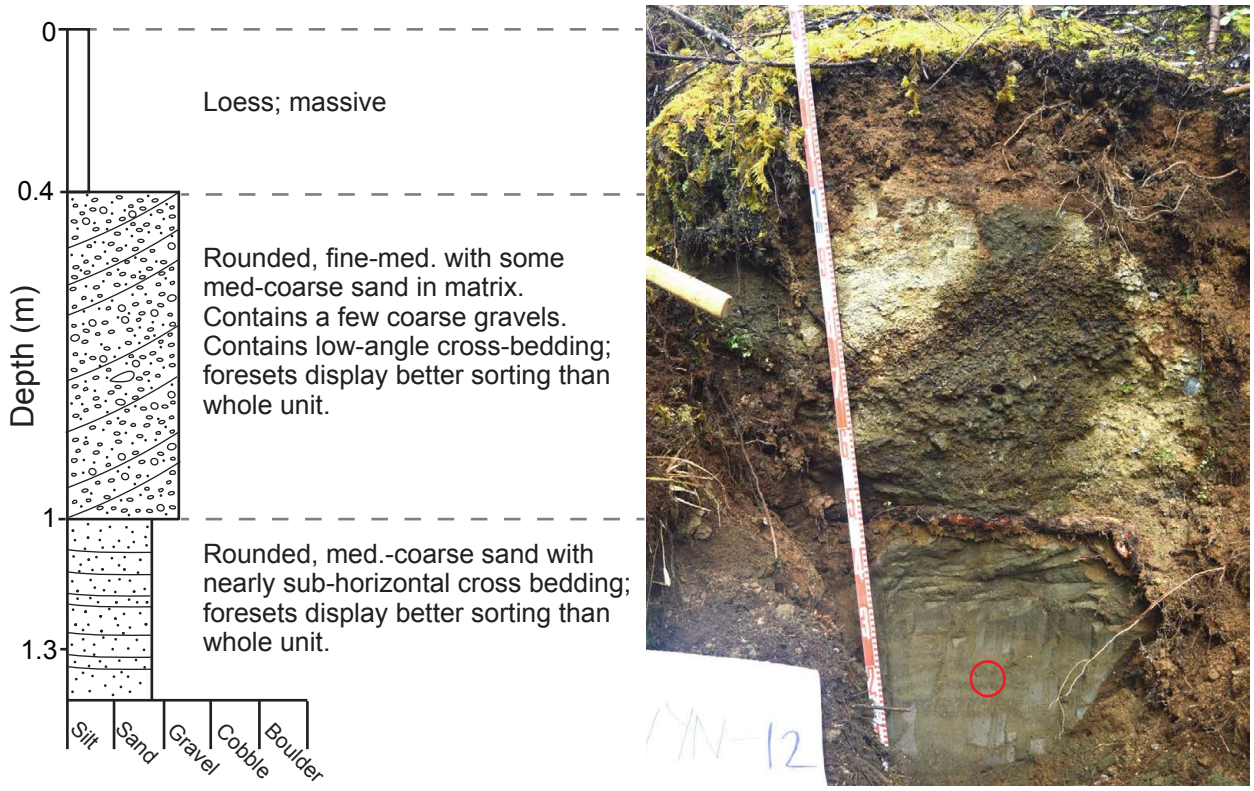

Figure S12.

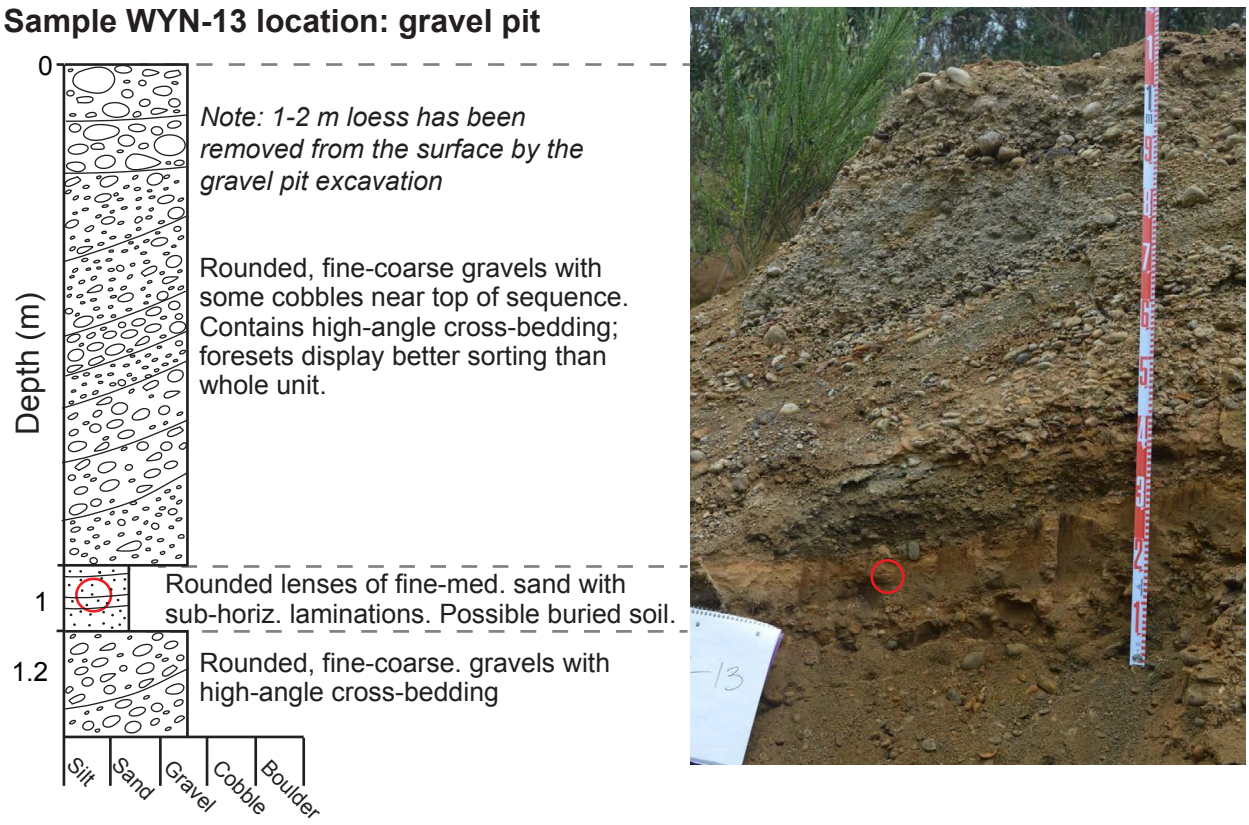
Sample WYN-13 location: gravel pit
0
Depth (m)
Note: 1-2 m loess has been removed from the surface by the gravel pit excavation
Rounded, fine-coarse gravels with some cobbles near top of sequence. Contains high-angle cross-bedding; foresets display better sorting than whole unit.
1
Rounded lenses of fine-med. sand with sub-horiz. laminations. Possible buried soil.
1.2
Rounded, fine-coarse. gravels with high-angle cross-bedding
Silt
Sand
Gravel
Cobble
Boulder

Figure S13.

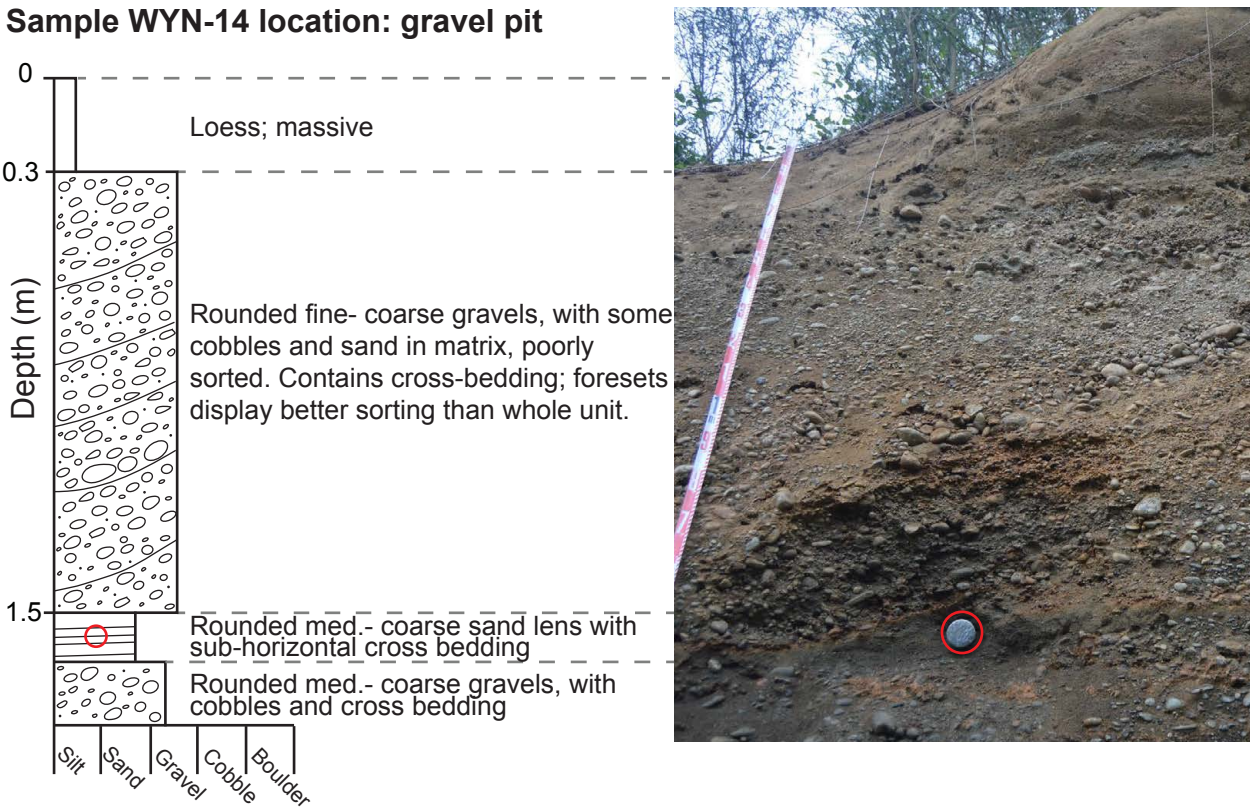
Sample WYN-14 location: gravel pit
0
0.3
1.5
Depth (m)
Loess; massive
Rounded fine- coarse gravels, with some cobbles and sand in matrix, poorly sorted. Contains cross-bedding; foresets display better sorting than whole unit.
Rounded med.- coarse sand lens with sub-horizontal cross bedding
Rounded med.- coarse gravels, with cobbles and cross bedding
Silt
Sand
Gravel
Cobble
Boulder

Figure S14.

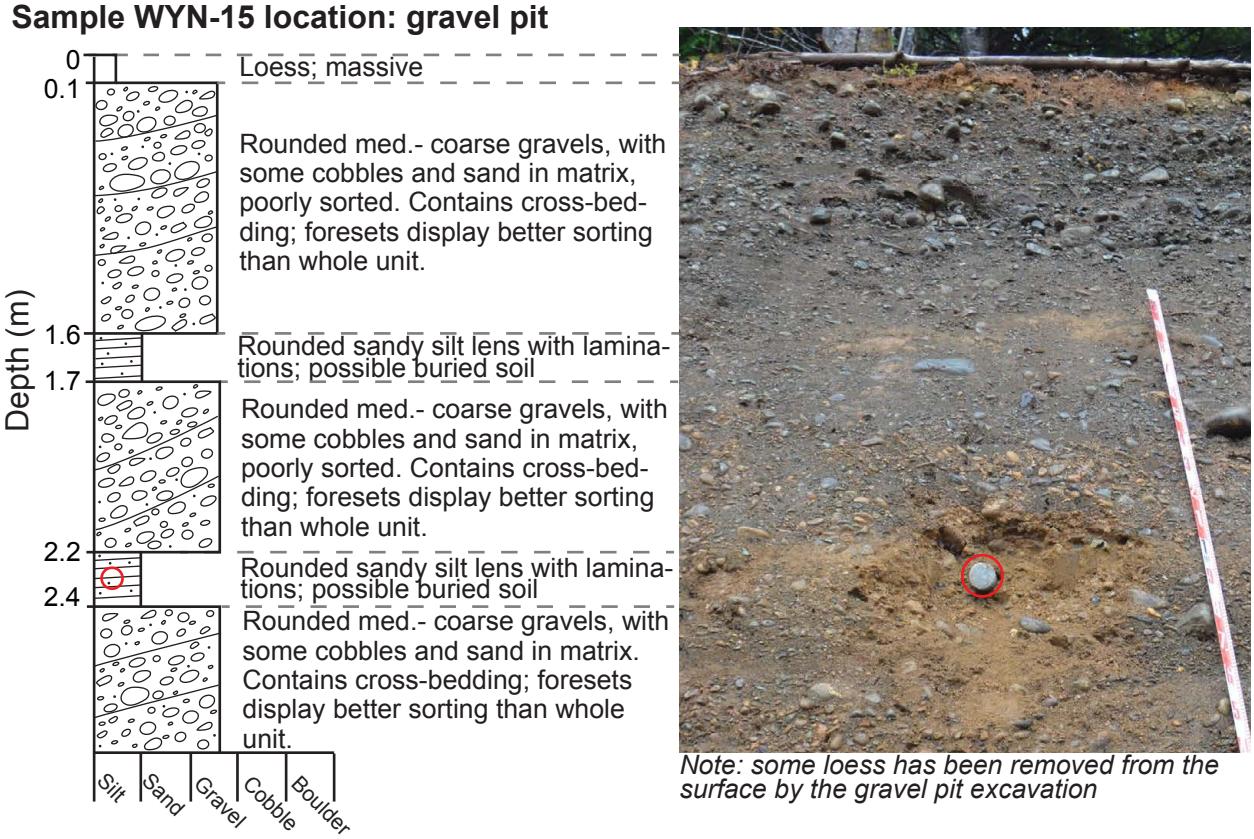
Sample WYN-15 location: gravel pit
Depth (m)
0
0.1
1.6
1.7
2.2
2.4
Loess; massive
Rounded med.- coarse gravels, with some cobbles and sand in matrix, poorly sorted. Contains cross-bedding; foresets display better sorting than whole unit.
Rounded sandy silt lens with laminations; possible buried soil
Rounded med.- coarse gravels, with some cobbles and sand in matrix, poorly sorted. Contains cross-bedding; foresets display better sorting than whole unit.
Rounded sandy silt lens with laminations; possible buried soil
Rounded med.- coarse gravels, with some cobbles and sand in matrix. Contains cross-bedding; foresets display better sorting than whole unit.
Silt
Sand
Gravel
Cobble
Boulder
Note: some loess has been removed from the surface by the gravel pit excavation

Figure S15.

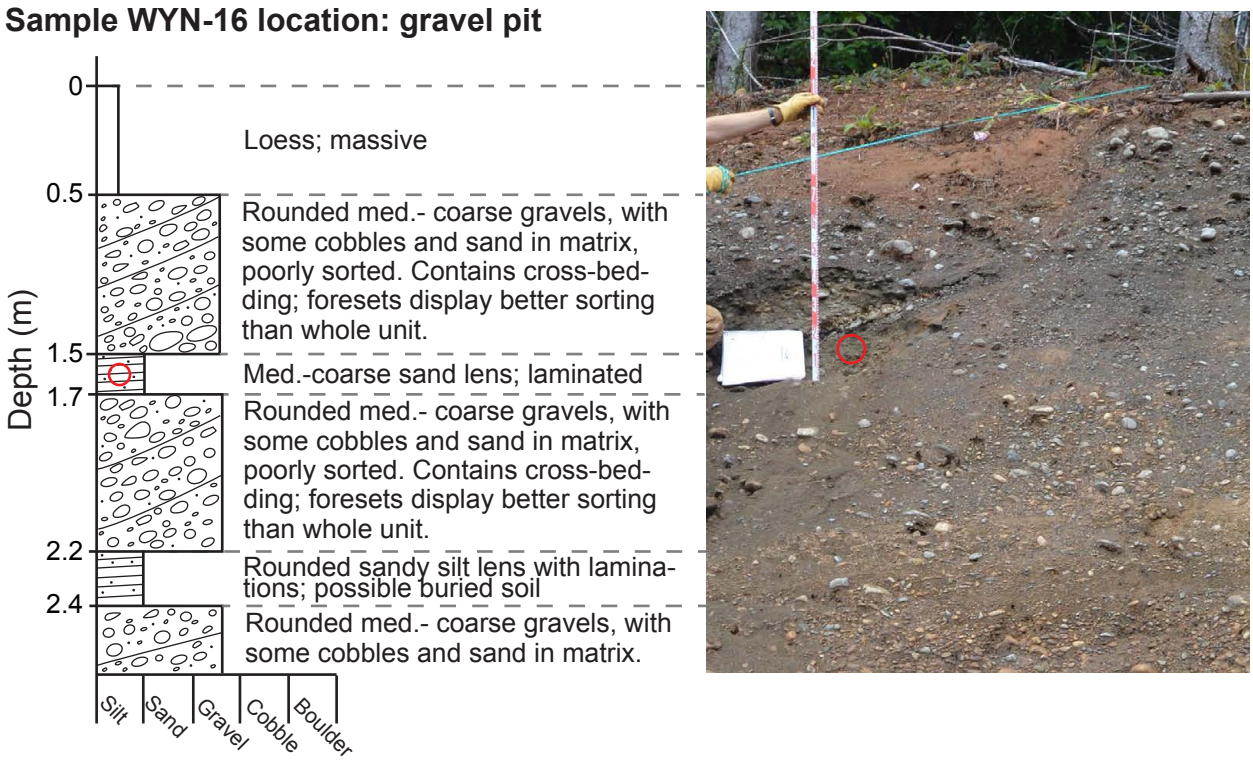
Sample WYN-16 location: gravel pit
Depth (m)
0
0.5
1.5
1.7
2.2
2.4
Loess; massive
Rounded med.- coarse gravels, with some cobbles and sand in matrix, poorly sorted. Contains cross-bedding; foresets display better sorting than whole unit.
Med.-coarse sand lens; laminated
Rounded med.- coarse gravels, with some cobbles and sand in matrix, poorly sorted. Contains cross-bedding; foresets display better sorting than whole unit.
Rounded sandy silt lens with laminations; possible buried soil
Rounded med.- coarse gravels, with some cobbles and sand in matrix.
Silt
Sand
Gravel
Cobble
Boulder

Figure S16.

Sample WYN-17 location: cliff; landslide-prone river cut

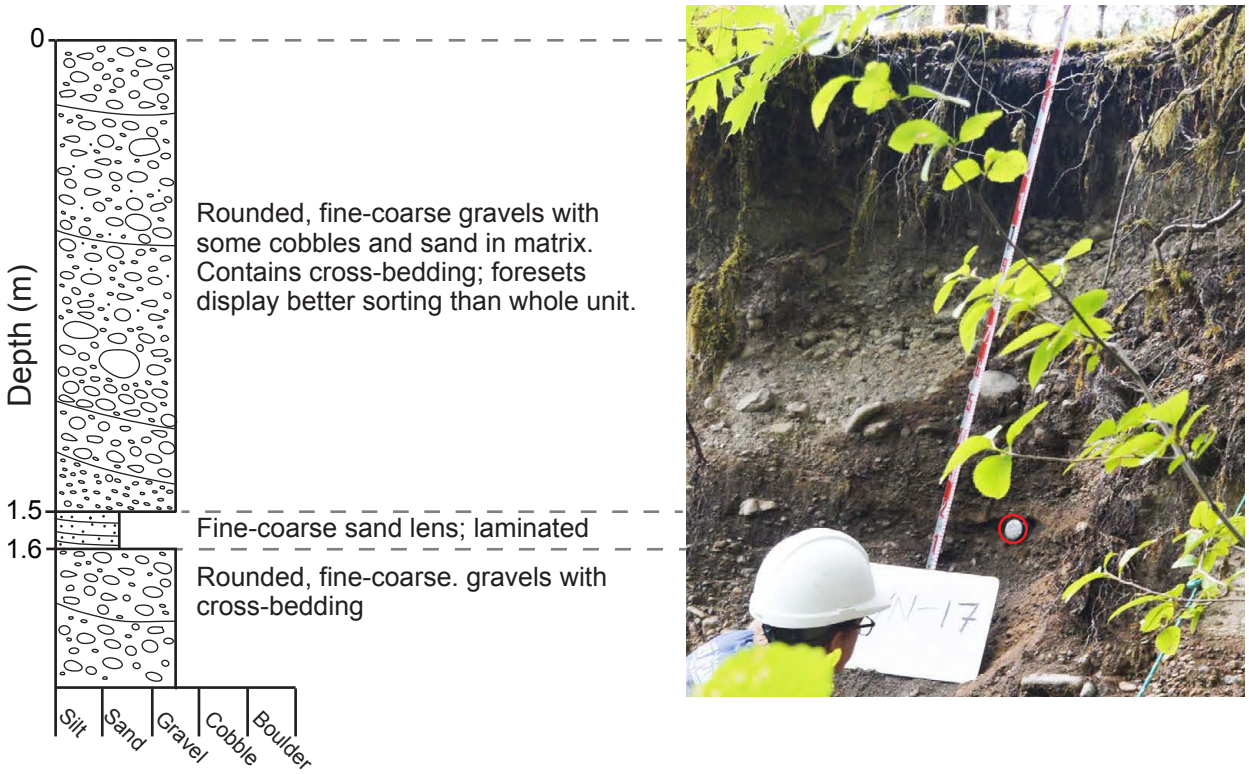

Figure S17.

Sample WYN-18 location: cliff; landslide-prone river cut

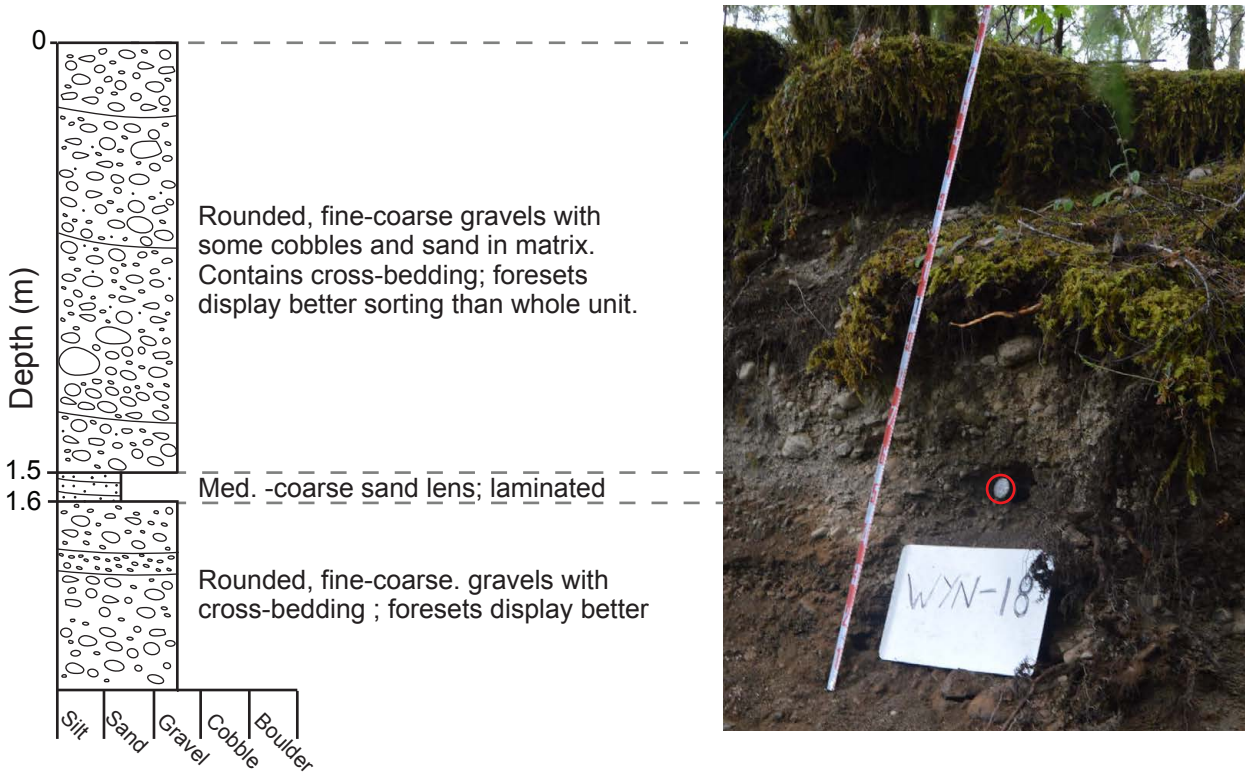

Figure S18.

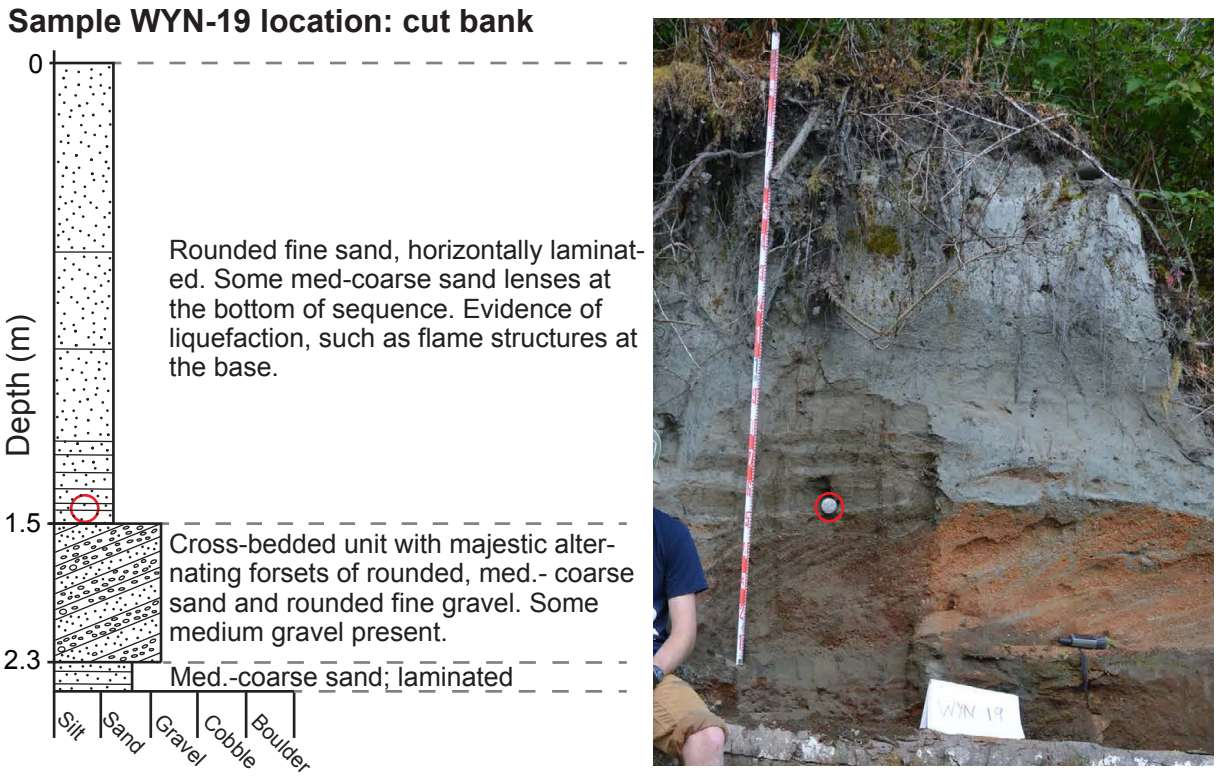
Sample WYN-19 location: cut bank
0
1.5
2.3
Depth (m)
Rounded fine sand, horizontally laminated. Some med-coarse sand lenses at the bottom of sequence. Evidence of liquefaction, such as flame structures at the base.
Cross-bedded unit with majestic alternating forsets of rounded, med.- coarse sand and rounded fine gravel. Some medium gravel present.
Med.-coarse sand; laminated
Silt
Sand
Gravel
Cobble
Boulder

Figure S19.

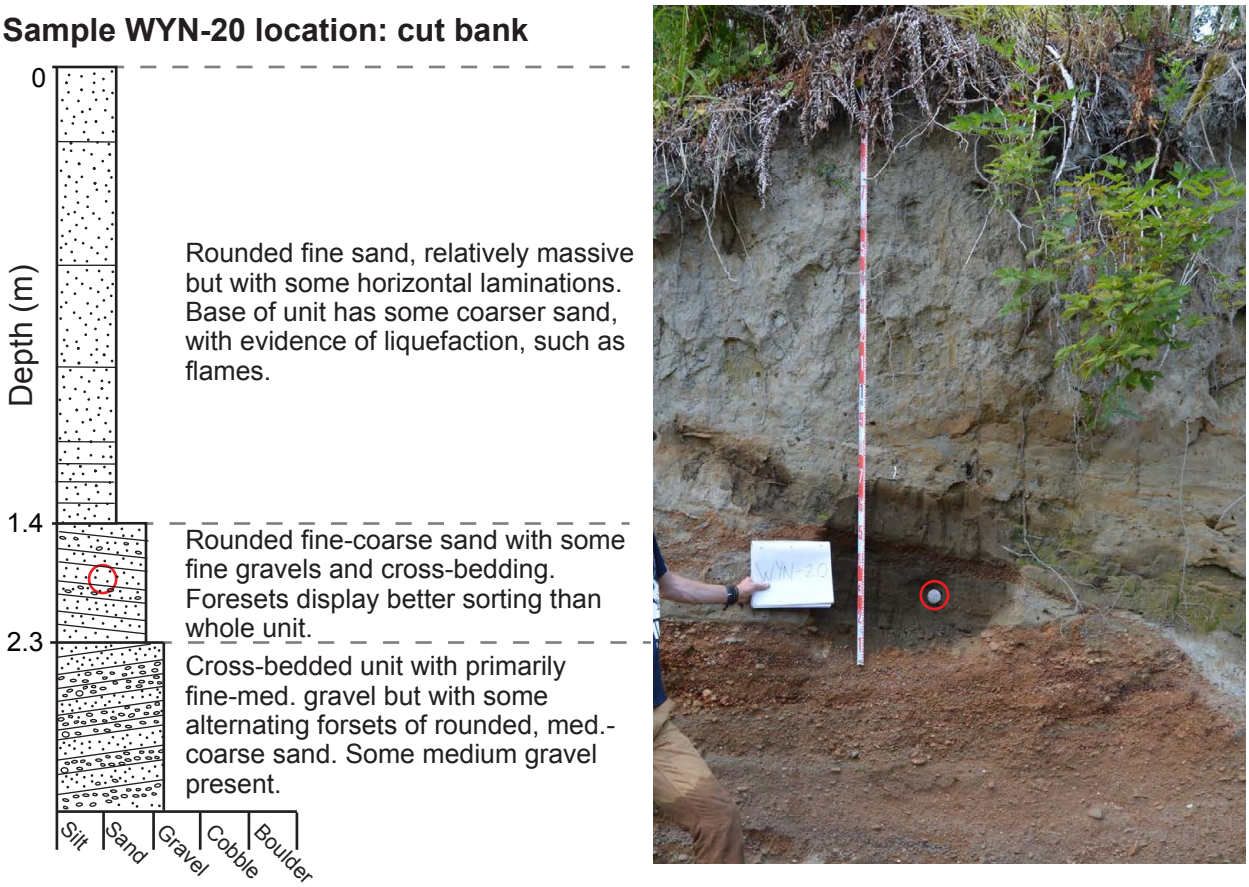
Sample WYN-20 location: cut bank
0
Depth (m)
Rounded fine sand, relatively massive but with some horizontal laminations. Base of unit has some coarser sand, with evidence of liquefaction, such as flames.
1.4
Rounded fine-coarse sand with some fine gravels and cross-bedding. Foresets display better sorting than whole unit.
2.3
Cross-bedded unit with primarily fine-med. gravel but with some alternating forsets of rounded, med.-coarse sand. Some medium gravel present.
Silt
Sand
Gravel
Cobble
Boulder
WYN-20

Figure S20.

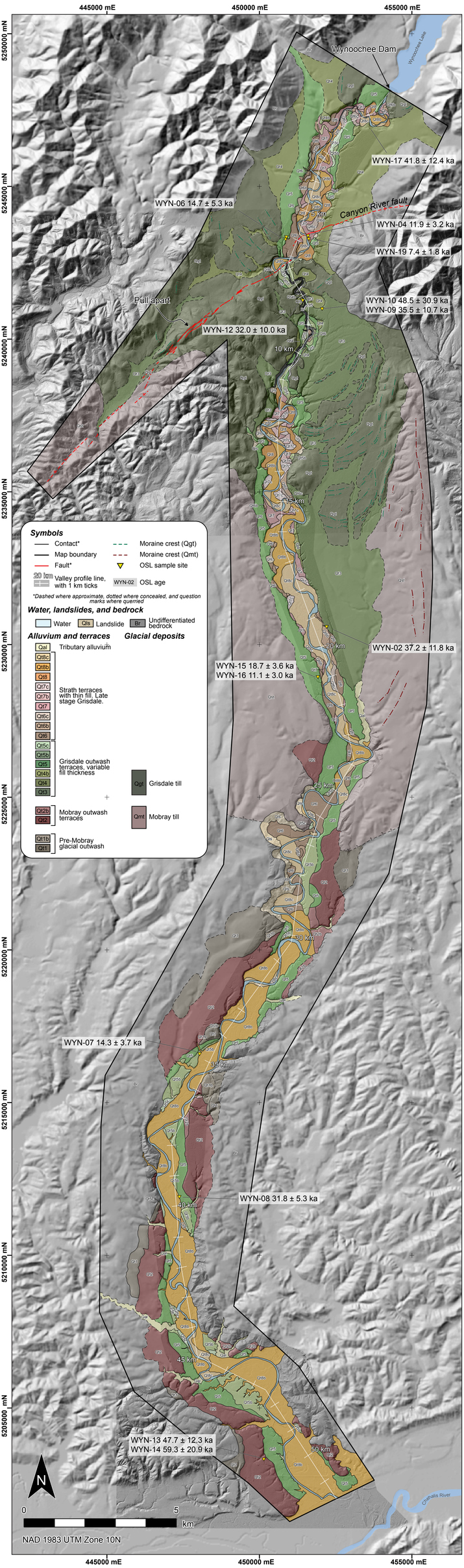

Plate 1: Detailed geomorphic map of the Wynoochee River valley south of the Wynoochee Dam. Valley distance indicated here is used in the main text body. OSL = optically stimulated luminescence.